Fluid-structure interaction analysis of a vertical-axis tidal turbine in surge motion using 2D panel method

Federica Perassi

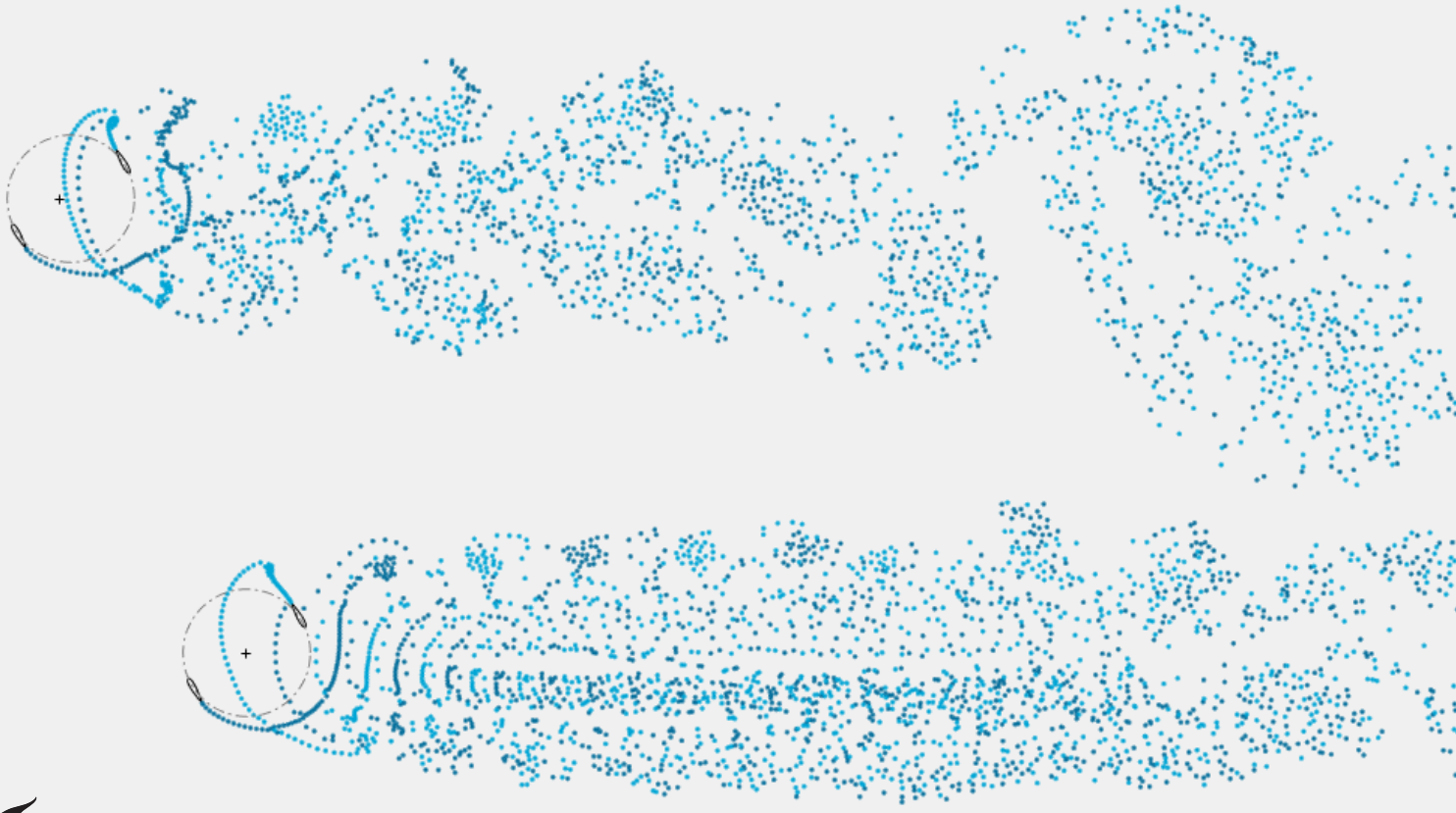

TU Delft

Fluid-structure interaction analysis of a vertical-axis tidal turbine in surge motion using 2D panel method

by

Federica Perassi

to obtain the degree of Master of Science in Sustainable Energy Technology
at the Delft University of Technology,
to be defended publicly on Tuesday October 12, 2021 at 09:30 AM.

Student number:	5149843	
Project duration:	November 16, 2020 – October 12, 2021	
Thesis committee:	Dr. A. Jarquin Laguna,	TU Delft, supervisor
	Prof. dr. ir. C.J.Simão Ferreira,	TU Delft
	Dr. ir. D.A.M. de Tavernier,	TU Delft

An electronic version of this thesis is available at `http://repository.tudelft.nl/`.

TU Delft

Abstract

Under real sea conditions, floating vertical-axis tidal turbines experience motion in six degrees of freedom induced by waves and currents. The floating platform's dynamic behaviour influences the relative motion between the turbine and the current stream, with a direct effect on the thrust force and performance of the rotor. The available scientific literature commonly investigates the fluid-structure interactions of vertical-axis tidal turbines under the floating carrier's motions using Computational Fluid Dynamics (CFD), which is the most computationally expensive and highest-fidelity method available for the modelling of vertical-axis turbines. In this project, the 2D free-wake vortex panel method implemented in the TU Delft in-house U2DiVA code is adopted. The validity of the tool is first investigated by verification against the scientific literature of 2D CFD for surge, sway and yaw. The second part of this work studies the effect of harmonic platform's surging motion on the time evolution of the hydrodynamic coefficients and of the velocity triangles of two existing floating vertical-axis tidal turbines in unbounded uniform tidal current.

In this work, the U2DiVA code is indicated as a conservative and time-effective tool to assess the hydrodynamic response of vertical-axis tidal turbines under floating platform's motions in the two-dimensional plane. Its accuracy is limited by the potential flow assumption, which causes overestimation of the hydrodynamic coefficients. The vortex panel method also limits the investigation of the dynamic stall phenomenon and flow separation. The results of the second part of the project suggest that surge motion introduces multiple frequencies of oscillation and increases the peak loading. Consequently, more severe cyclic loading occurs, impacting on the structural strength of the turbine. The origin of the oscillations is traced back to the time evolution of the velocity triangles. The surge velocity and displacement modify the flow field perceived at the blades, affecting the actual transient value of the tip speed ratio and the wake evolution in time, which generate, respectively, a wider amplitude of oscillation and an irregular profile of the history curves of the simulation quantities. The analysis of the wake trajectory reveals that spindle-shaped regions develop in the far-wake as a result of surging motion, and that the near-wake is characterised by more frequent and stronger blade-vortex interactions compared to the stand-alone turbine. Moreover, the results show that surge is beneficial to the average power extraction while only marginally affecting the mean loading. The investigation of possible tuning of rotor operating parameters suggests that control strategies could be developed for modifying the response of the vertical-axis rotor to the surge conditions. The rotational speed could be tuned either for the maximization of power extraction or for the reduction of cyclic loading. Instead, the initial blade azimuth of the turbine is not a determining parameter for the hydrodynamic response to the surging motion; this result suggests that yawing motion should weakly impact the hydrodynamics of the rotor compared to surge.

The findings of this research provide insights about critical aspects for the design of floating vertical-axis tidal turbine systems. The U2DiVA code can be applied for the study of the hydrodynamic response of the rotor under surging, swaying and yawing motion, as either independent or coupled motions, taking into account its limitations. The analysis of the time variation of the loads exerted by the rotor due to the platform's wave response motion is beneficial for the design of safe and reliable control strategies, as well as for the design of the mooring system. It also provides relevant information on the structural strength, fatigue life and power output variation of the turbine under specific floater's motions.

Acknowledgements

First, I would like to express my gratitude to Dr. A. Jarquin Laguna for the supervision and for the opportunity to work on such a challenging research topic. He provided me with invaluable advice and study material, but most importantly he transmitted me the passion and motivation to complete the project. I would also like to thank professor Ferreira and Dr. de Tavernier for being available to clarify my doubts in the course of the project and for extending my knowledge about vertical-axis turbines and the tools for their modelling.

Special thanks to my family and friends, without whom I wouldn't have been able to complete this project and the master degree itself. Chiara, Rebecca, Gabriele, Serena, Beauty: thank you for being there for me at literally any time, day and night, listening to my unnecessarily long voice notes about my adventures and life crisis and for teaching me not to fear the distance. I would also like to thank all the friends I met in this beautiful and exciting years in the Netherlands, especially Arianna, Achint, Dat, Alejandro, Josè, Elsa, Irina and the roommates of professor Henketstraat.

Contents

List of Figures

List of Tables

Nomenclature

Greek symbols

α	Angle of attack [°]
β	Angle for airfoil panelling [°]
$\Delta\theta$	Rotor displacement angle per time step [°]
Δt	Time step [s]
Δx	Horizontal distance [m]
Δx_{TE}	Horizontal distance of the trailing edge vortex [m]
Δy	Vertical distance [m]
γ	Angle between the platform velocity and the incoming wave velocity [°]
λ	Tip speed ratio [-]
μ	Strength of doublets [m^2/s]
ν	Kinematic viscosity of water [m^2/s]
Ω	Rotational speed of the rotor [rad/s]
ω_e	Frequency of the platform's motions [rad/s]
ω_{wave}	Frequency of waves [rad/s]
Φ	Phase angle [°]
ϕ	Velocity potential outside the body [m^2/s]
ϕ_i	Velocity potential inside the body [m^2/s]
ψ	Blade inflow angle [°]
ρ	Density of water [kg/m^3]
σ	Strength of sources [m^2/s]
Θ	Blade azimuthal position [°]
θ_p	Blade pitch angle [°]
θ_{yaw}	Angular rotor displacement induced by yaw [°]
ξ	Rotor displacement amplitude due to platform's motion [m]

Latin symbols

A	Platform's motion velocity amplitude [m/s]
B	Number of blades [-]
B_k	Aerodynamic influence coefficient of the airfoil sources [-]
c	Chord length [m]

C_k Aerodynamic influence coefficient of the airfoil doublets [-]

C_l Aerodynamic influence coefficient of the wake doublets [-]

C_M Torque coefficient [-]

C_P Pressure coefficient [-]

C_S Speed of sound in water [m/s]

C_F Hydrodynamic force coefficient [-]

C_{power} Power coefficient [-]

D Diameter of the rotor [m]

F Hydrodynamic force per unit length [N/m]

k Wave number [1/m]

l Panel length [m]

l_0 Fixed position of blade [m]

M Torque per unit length [N]

$Mach$ Mach number [-]

n Normal direction [-]

N_{panels} Number of panels over each airfoil [-]

P Power per unit length [W/m]

R Radius of the rotor [m]

r Distance between the singularity element and the point of computation [m]

$Reynolds$ Reynolds number [-]

S Panel surface [m^2]

T Period [s]

t Time instant [s]

tc Airfoil thickness-to-chord ratio [-]

U Velocity [m/s]

V Forward speed of the platform [m/s]

X' Horizontal position of a point of the rotor geometry under platform's motion [m]

X Horizontal position of a point of the rotor geometry [m]

Y' Vertical position of a point of the rotor geometry under platform's motion [m]

Y Vertical position of a point of the rotor geometry [m]

Subscripts/superscripts

0 Rotor parameter

∞ Tidal free-stream

D Drag

disp	Rotor displacement component
induced	Induced component
L	Lift
n	Normal component
opt	Optimal value
otherairfoils	Component induced by the airfoils' panels
P	Center of yaw motion
rel	Relative motion
rotation	Turbine rotation
surge	Platform's surge motion
sway	Platform's sway motion
t	Tangential component
TOT	Total rotor quantity
wake	Component induced by the wake
x	Horizontal component
y	Vertical component
yaw	Platform's yaw motion

Abbreviations

AC	Actuator Cylinder
BEM	Blade Element Momentum
CFD	Computational Fluid Dynamics
DMST	Double Multiple Stream Tube
HAT	Horizontal-Axis Turbine
HATT	Horizontal-Axis Tidal Turbine
MSE	Mean Squared Error
O&M	Operation and Maintenance
TRL	Technology Readiness Level
VAT	Vertical-Axis Turbine
VATT	Vertical-Axis Tidal Turbine
VAWT	Vertical-Axis Wind Turbine

1 Introduction

As the world's population increases and the energy demand rises, several technologies are being researched and implemented to allow the transition towards a carbon-neutral energy system. The most common technologies for renewable energy production are hydropower, wind energy, solar energy, biomass and geothermal, with the first two being the main sources of renewable electricity to supply the world energy demand [1]. The diversification of the energy production is crucial as it guarantees access to clean energy everywhere by exploiting the local natural resources. In particular, coastal nations could potentially exploit ocean energy, a large untapped resource which is available in various forms. Its potential can be harvested by turning the power of tides, waves and differences in sea temperatures and salinity into electricity [2].

In 2020, the total installed ocean energy capacity worldwide was 34MW, of which 78% was installed in European waters [3]. A significant increase of the deployed ocean energy capacity is expected over the coming years as a result of the ongoing development and reduction in costs of ocean energy technologies [4]. According to the European Commission (2020), the EU objective of reaching 1GW of installed ocean energy capacity by 2030 and 40GW by 2050 is "realistic and achievable" [4].

In the following sections, some background information about tidal stream/current energy is first introduced. Second, the problem statement is defined in section 1.3. Finally, the scope of the thesis and the research questions are formulated in section 1.4 and the chapters division of the project is provided in section 1.5.

1.1. Background on tidal stream/current energy

Tidal stream/current energy is a promising ocean energy technology which has the potential to play a relevant role in the future energy mix [5], especially in UK, Canada, France, Norway, Spain, Indonesia, Taiwan, China, Malaysia, Philippines and New Zealand [6]. Since tides are mainly driven by gravitational attraction between the Earth, the Moon and the Sun and are periodic, tidal energy production is predictable and reliable [5]. Tidal energy can support grid stability and complement the power output of other intermittent renewable energy sources [7], such as solar energy or wind energy. Therefore, the potential of tidal energy technologies is mainly related to its predictability, dependability, large energy density and durability and can facilitate the decarbonisation of islands.

The predicted increase in tidal energy capacity over the next years is a consequence of both technological advances and reduction of costs. According to data from the EU funded projects, the tidal energy sector has already cut costs by 40% since 2015, decreasing the LCOE from 0.60€/kWh in 2015 to 0.34-0.38€/kWh in 2020. A further cost reduction is expected, with the LCOE reaching 0.15€/kWh by 2025 and 0.10€/kWh by 2030 [3]. Moreover, floating concepts are gaining interest in the offshore energy industry as more economically attractive than subsea concepts, in terms of installation cost as well as operation and maintenance (O&M). An additional benefit of floating energy converters compared to bottom-mounted turbines includes the exploitation of resources further offshore.

The recent improvements in tidal energy technology, focused on the extraction of kinetic energy from tidal currents, have been led by research and development studies in EU and its member states [6]. Ongoing European projects, such as FloTEC and TIGER (see Figure 1.1), are demonstrating the potential of floating tidal turbines and are supporting the progress towards the maturity of tidal technology. In fact, new concepts

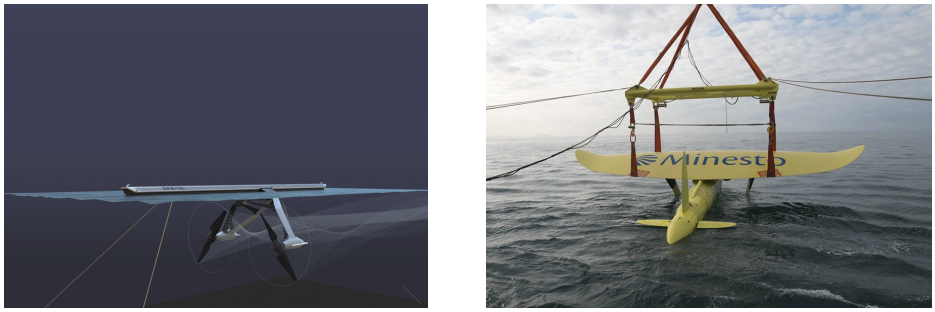

Figure 1.1: Tidal turbines demonstrators of EU projects (Horizon 2020): the O2 turbine FloTEC [8] on the left and the Minesto Deep Green Micro Grid converter TIGER [9] on the right.

are being tested, and the rotor and blade designs for tidal energy converters are continuously developed and improved through the design experience from hydropower, ship propellers and wind turbines [10]. Although the first tidal arrays are already deployed and operational, only a few converter designs of tidal stream turbines are at an advanced TRL stage (TRL 9) [3].

1.2. State of the art of tidal energy converters

Several concepts have been developed to exploit the potential of tides, in the form of potential energy or kinetic energy. Two main approaches to harvest tidal energy can be distinguished [5]: tidal barrages and tidal current turbines, also know as hydrokinetic devices. The existing tidal energy capacity is mostly harnessed by tidal barrage systems [5], which make use of a reservoir or basin civil structure to regulate the water level. but currently the research is directed towards the development of tidal stream/current technology.

Among the tidal current turbines, the designs to extract the kinetic energy of moving water are commonly classified based on the direction of the turbine rotation axis with respect to the main direction of the upcoming current speed: vertical-axis turbines (VATs) and horizontal-axis turbines (HATs), as shown in Figure 1.2. Traditionally, tidal current energy is exploited with horizontal-axis turbines mounted on fixed structures, either seabed mounted/gravity-based systems or pile mounted systems [11]. The horizontal-axis concept is more mature than the vertical-axis in terms of technology and supply chain for historical reasons. Because of the fatigue issues and the relatively low efficiencies of vertical-axis turbines, in the 20^{th} century the wind energy sector invested in the research of horizontal-axis turbines [12], considered more economically attractive, developing experimental and numerical analysis tools and enabling this concept to dominate the renewable energy market.

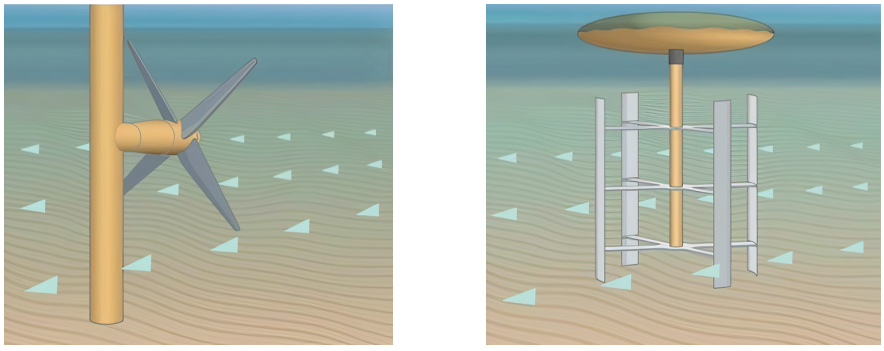

Figure 1.2: Examples of tidal turbine configurations: horizontal-axis tidal turbines on the left and vertical-axis tidal turbines on the right [13].

There is a renewed interest in the vertical-axis configuration of turbines, as they have the advantage of functioning independently of the stream path, compared to HATs which instead require a yaw control system [1]. Vertical-axis turbines are more advantageous for less energetic sites, since they can reach higher torque at lower rotational speed and lower current velocity [14], and for reduced available site area, because of the larger packing density due to the fast wake recovery [12]. Nevertheless, the vertical-axis concept is characterised by reduced performance and marked fatigue issues. The performance is penalized by the interactions

of the blades with the wake: the vortices shed by the blades in upwind position degrade the power extraction in the downwind region of the rotor. The vibrations resulting from the cycling loading originate from the time variation of the relative inflow velocity at the blade over the rotation. The vertical-axis configuration is also particularly beneficial for offshore deep-water applications. While the electrical components in a horizontal-axis tidal turbine (HATT) are sealed and placed under water, making O&M challenging [14], floating vertical-axis tidal turbines (VATTs) are expected to reduce O&M costs by allowing to relocate the power take off and generator above the sea surface thus facilitating the access to those components.

Vertical-axis turbines are further classified based on the force driving the rotation, as represented in Figure 1.3. Lift-driven turbines, also known as "Darrieus-type" VATs, rotate thanks to the lift force generated by blades shaped as airfoils resembling airplane wings [15], either straight or curved [16]. In drag-driven turbines, also called "Savonius-type" VATs, the torque originates from the difference of drag on the blades [17]. Although not able to self-start, the lift-driven turbines are more commonly used for energy extraction because of the higher efficiency. In fact, the blades of lift-driven turbines generally produce positive torque during the entire rotation when operated at optimal conditions, while the torque produced at the blades of a drag-driven turbine is positive for only half blade revolution [17]. In some applications, drag-driven turbines are preferred because of their simple and robust design and because of their ability to self-start [15].

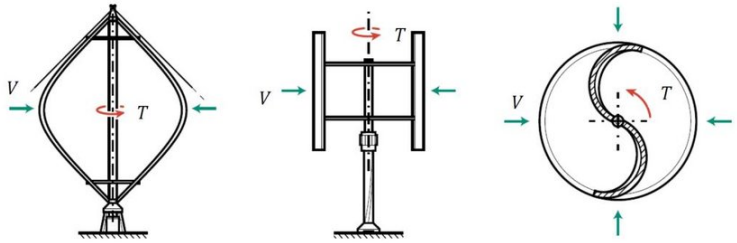

Figure 1.3: Schematic of three types of vertical-axis turbine: curved-bladed Darrieus turbine (a), straight-bladed Darrieus turbine (b) and Savonius turbine (c) [18].

1.3. Problem description

Because of the aforementioned advantages, floating vertical-axis tidal turbines are being studied as a very promising concept for offshore applications and several designs have been proposed and tested, such as the Haineng 1 [19] (HEU, China) and the Kobold [20] (INSEAN, Italy) among others. Many possible solutions to the main challenges of this concept are emerging, hence contributing to the maturity of the technology.

The study of the hydrodynamic performance of vertical-axis current turbines under rotation and wave-induced platform motion is a challenging research topic. Under real sea conditions, the floating system experiences motion in six degrees of freedom induced by waves and currents. The dynamic behaviour of the floating platform influences the relative motion between the turbine and the current stream, with a direct effect on the thrust force and power output of the rotor. Simultaneously, the hydrodynamic forces acting on the rotor of the turbine, depending on the sea environmental conditions and on the operating conditions of the turbine, affect the motion of the floating platform.

Understanding this complex hydrodynamic interaction could give insights about critical aspects for the design of a floating-VATT system. For instance, the analysis of the time variation of the loads exerted by the VATT due to the platform's wave response motion is beneficial for the design of safe and reliable control strategies. Since the turbine's operating conditions affect the coupled system motion induced by the sea environment, the study of the hydrodynamic loads acting on the system is equally important for the design of the mooring system. It can also provide relevant information on the effects of sea conditions on the structural strength and fatigue life of the turbine, as well as on the variation of the power output under specific floater's motions. The analysis of the wake trajectory can give insights on the fluid-structure interaction when the rotor moves with waves.

1.4. Scope of the thesis and research questions

This chapter provided some background on tidal energy and the vertical-axis turbine concept, as well as on the challenging research topic of floating vertical-axis tidal turbines under the platform's motions. The available scientific literature investigating the fluid-structure interaction of floating VATTs is limited and most commonly uses an uncoupled computational fluid dynamics approach, as will be discussed in Chapter 2. In this project, a 2D free-wake vortex panel method is selected for the modelling of VATTs under imposed floating platform's motions as it is an inherently unsteady method representing a trade-off between accuracy and computational cost among the available numerical modelling techniques for VATs. Additionally, the potential flow theory is fundamental and explicitly modelled, facilitating the interpretation of the simulation results of the second part of the project, which studies the effect of surging motion on the hydrodynamics of two existing floating VATTs. The investigation of the floating platform's motion is limited to the motion in the direction of the incoming current as the literature of coupled multi-degrees of freedom motion reveals that surge has a stronger impact on the hydrodynamic response of the rotor compared to the other degrees of freedom in the two-dimensional plane, which will be presented in 2.2.1. Consequently, the following research questions are formulated:

1. How do the results of a 2D free-wake vortex panel method compare to high-fidelity CFD models in describing the hydrodynamics of a vertical-axis tidal turbine under imposed harmonic platform motions?

2. What is the effect of prescribed surging motion of the floating support structure on the hydrodynamic loads and captured power of a vertical-axis turbine, in terms of:

   (a) magnitude, amplitude of oscillation and frequency content of the time history of the hydrodynamic coefficients?

   (b) time evolution of the velocity triangles at the blade section?

1.5. Thesis outline

This thesis project is structured in six chapters. In this first chapter, an introduction to tidal kinetic energy and to the floating vertical-axis turbines is provided and the scope of the research is described. In Chapter 2, an overview of the available modelling techniques for vertical-axis turbines and a review of the research papers dealing with the interaction of the floating structure subject to current and wave induced motions with the hydrodynamics of the vertical-axis turbine are presented and discussed. The 2D free-wake vortex panel method is defined for investigating the topic and the TU Delft in-house U2DiVA code implementing it is described in details in Chapter 3. Addressing the first research question, the tool is verified against the results of 2D CFD simulations of the scientific literature in Chapter 4. Finally, the hydrodynamic response of two existing lift-driven vertical-axis tidal turbines with straight blades, mounted on floating platforms experiencing identical surging motion, is studied in Chapter 5 using the U2DiVA code. The effect of surge motion is investigated in four steps in order to address the second research question. First, the magnitude and amplitude of oscillation of the hydrodynamic coefficients are analysed. Second, the frequency of oscillation of the simulation quantities is studied. Third, the modified time evolution of the velocity triangles is investigated, with focus on the wake trajectory. Fourth, some examples implementing possible tuning of rotor operating parameters for controlling the hydrodynamic response are provided. Conclusions and recommendations are drawn in Chapter 6.

2

Overview of the existing methods for the modelling of floating vertical-axis turbines

The dynamic behaviour of offshore renewable energy converters, such as wind turbines and tidal turbines, installed on floating platforms has been studied in the scientific literature with different approaches. This chapter deals with the current literature on the numerical modelling of floating vertical-axis turbines. First, the main approaches for the modelling of vertical-axis turbines, their advantages and limitations are described in section 2.1. Second, an overview of the modelling techniques for floating vertical-axis turbines, as coupled or uncoupled system, and the results of some relevant scientific articles about floating VATTs are provided in section 2.2. Eventually, some reflections on the available numerical modelling techniques for floating vertical-axis systems and on the literature review are presented in section 2.3.

2.1. Numerical modelling of vertical-axis turbines

Vertical-axis turbines can be simplified at different levels, as shown in Figure 2.1 in order of decreasing complexity [21]. The 3D rotor is the most complete representation of the VAT, as it includes the effect of the finite number of blades and the three-dimensional effects deriving from the finite blade length. Because of the high computational cost of the 3D representation, the 2D rotor simplification and actuator cylinder have been used in most of the scientific research. The 2D rotor assumes similar flow field on each section of the blades; it includes the effect of the finite number of blades but neglects tip effects. The simplification level requiring the lowest computational cost is the actuator surface, which represents the rotor as a cylinder in 3D and a circle in 2D on which the average blade forces over one rotation are applied. In this representation, both the effects of finite number of blades and finite blade length are not accounted for.

Different theories are associated to each simplification level to study the hydrodynamics of vertical-axis tidal turbines, as well as the aerodynamics of vertical-axis wind turbines (VAWTs). Relatively fast modelling techniques can be used at the actuator surface level, such as momentum model and actuator cylinder model. Vortex models and Computational Fluid Dynamics (CFD) can be applied to all the levels and result in higher fidelity and higher computational time, especially for more complete VAT representations. The main families of modelling techniques are reported below in order of increasing accuracy and computational time, and they are schematically represented in Figure 2.2.

2.1.1. Blade element momentum models

Momentum models (or streamtube models) solve the aerodynamic performance and blade loads in the actuator surface representation. The flow disturbance is determined by equating the streamwise aerodynamic force on the rotor blades to the time rate change in momentum through the rotor [22]. Several momentum models are available, representing the 2D actuator as single streamtube, multiple streamtube, double streamtube or double-multiple streamtube [23].

The most accurate version of momentum models available is the Double Multiple Stream Tube (DMST) developed by Paraschivoiu [24], which is a combination of the double streamtube model and the multiple streamtube model. It is frequently found in the literature of VAWTs [25, 26, 27] as well as of VATTs [28]. This analytical model relies on the Blade Element Momentum (BEM) theory and represents the rotor as a series

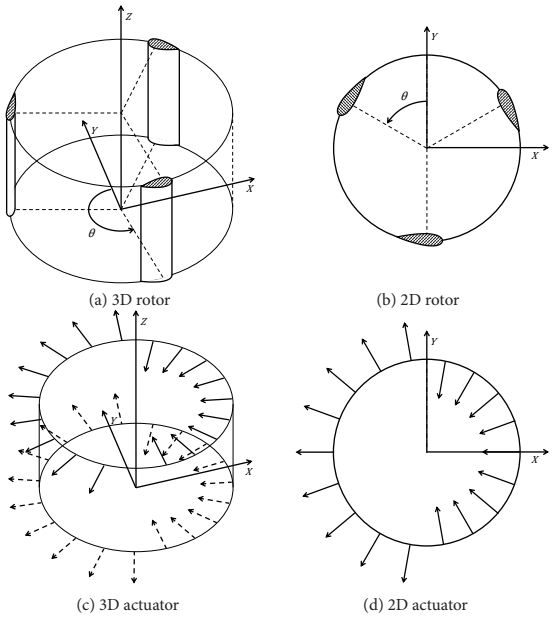

Figure 2.1: The four levels of vertical-axis turbine simplification for numerical modelling [21].

of adjacent independent stream tubes, for which momentum balance is carried out separately. Each stream tube is divided into an upwind half and a downwind half and the turbine is replaced by a pair of actuator discs at the intersections of the stream tubes with the airfoil's path. This results in a steady solution, found through iterative process [21]. The schematics of the rotor in the DMST model is illustrated in Figure 2.2(a).

Momentum models provide faster qualitative results compared to other numerical methods and give good predictions of the performance of VATs, especially for low solidity, low tip speed ratio and light-loaded cases [12]. In fact, their application is limited to turbines with small solidity (below 0.2): for large values of the solidity the assumptions of the model are no longer valid (i.e. homogeneous and steady flow; no frictional drag or non-rotating blade) [27]. Moreover, some assumptions of the model are contradictory to the flow physics of vertical-axis turbines, and cause inevitable error. The wake expansion is not modelled because of the assumption of independent and straight streamtubes. Also, the interaction between the flow in the upwind and downwind regions of the rotor is not modelled: the wake originating upwind is assumed to be fully developed before reaching the downwind half and the effect of the downwind actuator disk on the upwind one is neglected. Because of these assumptions, the DMST cannot model the occurrence of flow reversal and it is not accurate in highly loaded cases [29].

2.1.2. Actuator cylinder models

The actuator cylinder (AC) model uses the 2D steady incompressible Euler equations and continuity equation to compute the flow field and the BEM theory to compute the blade loads on the rotor, represented either as 3D or 2D actuator surface.

The AC method developed by Madsen [30] is commonly used in the literature of floating VAWTs because of its simplicity and low computational cost [31, 32]. It requires the force field on the blades as input, for which BEM is often used. From the normal and tangential forces to the rotor plane, the induced velocity is computed analytically through the continuity equation and Euler equation. The schematics of the AC model is provided in Figure 2.2(b). Similarly to momentum models, the solution is steady and computed through an iterative process. However, the actuator cylinder model is characterised by a higher accuracy since it doesn't assume independent stream tubes, taking into account the interaction between streamtubes and the effect of the downwind region of the rotor on the upwind one [29, 31].

Assuming steady inflow conditions, the AC method doesn't model dynamic effects which are typical of VATs operation. Some effects can be modelled in addition; for instance, dynamic stall can be included via the Beddoes-Leishman dynamic stall model. Furthermore, it is not as accurate for highly loaded rotors such as DMST [29].

2.1.3. Vortex methods

Higher-fidelity can be obtained through vortex models for all rotor simplification levels, which are based upon vortex representations of the blades and their wakes and assume potential (inviscid) flow. The representation of the blade as vortex system is built on two main principles: Helmholtz' vortex theorem and Kelvin's circulation theorem. Diverse vortex methods can be found in the literature of vertical-axis turbines, and they belong to one of two main families, depending on the calculation method of the blade loads: lifting-line methods and lifting-surface methods (or panel methods). The first represent the blade as a single lifting line, usually placed at quarter chord point (see Figure 2.2(c)), and the second consist of straight vortex filaments arranged either on the airfoil mean camber line or on the airfoil surface. These methods are unsteady as they need to be solved in time [21].

Several vortex methods can be found in the scientific literature of VATTs, either based on the lifting-line or lifting-surface approximations. The VAT-VOR3D code [28], the CACTUS code (Code for Axial and Cross-flow TUrbine Simulation) [33], the Qblade code [34] and the discrete vortex method by the University of British Columbia (DVM-UBC) [35, 36] are some examples of existing tools implementing the lifting-line vortex theory. Lifting-line methods cannot represent the near blade phenomenon (e.g. cavitation), since the blade element is simply represented as a bound vortex, and they generally do not model the free surface effect and the mounted frame effect, which in reality cause a significant power reduction [35]. In order to represent the near blade, potential flow panel methods are used, which are based on the discretization of the body surface into a number of panels. The solution consists of finding the vortex strength of each panel numerically; from this information, it is possible to compute secondary outputs such as the total circulation, lift force, local pressure distribution and local velocities. Panel methods can resolve flow curvature effects and deal with finite blade length effects better than lifting-line models [12]. An example of lifting-surface method used in the scientific literature of VATTs is the 2D Vortex Panel Method VPM2D developed by Wang et al. in [23].

Compared to momentum model and actuator cylinder model, vortex methods require a higher computational time but lead to more accurate results, especially for high solidity and large tip speed ratio [12]. Since they rely on the assumption of incompressible and inviscid flow, compressibility and viscosity effects (such as viscous diffusion and decay of vortices) are not modelled, which limits the analysis of the dynamic stall phenomenon. A possible method to introduce the viscosity and compressibility correction consists in incorporating a boundary layer model in the vortex method [37], with the drawback of further increasing the computational cost.

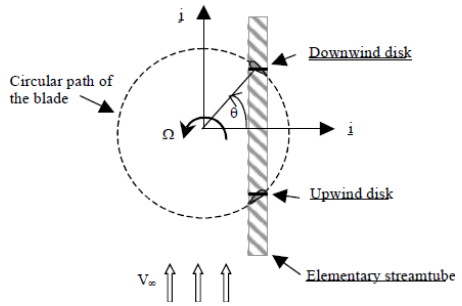

(a) Momentum model (DMST) [24]

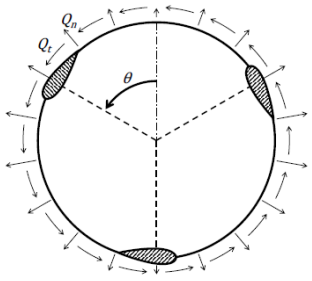

(b) Actuator Cylinder [21]

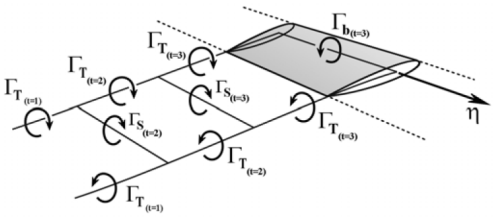

(c) Vortex method (VAT-VOR3D) [28]

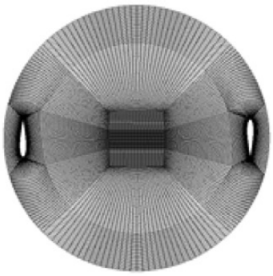

(d) CFD [38]

Figure 2.2: Schematics of the four main families of numerical techniques for the modelling of vertical-axis turbines.

2.1.4. Computational fluid dynamics

The highest fidelity in the modelling of a vertical-axis turbine can be reached by adopting Computational Fluid Dynamics (CFD) numerical simulations, which solve the Navier-Stokes equations in space and time inside a given computational domain, providing insights into the fluid dynamics of a process [39]. The solution is either steady or unsteady, depending on the model used.

This numerical tool is very time-consuming and its results are strongly dependent on the settings and assumptions. This can be seen by the fine meshing required in CFD simulations as illustrated in the example of Figure 2.2(d). A CFD simulation gives accurate solutions only when the problem is well-posed. The main advantage of this approach is that all field quantities are known (almost) everywhere inside the domain and that it usually leads to more accurate results compared to the lower fidelity methods explained in the previous subsections. Moreover, it allows the modelling of viscosity, compressibility and finite blade length effects and the study of the near blade phenomenon. It is therefore an insightful tool for the understanding of flow phenomena. Nevertheless, it is the most complex and computationally expensive approach for modelling a vertical-axis turbine. In order to reduce the computational cost, the vertical-axis turbines are often modelled in 2D, which introduces the need for 3D effects corrections (such as arm effects and free surface effects).

2.2. Fluid-structure interaction for floating turbines

The numerical modelling of offshore turbines is challenging as they are subjected to loads acting on the rotor and on the floating carrier which originate from the interaction of the system with the sea environment. In order to fully understand the system, the hydrodynamics, mooring line dynamics, structural dynamics, control dynamics and, in case of wind turbines, aerodynamics should be modelled in a coupled approach. For the modelling of the hydrodynamic module in VATTs and aerodynamic module in VAWTs, the numerical techniques described in section 2.1 have been used in the scientific literature of floating vertical-axis turbines within either coupled or uncoupled approaches. Fully coupled models often employ low computational cost VAT representations, applying, for example, momentum models, actuator cylinder models or vortex models [12]. Since the interfacing of the different programs in a coupled approach has the drawbacks of introducing instabilities and increasing the computational cost, uncoupled approaches are more commonly found in the scientific literature as well as in the engineering practice used by turbine developers. An overview of the techniques for the modelling of vertical-axis turbines presented in section 2.1 and examples of methods used in the literature of VATTs and VAWTs are illustrated in the scheme of Figure 2.3.

In the literature of vertical-axis tidal turbines, uncoupled approaches have been used to investigate the influence of the floater's motion on the performance and unsteady loads of the rotor [38, 40, 41, 42] or, vice versa, the effect of power generation on the platform motion and mooring forces [11]. These approaches, based on computational fluid dynamics, will be described in details in 2.2.1.

The literature of floating VAWTs shows larger variety of modelling techniques, including high-fidelity 3D and 2D CFD but with a preference for the low computational cost models, since the coupling of floater's motions and turbine model is generally obtained iteratively. For instance, the Paraschivoiu's DMST model, including additional corrections (such as for dynamic stall, 3D effects and unsteady wind profiles), was applied for the description of the aerodynamics of the VAWT in the coupled approach proposed in [43] and in the semi-coupled approach of [26]. The first approach uses the nonlinear coupled motion equations of the floating platform to model the floating VAWT as a rigid body, including the inertia, damping and restoring forces and moments, mooring force and environmental loading. Instead, in the approach described in [26] the aerodynamic loads are used as inputs to the hydrodynamic model to calculate the new platform position, while the inflow velocity components for the aerodynamic module are computed from the instantaneous position of the platform. Another common numerical modelling technique used in the literature of floating VAWTs is the actuator cylinder model developed by Madsen, which is more accurate than DMST model and is characterised by a low computational cost. In [31, 32] the AC model is applied, including corrections for the dynamic inflow and dynamic stall, and coupled to a tool modelling the platform's hydrodynamics, structural dynamics and controller dynamics for a fully coupled approach.

2.2.1. The uncoupled CFD approach

Research in the effects of different degrees of freedom motion on vertical-axis tidal turbines has already been conducted, as well as general reviews of the dynamic behaviour of floating marine energy devices [44]. The most popular method in the literature to study the unsteady hydrodynamic characteristics of VATTs subject to floating carrier's motion induced by waves and currents is CFD. Several scientific articles [11, 38, 40, 41, 42, 45]

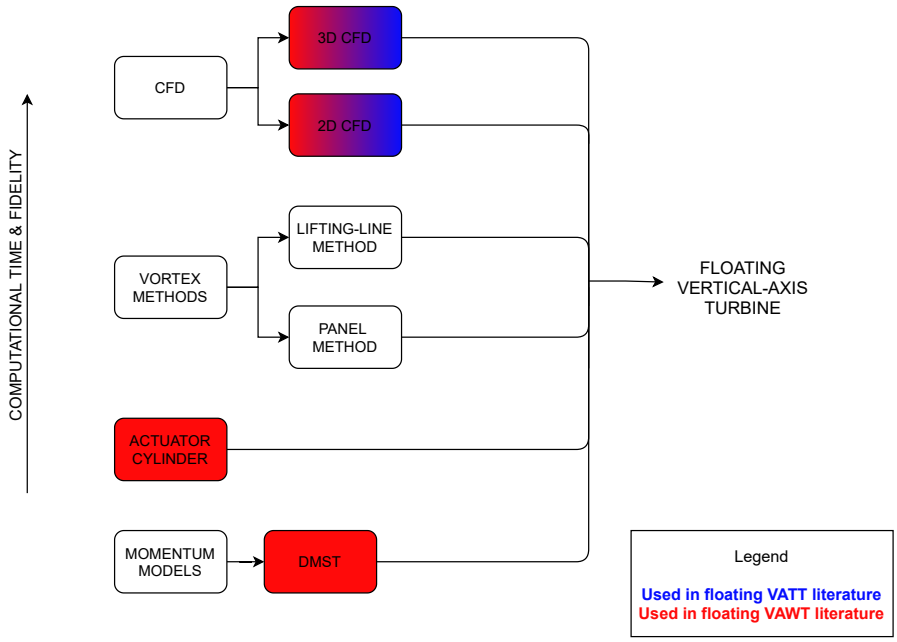

Figure 2.3: Overview of the techniques for the numerical modelling of vertical-axis turbines and examples of methods used in the scientific literature of floating VATTs and VAWTs.

employ CFD for investigating the effect of the platform's motions on the turbine's performance and loads by assuming constant rotational speed of the turbine, constant inflow velocity and simply harmonic platform's motion induced by waves. The assumption of harmonic platform's motions is valid when assuming regular sea waves, resulting in motions with the same frequency as the waves since the platform is stationary [46]. Typical values of sea waves are assumed in the literature of uncoupled CFD for VATTs modelling to define the amplitude and frequency of platform's oscillations.

In 2016, Sheng et al. [38] employed CFX ANSYS to simulate the hydrodynamic performance of a 2D VATT under surge motion. Simulations with different values of surge frequency, surge amplitude and tip speed ratio were conducted. The time history curves of the hydrodynamic load coefficients were extracted from the results of the CFD simulations. Eventually, Sheng et al. developed a trigonometric function to fit the time history curves of the load coefficients and used a least-squares method to obtain the hydrodynamic derivatives under the different cases simulated. From the results of the numerical simulations, they concluded that surge modifies the amplitude of the hydrodynamic loads, causing periodic variation of the peak values, as illustrated in Figure 2.4. Moreover, the results showed that the effect of surge oscillation motion on the force of the vertical-axis tidal turbine can be described by the hydrodynamic derivatives of the damping coefficient.

Several other papers [11, 40, 41, 42, 45] apply the same approach of Sheng et al., either in 2D or 3D, to analyse the fluid-structure interaction of vertical-axis tidal turbines under different wave-induced motions. Similarly to the aforementioned case of surging motion [38], the results of these papers showed that the envelopes of the load coefficients and power coefficient undergo cyclical oscillations directly correlated to the floating platform's motions (yaw [40], sway [42] and pitch [45]), with the oscillation amplitude increasing with the motion frequency. It was also reported that the average values of the hydrodynamic coefficients are only marginally affected by the floater's motion and that the damping force is generally the dominant contribution to the fluctuations of hydrodynamic loads induced by wave-response motion. These fluctuations induced by the sea environment cannot be ignored during the design of the turbine structure and control system, since they increase the peak loads on the turbine. This impacts negatively on the turbine's structural integrity, reducing its fatigue life.

The floating carrier's motions can induce significant variations of the power coefficient, impacting on the annual energy yield of the power station. For instance, yawing motion only marginally decreases the power output [40], while pitching motion has a positive influence on the power coefficient as a result of the increase in tangential force of the upstream disk [45], as pictured in Figure 2.5.

Furthermore, some researchers studied the effects of coupled multi-degrees of freedom motions on the VATT performance. In 2018, Wang et al. [41] analysed the hydrodynamics of rotating VATT under surging and

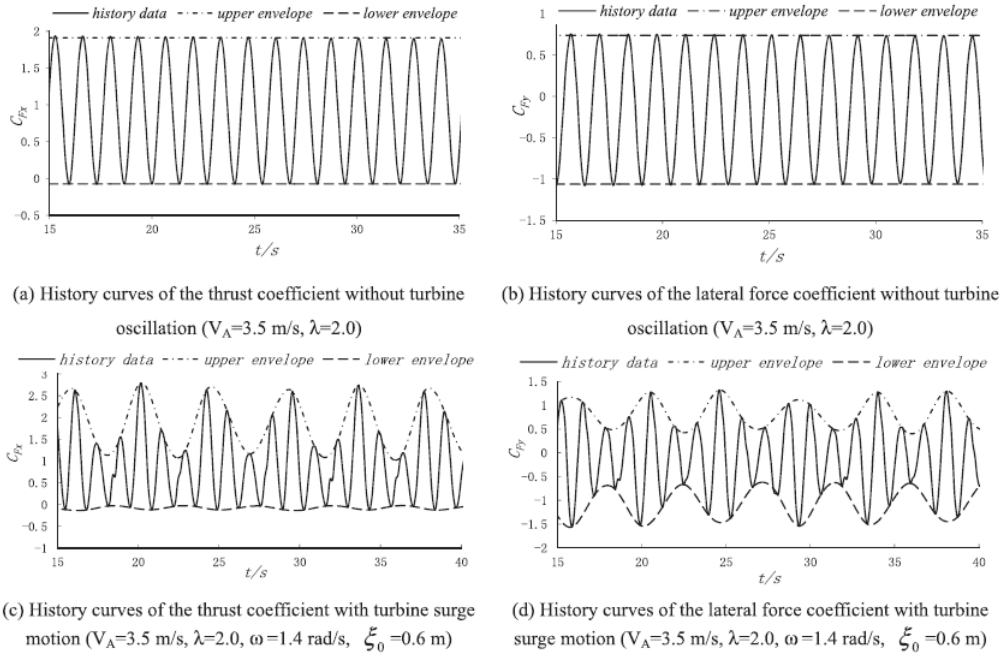

(a) History curves of the thrust coefficient without turbine oscillation (V_A=3.5 m/s, λ=2.0)

(b) History curves of the lateral force coefficient without turbine oscillation (V_A=3.5 m/s, λ=2.0)

(c) History curves of the thrust coefficient with turbine surge motion (V_A=3.5 m/s, λ=2.0, ω=1.4 rad/s, ξ_0=0.6 m)

(d) History curves of the lateral force coefficient with turbine surge motion (V_A=3.5 m/s, λ=2.0, ω=1.4 rad/s, ξ_0=0.6 m)

Figure 2.4: Effect of the floating platform's surging motion on the cyclic loading of the vertical-axis tidal turbine rotor of the simulations conducted by Sheng et al. in [38].

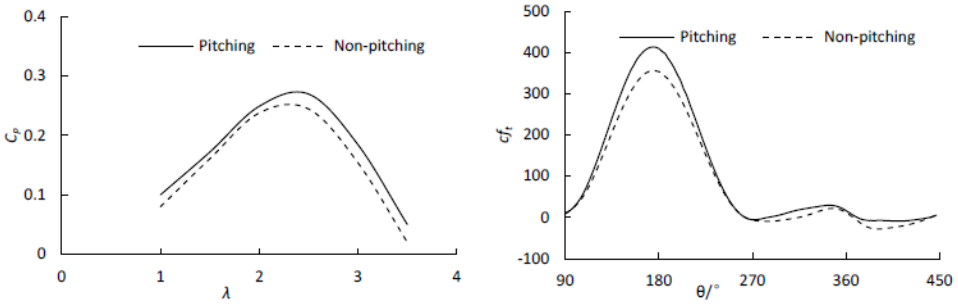

Figure 2.5: Effect of the floating platform's pitching motion on the power coefficient (on the left) and tangential force coefficient (on the right) of the vertical-axis tidal turbine of the simulations conducted by Zhang et al. in [45].

yawing coupled motions in unbounded uniform flow. They concluded that the effects on the hydrodynamic performance and loads are predominantly caused by surging motion, as can be seen in Figure 2.6, and that the fluctuation amplitude increases with increasing surging frequency. The effects of yawing motions are only reflected for yawing frequencies much higher than the surging frequency. Similar results were observed by Xu et al. [42], who investigated the hydrodynamics of a rotating VATT under surge and sway. The results showed that, when surging and swaying motions are coupled at different frequencies, the main effect on the hydrodynamic loads is caused by surge, while the effect of sway is only relevant when the swaying frequency is much higher than the surging frequency. Therefore, motions in some degrees of freedom are more relevant than others, having larger impact on the turbine's hydrodynamic response.

Interestingly, Hu et al. [11] applied the same methodology to study the coupling of VATT loading with platform's motion and mooring lines from the perspective of the floater, focusing on the effect of VATT operation on the motion of the floating platform and on mooring line forces. The results showed that the turbine's rotation affects marginally heave response, induces more severe pitching and surging (sway, roll and yaw are neglected due to the symmetrical characteristics of the floater) and affects the tension at the different mooring lines. This study demonstrates that simply applying forced oscillation on the turbine is not an accurate representation of the coupling floater-VATT; also the effect of VATT operation on the floater's motion should be considered.

Computational fluid dynamics has been extensively used in the scientific research concerning this topic

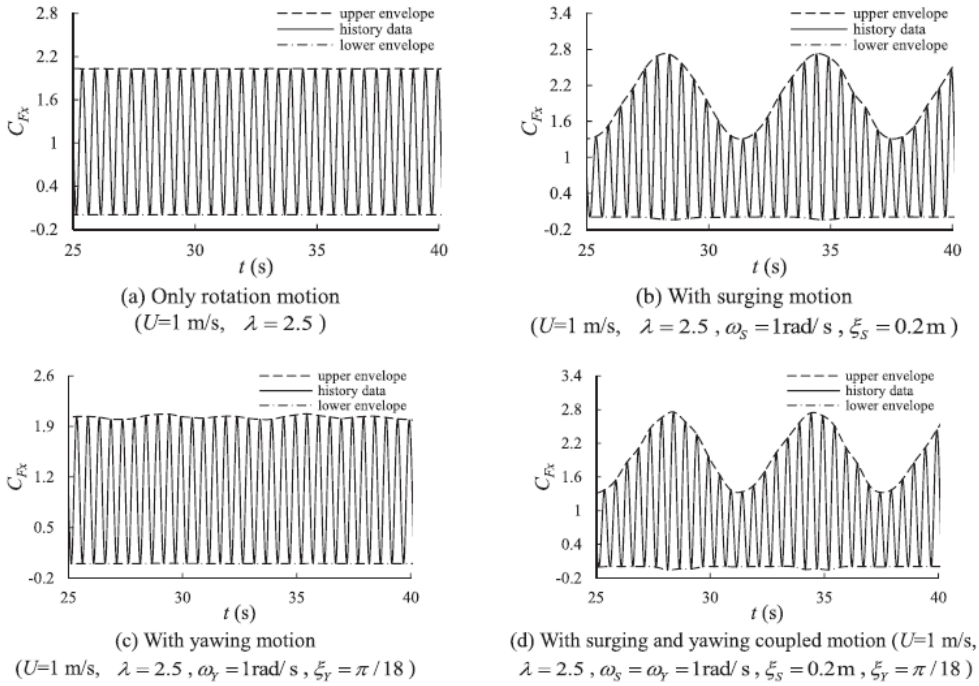

Figure 2.6: Effect of the floating platform's surge and yaw motions, individually and coupled, on the time-history curves of the VATT rotor thrust coefficient in the simulations conducted by Wang et al. in [41].

because it is capable of higher fidelity and higher level of details compared to other numerical methods for the modelling of VATs. Being a detailed model for fluid-structure interaction, it can give insights about the motion response characteristics of floating tidal technology and the hydrodynamic loads on the turbine. For example, Xu et al. [42] were able to analyse the evolution of the vortex distribution around the vertical-axis turbine under surging and swaying motions through CFX ANSYS simulations. They observed that at the blade tails the vortex is symmetric, while in the downstream, where vortex intensities decrease, the surging (swaying) motions would drive trailing vortex to fluctuate in x- (y-) direction, with the surging (swaying) motion period. Nevertheless, CFD modelling implies very high computational time.

2.3. Discussion

In this chapter, the available numerical modelling techniques for vertical-axis turbines were first described in section 2.1 and an overview of the literature of floating vertical-axis turbines, with a focus on the approaches used for tidal turbines, was provided in section 2.2. For the purpose of this thesis, the Unsteady Two-Dimensional Vorticity Aerodynamics model (U2DiVA) [47] is used for investigating the effect of wave-induced platform's motion on the hydrodynamics of a vertical-axis tidal turbine, with proper modifications to the code to integrate the platform's motions. The U2DiVA code implements in MATLAB the unsteady formulation of the vortex panel method presented by Katz and Plotkin in [37] and is described in details in Chapter 3.

The vortex panel method is chosen as it is inherently unsteady and as it represents a trade-off between accuracy and computational cost. In fact, the low computational cost DMST model often found in the literature of floating VAWTs as described in section 2.2 is not able to represent the unsteadiness introduced by the platform's motions on the flow perceived at the blades. Because of its assumptions, the DMST model suffers in accuracy for high loaded cases, large solidity rotors and high tip speed ratios. Moreover, it cannot model the unsteady interaction of the wake with the rotor either in the upwind half and downwind half. Being also the AC model based on the steady flow assumption, the lowest computational cost models and the actuator surface simplification level of the rotor were discarded. Compared to computational fluid dynamics, the most used approach in the literature of floating VATTs as described in 2.2.1, vortex panel methods have the advantage of a reduced computational time, of the order of magnitude of minutes to few hours, since known solutions are simply combined to satisfy boundary conditions instead of solving the Navier-Stokes differen-

tial equations. The computational cost can be further decreased by setting larger grid resolution and longer time steps, while CFD simulations require fine grids and work on a limited range of time step sizes depending on the grid resolution. Additionally, the potential flow theory is more fundamental and explicitly modelled, facilitating the understanding and interpretation of simulation results. However, since this method is based on the assumption of inviscid and potential flow, viscosity and compressibility effects are not included. Being a two-dimensional method, the effects related to the finite blade length are also neglected.

Finally, the approach used in this project is one way coupling, implemented with the imposition of the platform's motion on the instantaneous position and velocity of the rotor. From the examples of the fully coupled approaches available in the literature of floating VAWT described in section 2.2, it was concluded that they must compromise the accuracy of rotor representation in order to reduce the computational time to represent the whole system. In order to use the high-fidelity vortex panel method, the full coupling will not be implemented in the scope of this thesis due to the limited time of the project.

3

The 2D vortex panel method

In order to understand the effect of wave-induced platform's motions on the hydrodynamics of vertical-axis tidal turbines, the unsteady 2D vortex panel method is adopted in this project because of the advantages explained in Chapter 2. In this chapter, a description of the TU Delft in-house U2DiVA code [47], an unsteady multibody model implementing the formulation of the 2D free-wake vortex panel method presented by Katz and Plotkin in [37], is first provided in section 3.1. Next, the integration of the floating platform's motions in the commercial software MATLAB is described in section 3.2, followed by the sensitivity of the numerical model to some of its input parameters analysed in section 3.3.

3.1. Description of the U2DiVA code

The vortex panel method is a numerical technique which allows for sufficient accuracy and realistic modelling of the bodies with a reasonable level of complexity. It is based on the discretization of lifting bodies in panels, which are represented by a distribution of singularity elements of such strength to make the body surface a streamline of the flow. The solution of such model is computed at each time step from a system of linear equations, and it consists of defining the strength of the singularity elements while satisfying the Kutta condition. This model provides insights in the flow physics and near-blade phenomena, and the solution can be found numerically at any point of the fluid domain. Compared to CFD, panel methods require a relatively short computational time since the meshing of the entire computational domain is not necessary. However, the accuracy of the solution is limited by the assumptions of incompressible and inviscid flow at the base of the potential flow theory.

In this section, the code is described in detail in order to explain the inputs, basic equations and generated outputs and to facilitate the understanding of the platform's motion integration. A flowchart of the script is illustrated in Figure 3.2.

3.1.1. Initialization of the simulation

Before running the simulation, some inputs need to be defined in three separate files, organized as reported below.

1. The rotor geometry, turbine motion in time and center of momentum are defined in a *geometry file*.
2. The inflow conditions, in terms of incoming current velocity and angle, are defined in a *wind script*.
3. *Other settings* are assigned separately, such as: GPU details, simulation name and directories, number and size of the time steps, settings for the generation of the output, maximum wake length, airfoil data file, size of the near wake, proximity scale.

The singularity elements used in the representation of the airfoils and wake need to be selected. In this work, the airfoils are represented by a 2D distribution of sources and doublets over a number of flat panels N_{panels} covering the surface of each airfoil. The vortex strength per unit length (σ for the sources, μ for the doublets) is assumed to be constant over each panel and to vary from one panel to another. Instead, the near-wake is modelled with doublets, and the mid and far wake are modelled with vortex points. From this

discretized geometry, corner points and collocation (control) points are defined for each panel. The control points are located at the panel midpoints, slightly inside the airfoil.

The time of the unsteady simulations is also discretized and the time instant at the j^{th} time step is computed as:

$$t_j = t_{j-1} + \Delta t \tag{3.1}$$

where the finite time step Δt[s] is defined from the rotational speed Ω and the angular displacement $\Delta\theta$ admitted at each time step for a stand-alone rotor as $\Delta t = \frac{\Delta\theta}{\Omega}$.

Before the computation of each time step starts, the body geometry and the wake are initialized as doublets and sources. The strength of the singularity elements in the initial time step is set to zero.

3.1.2. Definition of the geometry: wake convection and airfoil panelling

At each time step, the position of the wake vortex points is updated as well as the geometry of the rotor. Since the U2DiVA code implements a free-wake method, the wake position in time is determined by the local velocity at every wake element, calculated from three contributions: the incoming velocity U_∞, the velocity induced by the airfoil elements and the velocity induced by the wake itself (self-induction). The part of the numerical model computing the wake convection is very time consuming, taking a significant portion of the computational time. As a consequence of the free-wake method, simulating more blades implies longer computational time as more vortex points need to be considered in the computation of the induced velocity.

The geometry change due to the rotor movement is computed in the fixed (Cartesian) reference frame with origin in the center of rotation (see Figure 3.1). From the geometry change in time, the perceived velocities are derived and the deformation occurrence is evaluated. The airfoils are panelled and the control points are defined with the aforementioned criteria.

3.1.3. Computation of the influence matrix

The problem now consists of finding the strength of the combination of sources/doublets distribution by satisfying the Dirichlet boundary condition and the Kutta condition.

Consider N surface panels and N_W additional wake panels. The Dirichlet boundary condition of zero normal flow to the body surface boundary solving the Laplace equation is based on the definition of the total inner velocity potential ϕ_i^*, given as the sum of the velocity potential on the interior of the body ϕ_i and the velocity potential of the free-stream ϕ_∞, which must be set to a constant value.

$$\phi_i^* = \phi_i + \phi_\infty = constant \tag{3.2}$$

For each collocation point, it is possible to write the following formulation of the Dirichlet boundary condition of zero normal flow in two-dimensions (from [37]):

$$\sum_{k=1}^{N} \frac{1}{2\pi} \int_{bodypanel} \mu \frac{\partial}{\partial n}\left(\frac{1}{r}\right) dS + \sum_{l=1}^{N_W} \frac{1}{2\pi} \int_{wakepanel} \mu \frac{\partial}{\partial n}\left(\frac{1}{r}\right) dS - \sum_{k=1}^{N} \frac{1}{2\pi} \int_{bodypanel} \sigma \left(\frac{1}{r}\right) dS = 0 \tag{3.3}$$

where r is the distance between a singularity point and the point where the potential is evaluated, S is the boundary surface about which flow is calculated and n is the normal vector to the panel surface element. A linear algebraic system of N equations results from writing equation 3.3 for each collocation point. A shorter form can be obtained by defining the aerodynamic influence coefficients as:

$$C_k = \frac{1}{2\pi} \int \frac{\partial}{\partial n}\left(\frac{1}{r}\right) dS \Big|_k \tag{3.4}$$

$$C_l = \frac{1}{2\pi} \int \frac{\partial}{\partial n}\left(\frac{1}{r}\right) dS \Big|_l \tag{3.5}$$

$$B_k = -\frac{1}{2\pi} \int \left(\frac{1}{r}\right) dS \Big|_k \tag{3.6}$$

from which equation 3.3 can be rewritten, at each control point, as:

$$\sum_{k=1}^{N} C_k \mu_k + \sum_{l=1}^{N_W} C_l \mu_l + \sum_{k=1}^{N} B_k \sigma_k = 0 \tag{3.7}$$

Both the sources σ and the doublets μ are unknowns. In order to compute the analytical solution, an assumption must be made. Therefore, the source strength is assumed to be given by the total potential that the element perceives:

$$\sigma = -\frac{\partial \phi}{\partial n} \tag{3.8}$$

which is computed in the numerical code as the sum of the source term from the perceived velocity due to movement of airfoil, the source term from the perceived velocity due to windspeed and the source term due to wake induction.

Now, the strengths of the doublets distributed over the airfoil μ_k are the only unknowns, since σ was computed, the aerodynamic influence coefficients are known (B_k and C_k from the problem geometry and C_l from the location of the wake at each time step) and the wake strengths μ_l are known since their values don't change in time. The final version of the Dirichlet equations to compute μ_k becomes:

$$\sum_{k=1}^{N} C_k \mu_k = -\sum_{l=1}^{N_W} C_l \mu_l - \sum_{k=1}^{N} B_k \sigma_k \tag{3.9}$$

where the right-hand side (RHS) consisting of the sum of the wake induced potential and source term is known.

In addition to the N equations from the Dirichlet boundary condition, the Kutta condition must be satisfied in the vortex panel method. The Kutta condition is applied at the trailing edge and it states that the wake doublet of strength μ_W is equal and opposite to the difference of strengths of the final and initial doublets of the airfoil, respectively μ_1 and μ_N.

$$\mu_1 - \mu_N + \mu_W = 0 \tag{3.10}$$

For each airfoil, one linear equation is added by the Kutta condition inside the doublets influence matrix.

3.1.4. Computation of the solution in terms of vortex strength

From the final system of equations, the solution can be easily found numerically by inverting the doublets influence matrix and multiplying it by the RHS. The distribution of vortex panel strength which cause the body to be a streamline of the flow is obtained. Finally, the doublets vector is distributed over the airfoils and the doublets obtained from the Kutta condition are transformed into new wake vortex elements. The wake is also trimmed to a maximum length, which was prescribed in a separate settings file, and the results of each time step are saved.

3.1.5. Secondary outputs

This subsection deals with the secondary outputs which can be computed at the end of the simulation, when the vortex strength distribution is known at each time step. Since the analysis of the hydrodynamic response of the vertical-axis tidal turbines of Chapter 5 will focus on the time evolution of the velocity triangles and of the hydrodynamic coefficients, the equations for the computation of these quantities are provided. The convention followed by the code is illustrated in Figure 3.1. Equations for the computation of possible additional results can be found in the Appendix A.2.

The relative velocity U_{rel} on a 2D blade element of a vertical-axis tidal turbine is given at each time step by the sum of the incoming tidal current velocity U_∞, the rotational speed ΩR, the induced velocity $U_{induced}$ and, if present, the surge velocity U_{surge}:

$$\vec{U}_{rel} = \vec{U}_\infty + \vec{\Omega} R + \vec{U}_{induced} + \vec{U}_{surge} \tag{3.11}$$

The induction on the point in analysis is calculated by adding the velocity induced by the wake elements U_{wake} and the velocity induced by the doublets/sources distribution over the airfoils $U_{otherairfoils}$.

$$\vec{U}_{induced} = \vec{U}_{wake} + \vec{U}_{otherairfoils} \tag{3.12}$$

The relative velocity can be further decomposed either in horizontal and vertical direction:

$$U_{rel,x} = U_\infty + U_{disp,x} + U_{induced,x} = U_\infty + \Omega R \cos\Theta + U_{surge} + U_{induced,x} \tag{3.13}$$

$$U_{rel,y} = U_{disp,y} + U_{induced,y} = \Omega R \sin\Theta + U_{induced,y} \tag{3.14}$$

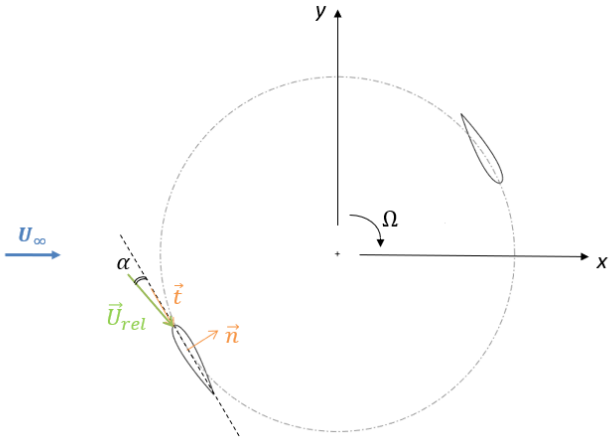

Figure 3.1: Frame of reference and rotor visualization in the U2DiVA code.

where Θ is the airfoil angular position in [°] and R the rotor radius in [m], or in normal and tangential direction as:

$$U_n = U_{rel,x}\cos\Theta + U_{rel,y}\sin\Theta \tag{3.15}$$

$$U_t = U_{rel,x}\sin\Theta - U_{rel,y}\cos\Theta \tag{3.16}$$

In lift-driven VATs, the velocity components vary in time depending on the azimuthal position of the airfoil Θ, with the exception of the constant U_∞. Consequently, the angle of attack at the blade is computed as:

$$\alpha = \tan^{-1}\frac{U_n}{U_t} \tag{3.17}$$

Knowing the time evolution of the velocity triangles at the control points, the instantaneous pressure coefficient can be calculated on each panel from Bernoulli's equation as:

$$C_{P,i} = 1 - \left(\frac{U_{t,i}}{U_\infty}\right)^2 - \frac{2}{U_\infty^2}\frac{\delta\mu}{\delta t} \tag{3.18}$$

where $U_{t,i}$ is the tangential velocity at the control point of the i^{th} panel and the term $-\frac{2}{U_\infty^2}\frac{\delta\mu}{\delta t}$ is the mass acceleration term, including the time derivative of the doublets $\frac{\delta\mu}{\delta t}$. The pressure distribution over the surface of the lifting body is used to compute the distribution of the force coefficients normalized by the diameter D at each time step in x- and y-direction:

$$C_{Fx,i} = \frac{-C_{P,i}\, l_i\, \vec{n}x_i}{D} \tag{3.19}$$

$$C_{Fy,i} = \frac{-C_{P,i}\, l_i\, \vec{n}y_i}{D} \tag{3.20}$$

where l_i is the panel length and $\vec{n}x_i$ and $\vec{n}y_i$ are the projections of the normal unit vector to the i^{th} panel respectively in x- and y-direction. The force coefficients over the entire airfoil are given by the sum of the coefficients of all the panels:

$$C_{Fx} = \sum_{i=1}^{N_{panels}} C_{Fx,i} \tag{3.21}$$

$$C_{Fy} = \sum_{i=1}^{N_{panels}} C_{Fy,i} \tag{3.22}$$

From these coefficients it is possible to compute the forces per unit length of the rotor at the 2D blade section as:

$$F_x = \frac{1}{2}\rho U_\infty^2 D C_{Fx} \tag{3.23}$$

$$F_y = \frac{1}{2}\rho U_\infty^2 D C_{Fy} \tag{3.24}$$

where ρ is the density of sea water of around $1025 kg/m^3$. For a rotor of number of blades B, the total thrust and lateral force coefficients, respectively C_{Fx}^{TOT} and C_{Fy}^{TOT}, are computed by the sum of the force coefficients on each blade k:

$$C_{Fx}^{TOT} = \sum_{k=1}^{B} C_{Fx}(k) \tag{3.25}$$

$$C_{Fy}^{TOT} = \sum_{k=1}^{B} C_{Fy}(k) \tag{3.26}$$

The distribution of torque coefficient C_M over the airfoil is calculated from the force coefficients and the total torque coefficient from the sum of this distribution as reported in the equations below.

$$C_{M,i} = \frac{C_{Fx,i}\Delta y_i - C_{Fy,i}\Delta x_i}{R} \tag{3.27}$$

$$C_M = \sum_{i=1}^{N_{panels}} C_{M,i} \tag{3.28}$$

where Δx_i and Δy_i are the distances in x- and y-direction of the control point of the i^{th} panel from the center of momentum. From the torque coefficient, the instantaneous torque per unit length acting on the blade section can be found at each time step as:

$$M = \frac{1}{2}\rho C_M U_\infty^2 2R^2 \tag{3.29}$$

The instantaneous power coefficient is computed from the rotor torque coefficient and the tip speed ratio $\lambda = \frac{\omega R}{U_\infty}$ as:

$$C_{power} = \lambda \cdot \sum_{k=1}^{B} C_M(k) \tag{3.30}$$

Therefore, the instantaneous power per unit length of the rotor produced by the tidal turbine is:

$$P = \frac{1}{2}\rho C_{power} U_\infty^3 D \tag{3.31}$$

3.2. Integration of the 2D floating platform's motions

The integration of the floating platform's motions in the U2DiVA code is realized by prescribing them to the time evolution of the rotor position defined in the *geometry input file*. At each time step, the control points of the airfoils are translated by a fixed angular displacement $\Delta\theta$[°] over the rotor while the center of momentum is fixed in the origin, obtaining the position vector of the points describing the rotor geometry $(\vec{X}(t), \vec{Y}(t))$. Since the model represents the rotor in two dimensions, motions in only three degrees of freedom can be integrated and simulated: surge, sway and yaw. The platform's motions are imposed to the rotor geometry evolution in time, resulting in the new position vector $(\vec{X}'(t), \vec{Y}'(t))$ defined in equations 3.32 and 3.33. The instantaneous values of surge displacement X_{surge} and sway displacement Y_{sway} simultaneously translate the airfoils and the center of momentum in x- and y- direction, respectively. The rotor displacement due to yaw motion centered around a point $P(X_P, Y_P)$ with yaw angle θ_{yaw} is calculated with a rotation matrix.

$$\vec{X}'(t) = X_P + (\vec{X}(t) - X_P)\cos\theta_{yaw}(t) - (\vec{Y}(t) - Y_P)\sin\theta_{yaw}(t) + X_{surge}(t) \tag{3.32}$$

$$\vec{Y}'(t) = Y_P + (\vec{Y}(t) - Y_P)\cos\theta_{yaw}(t) + (\vec{X}(t) - X_P)\sin\theta_{yaw}(t) + Y_{sway}(t) \tag{3.33}$$

In this project, the platform's motions are assumed to be induced by regular waves in order to simplify the analysis and interpretation of the results. The theory of regular waves is briefly presented in the Appendix A.1. The motion of a floating platform under regular waves is described as harmonic, with circular frequency of the encounter expressed by:

$$\omega_e = \omega_{wave} - kV\cos\gamma \tag{3.34}$$

where ω_{waves} is the circular wave frequency in [rad/s], k is the wave number in [rad/m], V is the forward speed of the platform (here with zero forward velocity $V = 0$m/s) and γ is the angle between the platform

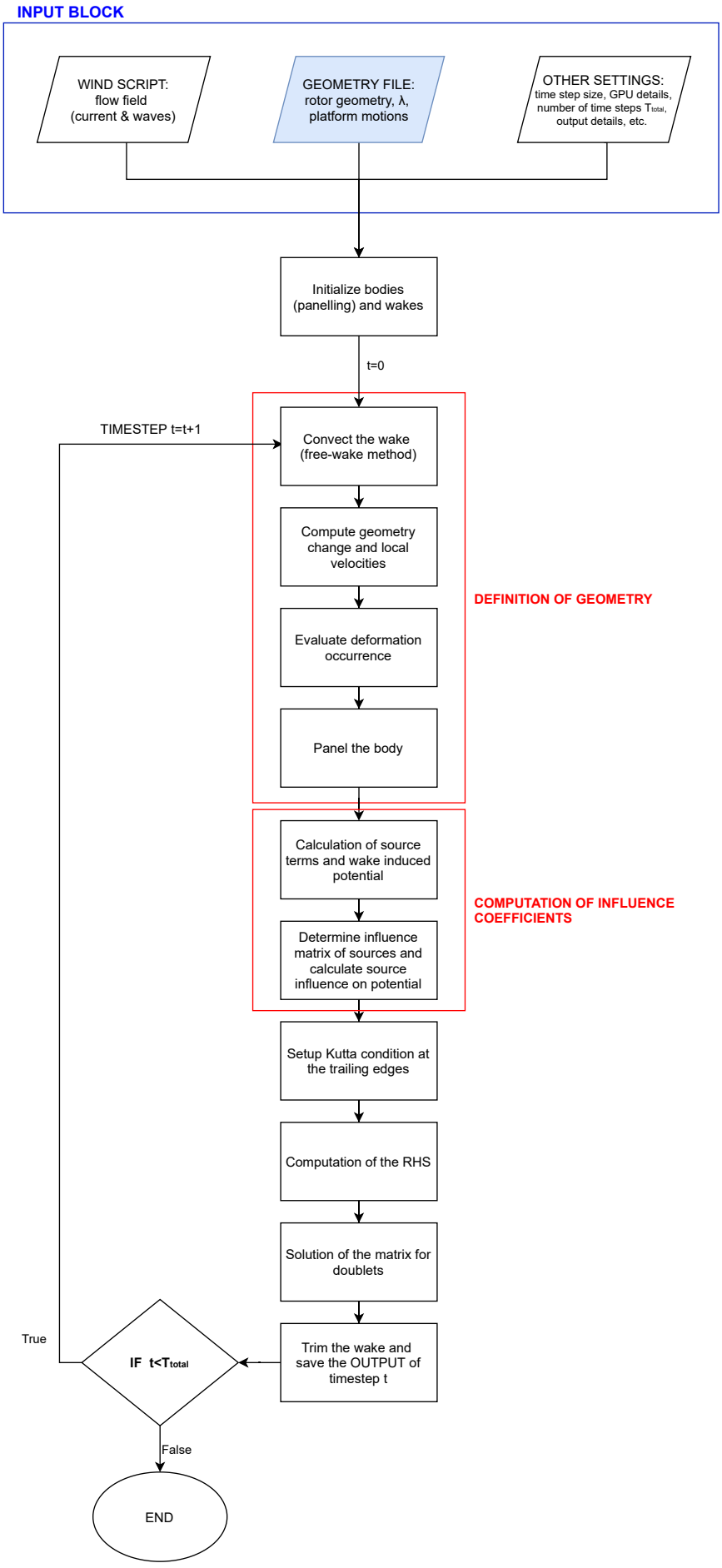

Figure 3.2: Flowchart of the TU Delft in-house U2DiVA code.

velocity and the incoming wave velocity in [°]. The amplitude of platform's surge motion A_{surge}[m/s], sway motion A_{sway}[m/s] and yaw motion ξ_{yaw}[°] can be defined from the wave amplitude, and the phases of the motions are respectively Φ_{surge}, Φ_{sway} and Φ_{yaw} in [°]. Surge motion is described as harmonic motion induced by regular waves in the direction of the tidal current. From integration of the surge velocity U_{surge} of equation 3.35, the equation 3.36 of the surge displacement X_{surge} to implement inside the *geometry input file* is obtained.

$$U_{surge}(t) = \mathrm{Re}\left(A_{surge} \cdot \mathrm{e}^{-\mathrm{i}(\omega_e t - \Phi_{surge})}\right) \tag{3.35}$$

$$X_{surge}(t) = \mathrm{Re}\left(-\mathrm{i} \cdot \frac{A_{surge}}{\omega_e} \cdot \mathrm{e}^{-\mathrm{i}(\omega_e t - \Phi_{surge})}\right) \tag{3.36}$$

The sway motion is modelled similarly, but in the cross-flow direction, i.e. the y-direction in the convention of the U2DiVA code. The sway velocity U_{sway} and displacement Y_{sway} are defined respectively in equations 3.37 and 3.38.

$$U_{sway}(t) = \mathrm{Re}\left(A_{sway} \cdot \mathrm{e}^{-\mathrm{i}(\omega_e t - \Phi_{sway})}\right) \tag{3.37}$$

$$Y_{sway}(t) = \mathrm{Re}\left(-\mathrm{i} \cdot \frac{A_{sway}}{\omega_e} \cdot \mathrm{e}^{-\mathrm{i}(\omega_e t - \Phi_{sway})}\right) \tag{3.38}$$

Yaw motion is modelled as harmonic yaw angle θ_{yaw} as in equation 3.39.

$$\theta_{yaw}(t) = \mathrm{Re}\left(\xi_{yaw} \mathrm{e}^{-\mathrm{i}(\omega_e t - \Phi_{yaw})}\right) \tag{3.39}$$

Alternatively, the platform's motions could be integrated in the code by modelling flow acceleration in the *wind script file*. For example, in the case of surge motion the instantaneous surge velocity is added to the current speed in x-direction. Simulations integrating the surging motion in the two input files were compared and the simulation outputs were found to be approximately the same, with a difference in the mean squared error of the hydrodynamic coefficients of the order of magnitude of 10^{-4}. Nevertheless, the *geometry input file* is preferably modified since it allows to distinguish the effect of surge on the inflow field perceived at the blade into the component deriving from relative flow acceleration and the one deriving from the evolving rotor position with respect to the wake. In fact, since the code computes the velocity by derivation of the airfoils position in time, introducing the platform's motion as the change of rotor position in time in the *geometry input file* accounts for both the effects of position and velocity introduced by the wave-induced motion.

3.3. Sensitivity study

Since the U2DiVA code uses a numerical method for calculating the flow around the VATT's blades, the sensitivity of the numerical model to its inputs should be verified. The sensitivity study is conducted for two existing lift-driven vertical-axis tidal turbines, the Haineng 1 and the Kobold (see Figure 3.3), which hydrodynamic response to surging motion will be studied in Chapter 5. The first turbine analysed is the Haineng 1 300kW [19], which was developed by Harbin Engineering University (HEU) of China as consisting of two rotors of 150kW installed on a floating catamaran and was tested from 2012 to 2013 in Zhoushan islands (China). The second turbine of this study is the Kobold [20], patented by Ponte di Archimede International S.p.A. (Italy) in 1998 and further developed and tested at the university of Naples Federico II and at the research institute INSEAN, both located in Italy. The first Kobold pilot plant was installed in 2001 in the Strait of Messina (Italy) [48], following which new projects emerged for prototypes to be installed in San Bernardino strait (Philippines), Bali (Indonesia) and Zhoushan islands (China) [20]. The geometry of the two turbines is reported in Table 3.1, with the information retrieved from [38] for the Haineng 1 and from [20, 28, 48] for the Kobold. Both turbines are straight-bladed and were designed for floating applications. Although the HLIFT18 airfoil was designed for the Kobold turbine [28], data about this airfoil couldn't be found and the NACA0018 is used instead.

The operating and inflow conditions of the simulations run for the sensitivity study are reported in Table 3.2. The parameters are found from the literature, from [38] for the Haineng 1 turbine and from [20] for the Kobold turbine.

In this section, the sensitivity of the code to airfoil panelling and time step size is investigated. First, the effect of the number of panels at a given time step size on the accuracy and computational cost is described in 3.3.1 for both turbines. Similarly, the convergence of the hydrodynamic coefficients for decreasing time

Table 3.1: Geometry of the Haineng 1 [38] and the Kobold [20, 28, 48] vertical-axis tidal turbines.

TURBINE	Geometry of the VATT rotor					
	R [m]	c [m]	B	Airfoil	l_0 [m]	Φ_0 [°]
Haineng 1	2.0	0.9	2	NACA0018	0.25c	0
Kobold	3.0	0.4	3	NACA0018 (HLIFT18)	0.25c	0

Table 3.2: Operating and inflow conditions used in the sensitivity analysis of the U2DiVA code for the Haineng 1 turbine [38] and the Kobold turbine [20].

TURBINE	λ	U_∞[m/s]
Haineng 1	3.0	3.5
Kobold	2.8	2.0

step size at a given panelling is discussed in 3.3.2. Finally, some reflections on the findings of the sensitivity study and on the limitations of input parameters of vortex panel methods are presented in 3.3.3.

(a) Haineng 1 VATT [38]

(b) Kobold VATT [20]

Figure 3.3: Visualizations of the Haineng 1 (a) and the Kobold (b) vertical-axis tidal turbines.

3.3.1. Sensitivity to the panelling

The panelling of the airfoils is generated using chord-wise cosine spacing and closed trailing edge for distributing a number of panels N_{panels} over the airfoil, as described in [49, 50]. The cosine spacing distributes more panels close to the trailing edge and leading edge, in order to obtain a finer resolution on critical points for the study of the flow phenomena. Closing the trailing edge is also necessary to apply the Kutta condition. The point distribution is obtained through the following equations:

$$x = \frac{1}{2}\left(1 - \cos\beta\right) \tag{3.40}$$

$$y = \frac{tc}{0.2}\left(0.2969\sqrt{x} - 0.126 \cdot x - 0.35160 \cdot x^2 + 0.2843 \cdot x^3 - 0.1036 \cdot x^4\right) \tag{3.41}$$

where tc is the airfoil's thickness-to-chord ratio and the angle β is given by a uniform distribution of N_{panels} points between 0° and 360°. Several panelling options from 20 up to 190 panels are explored in this work. The simulations are conducted assuming a displacement of the airfoil of 2.5° per time step, as was used in other studies employing the U2DiVA code [47, 51], and ran for four full rotor revolutions.

Increasing the number of panels covering each airfoil means increasing the resolution of the grid and providing smoother simulation results. The curves of the normalized force coefficients of the Haineng 1 VATT over one rotation for increased grid resolution can be observed in Figure A.1 of the Appendix. The effect of increasing N_{panels} on the quality of results can be quantified by defining the mean squared error (MSE), taking the results of the simulation with 190 panels as reference for the highest accuracy, as:

$$MSE = \frac{1}{M_{time}} \sum_{j=1}^{M_{time}} C_j - C_{j,ref} \tag{3.42}$$

where M_{time} is the number of time steps of the simulation, C_j is the force coefficient for the simulation with $N_{panels} < 190$ and $C_{j,ref}$ is the force coefficient for the 190 panels simulation at the j^{th} time step. The MSE of the force coefficients over the 3^{rd} and 4^{th} rotations as function of the number of panels is reported in Figure 3.4. From the two graphs, it can be seen that panelling above 90 panels provides sufficiently accurate results, and that the error further reduces when adding more panels. Using 150 panels would be sufficient to obtain a good representation of the airfoils. However, since it was observed that the panelling doesn't strongly influence the computational time as it simply affects the dimension of the solution matrix, the highest accuracy 190 panels will be used in the simulations of Chapter 4 and Chapter 5.

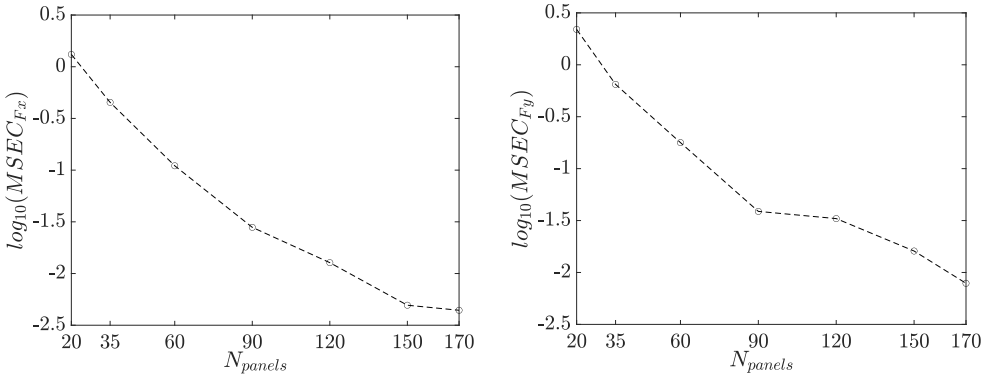

(a) Thrust force coefficient (b) Lateral force coefficient

Figure 3.4: Convergence of the MSE of the force coefficients of the Haineng 1 turbine (U_∞=3.5m/s,λ=3.0) for increasing number of panels with respect to 190 panels.

Compared to the Haineng I, the results of the simulations for the Kobold turbine are less sensitive to the variation of the number of panels. This is mostly noticeable in Figure 3.5, since the MSE starts from very low values with few panels and it converges steadily to very small MSE for large number of panels. Also, the normalized force coefficients over one rotation plotted in the Figure A.2 of the Appendix show small discrepancy for different number of panels. The different sensitivity to panelling of the two turbines could be related to their geometries, especially to parameters as the number of blades or the solidity.

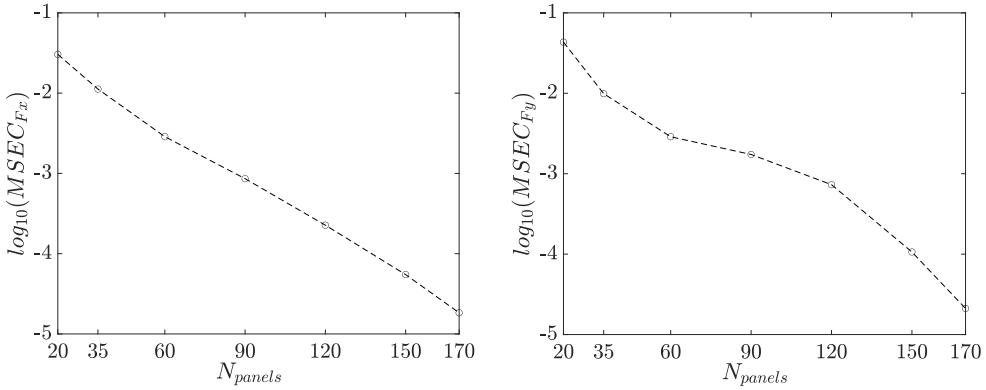

(a) Thrust force coefficient (b) Lateral force coefficient

Figure 3.5: Convergence of the MSE of the force coefficients of the Kobold turbine (U_∞=2.0m/s,λ=2.8) for increasing number of panels with respect to 190 panels.

3.3.2. Sensitivity to the time step size

The sensitivity study of the time step size is conducted for angular displacement per time step from 0.5° up to 10°, assuming 190 panels for each airfoil as it was found to be a highly accurate grid resolution in 3.3.1. Simulations are also run for smaller time steps, but this sharply increases the computational time and can

lead to numerical instability, as shown in Figure 3.6. For this reason, time steps below 0.5° are disregarded.

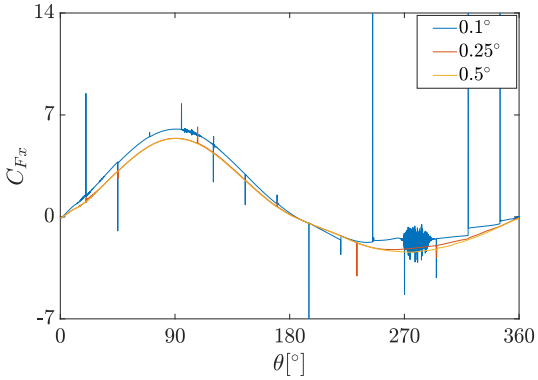

Figure 3.6: Effect of extremely small time steps on the normalized thrust coefficient at one blade of the Haineng 1 turbine (U_∞=3.5m/s,λ=3.0) over one rotation.

Since the time step size has a direct influence on the computational time, the aim of this study is to find a sufficiently small time step to represent the results with good accuracy, but not excessively small in order to have a reasonable computational time. Relatively small time steps lead to more accurate results than large time steps, since the solution is computed in more points in time. For decreasing time step size, smoother results are obtained and different magnitude of peak values is reached. In Figure A.3 of the Appendix, the curves of the force coefficients of the Haineng 1 turbine for different time step sizes are compared, and the more segmented curves corresponding to large time steps can be easily distinguished from the smoother curves resulting from small time steps. However, when the time step size is extremely small, such as 0.1° or 0.25°, numerical instabilities can rise as displayed in Figure 3.6. With extremely small time steps, the shedding of vorticity is more frequent and many vortices are generated at a reduced distance. This causes large variations of the induced velocity, in particular at the trailing edge, and therefore the discrepancies and spikes of the graph. The effect of extremely small time step sizes is particularly evident when the airfoil passes in the downwind side of the rotor (between 180° and 360°).

Taking the results of the simulation with 0.5° time step size as a reference, the MSE of the results can be compared as in Figure 3.7 and the convergence for decreasing time step size can be observed.

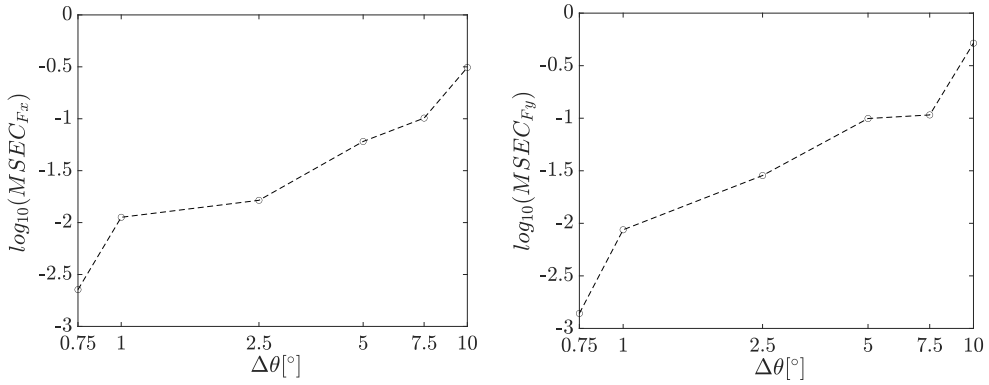

(a) Thrust force coefficient (b) Lateral force coefficient

Figure 3.7: Convergence of the MSE of the force coefficients at one blade of the Haineng 1 turbine (U_∞=3.5m/s,λ=3.0) for decreasing time step size with respect to a displacement of 0.5°per time step.

Similarly to the Haineng 1, the main effect of large time steps on the force coefficients of the Kobold turbine is a more segmented shape, with smaller peak values. For example, Figure A.4 in the Appendix displays the 10° curve following quite closely the more accurate 0.5° curve, with the exception of the peak areas. The Kobold VATT shows faster convergence rate with decreasing time step size than the Haineng 1, thus being less sensitive to the time step size. The MSE starts from low values at large time steps and quickly converges for smaller time steps, as represented in Figure 3.8.

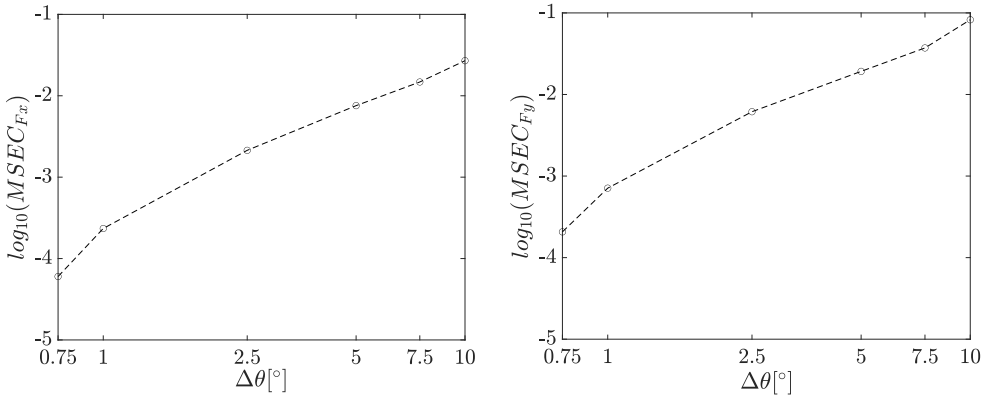

(a) Thrust force coefficient (b) Lateral force coefficient

Figure 3.8: Convergence of the MSE of the force coefficients at one blade of the Kobold turbine (U_∞=2.0m/s,λ=2.8) for decreasing time step size with respect to a displacement of 0.5°per time step.

3.3.3. Discussion on the sensitivity analysis

From the analysis conducted in 3.3.1 and 3.3.2, it can be concluded that the number of panels distributed over the airfoils and the time resolution largely influence the quality of the simulation results computed via the U2DiVA code. By increasing the number of panels and the number of time steps per rotation, the accuracy of panel methods increases, as well as the computational cost. The latter is mostly affected by the time step size, since it defines the time sampling over the rotation. Instead, refining the grid by introducing more panels only marginally affects the computational time since it increases the dimension of the solution matrix. From the comparison of the simulation results of the Haineng 1 and the Kobold, it was found that the sensitivity to the code inputs depends on the rotor geometry. In this case, the Haineng 1 turbine is more sensitive to both the inputs.

Compared to CFD simulations, in which higher-order and denser grids increase the accuracy of the solution, vortex panel methods are less sensitive to the panelling, as long as the trailing edge is closed in order to apply the Kutta condition correctly. The most important requirement for panel methods is having a sufficiently fine panelling of the airfoil surface in order to describe the geometry over which the flow is being resolved, particularly dense at the trailing edge [52]. However, an excessive number of panels might not improve significantly the solution and could introduce numerical error, e.g. matrix inversion stability [52]. Furthermore, vortex panel methods require a computational time of at least one order of magnitude lower than CFD. For example, in [52] a computational time of few seconds of the potential-flow method is compared to several minutes of CFD simulations. The U2DiVA code is characterised by a computational time of the order of magnitude of minutes to few hours, depending on the number of time steps simulated. A significant fraction of the computational time is spent on the implementation of the free-wake method. The respective computational time of CFD simulations is expected to be of the order of several hours or days. The setting-up of the CFD simulations is also a more time-consuming process, consisting of building a sufficiently fine grid, allowed to move with platform's motions, and selecting other simulation inputs accordingly, such as the time step size.

Before defining the number of panels and the time step size to be used in the simulations of this project, one additional consideration about the interaction of panelling and time stepping in the U2DiVA code should be mentioned. The two inputs studied in this chapter cannot be used in every combination, as numerical instabilities rise when the non-dimensional distance of the trailing edge vortex $\frac{\Delta x_{TE}}{c}$ is smaller than the size of the panels at the trailing edge. This distance can be computed from the displacement $\Delta\theta$ at each time step of the simulation as:

$$\frac{\Delta x_{TE}}{c} = \frac{\Delta\theta}{2\pi}\frac{D/2}{c} \tag{3.43}$$

while the size of the panels at the trailing edge depends on the number of panels selected, decreasing with increasing N_{panels}. The numerical instability introduced by an incorrect combination of panelling and time step size can be observed in the example provided in Figure 3.9, which compares the thrust coefficient of the Haineng 1 turbine obtained with 20 panels and 1° time step size to the correct combination of 190 panels with 1°.

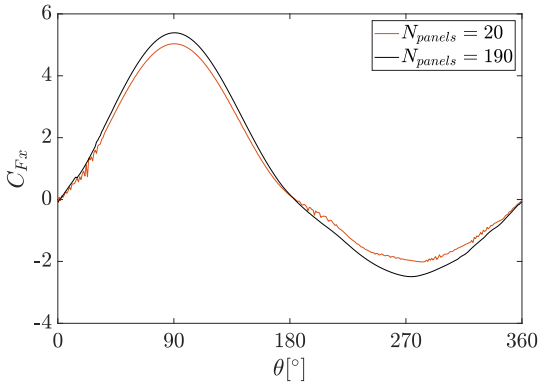

Figure 3.9: Comparison of the horizontal force coefficient of the Haineng 1 turbine with 20 and 190 panels over one rotation for 1° time step.

In conclusion, the U2DiVA code is a time-effective tool compared to computational fluid dynamics in terms of setting-up and simulation time, with the limitation of the potential-flow assumption. The sensitivity of the code to the panelling and time step size should be studied before running a simulation with given inputs in order to define the values of N_{panels} and $\Delta\theta$ as a trade-off between accuracy of results and computational time while considering the limits in their combination. From the results of this chapter and taking into account the aforementioned considerations, the simulations in this work are run with **190 panels** and with a displacement per time step in the range of **1°to 5°**.

4

Verification of the 2D vortex panel method against 2D CFD

The retrieved scientific literature dealing with the numerical modelling of floating vertical-axis tidal turbines exclusively uses CFD simulations in order to gain insights on the uncoupled system dynamics, as was discussed in Chapter 2. Although computational fluid dynamics represents the highest level of fidelity and accuracy among the numerical modelling techniques for VATs, it has the drawback of being computationally expensive and extremely sensitive to several inputs (e.g. meshing, differentiation scheme and turbulence model). In order to reduce the complexity and computational time and to facilitate the interpretation of results, the unsteady two-dimensional free-wake vortex panel code U2DiVA [47] was adopted in this project.

In this chapter, the U2DiVA code is verified against the results from the scientific literature using a 2D CFD approach for the analysis of the effect of floating platform's motions on the hydrodynamic coefficients of a vertical-axis tidal turbine. First, the assumptions and inputs to the simulations are described in section 4.1. Second, the verification for surge, sway and yaw, as independent or coupled motions, is presented respectively in sections 4.2, 4.3 and 4.4. The importance of viscosity and compressibility corrections and their possible introduction in the U2DiVA code is discussed in section 4.5. Eventually, the comparison of the results is provided in section 4.6, with reflections on the accuracy of this alternative approach.

4.1. Verification set-up

In order to reproduce the results of the scientific literature, the following assumptions of the 2D CFD method must be applied to the U2DiVA code:

- The tidal current speed U_∞ is assumed to be uniform in the considered horizontal plane, with no influence of waves.
- The rotational speed of the rotor Ω is constant.
- The platform motion is simulated as simple harmonic motion:

$$X_{surge}(t) = \xi_{surge} \sin(\omega_e t + \Phi_{surge}) \tag{4.1}$$

$$Y_{sway}(t) = \xi_{sway} \sin(\omega_e t + \Phi_{sway}) \tag{4.2}$$

$$\theta_{yaw}(t) = \xi_{yaw} \sin(\omega_e t + \Phi_{yaw}) \tag{4.3}$$

  where ξ_{surge} and ξ_{sway} are respectively the surge and sway amplitude in [m], ξ_{yaw} is the yaw amplitude in [rad], ω_e is the platform's motions frequency in [rad/s] and $\Phi_{surge}, \Phi_{sway}$ and Φ_{yaw} are the phase angles of surge, sway and yaw motion respectively. The platform itself is not considered, but only the effect of its motions on a vertical-axis turbine with axis perpendicular to the calm surface and straight blades in unbounded uniform flow is studied.

- Differently from the definitions of the force coefficients in 3.1.5, in this chapter C_{Fx} and C_{Fy} indicate the total rotor load coefficients, following the convention of the research papers using the 2D CFD approach.

Table 4.1: Geometry of the HEU [41, 42] and the Haineng 1 [38] vertical-axis tidal turbines.

TURBINE	Geometry of the VATT rotor					
	R [m]	c [m]	B	Airfoil	l_0 [m]	Φ_0 [°]
HEU	0.4	0.12	2	NACA0018	0.3c	0
Haineng 1	2.0	0.9	2	NACA0018	0.25c	0

Table 4.2: Inflow and operating conditions for the verification simulations of the HEU [41, 42] and the Haineng 1 [38] vertical-axis tidal turbines.

TURBINE	Operating and inflow conditions							
	λ	U_∞[m/s]	ξ_{surge}[m]	ξ_{sway}[m]	ξ_{yaw}[rad]	ω_e[rad/s]	X_P[m]	Y_P[m]
HEU	2.5	1.0	0.2	0.2	$\frac{\pi}{18}$	1.0	-0.4	0
Haineng 1	2.0	3.5	0.6	0	0	1.4	0	0

As a consequence of these assumptions, the flow at each turbine section is similar and can be studied as two-dimensional. The geometry of the turbines inputted in the simulations is reported in Table 4.1. The operating and inflow conditions of the simulations for the verification are presented in Table 4.2. Notice that the phase of platform's motions is assumed to be 0°for all the platform's motions.

In the 2D CFD approach used in the literature, the rotation and platform motions are implemented by dividing the computational domain in regions and allowing the regions to rotate and translate in time (by means of dynamic mesh [38, 41, 42] or slipping grid method [40]). In the U2DiVA code, the rotation is implemented by translating the control points of each airfoil over the rotor by a fixed displacement per time step, obtaining the position vector $(\vec{X(t)}, \vec{Y(t)})$; then, the platform motions are implemented as forced oscillation of the rotor with time, by adding the harmonic contribution described in equations 4.1, 4.2 and 4.3 to the airfoils position vector as well as to the position of the center of momentum, obtaining the new position vector $(\vec{X'(t)}, \vec{Y'(t)})$ as was discussed in section 3.2. Equations 3.32 and 3.33 are used for including the platform's motions either as independent or coupled.

However, the 2D CFD simulations and the 2D panel method simulations have some minor differences in the assumptions, with a direct effect on the results:

- A larger time step (corresponding to a displacement of 5°) is assumed in the U2DiVA simulations, compared to the smaller time steps used in the literature, such as 1°in [40] or 3°in [41, 42].
- The airfoils rotate in opposite directions in the two methods: clockwise in the U2DiVA code and counter-clockwise in the 2D CFD approach. For this reason, the results of the rotor lateral force coefficient computed via the U2DiVA code are plotted as $-C_{Fy}$ for comparison with the 2D CFD results.

4.2. Verification of surging motion

The effect of surge motion on the rotor force coefficients computed via U2DiVA code is verified against the results of Wang et al. (2018) and Xu et al. (2019) presented respectively in [41] and [42]. The rotor geometry of the vertical-axis tidal turbine used in these studies, developed at Harbin Engineering University (HEU) in China, is reported in the first row of Table 4.1. The inflow current, operating parameters and surge conditions are provided in Table 4.2.

Figures 4.1 and 4.2 display the oscillations of the rotor load coefficients in time in x- and y-directions for the stand-alone HEU turbine in unbounded uniform flow, comparing the results reported in [41, 42] and computed via U2DiVA. Since the rotor thrust and lateral force coefficients are computed as the sum of the force coefficients on each airfoil, the loads oscillate periodically with fluctuation frequency of $B \cdot \Omega$ between almost straight envelopes. The extreme values are constant over the rotor revolutions as a result of the steady inflow and operating conditions experienced by the stand-alone turbine. When platform's surge is introduced, the unsteady motion induces variations in the envelopes of the force coefficients, which are no longer straight but oscillate with surge frequency. Therefore, low-frequency oscillations (ω_e) and high-frequency oscillations ($2 \cdot \Omega$) can be recognized in Figures 4.3 and 4.4. Surge motion impacts on the rotor loading by simultaneously increasing or decreasing the force coefficients in x- and y-direction. The increase in loading occurs when the surge velocity adds up to the uniform current velocity, increasing the instantaneous velocity perceived at the blades. When the surge velocity opposes the current velocity, the loading on the rotor decreases as a result

of the smaller perceived velocity. Consequently, the upper envelope of the rotor thrust coefficient oscillates periodically around the constant envelope found in the simulation without surging motion, with a slightly increased mean value. The lower envelope is hardly affected by surge motion, being very close to zero, but oscillates symmetrically to the upper envelope. Instead, the lateral force coefficient is affected equally in both directions, again with a slightly larger average value for the upper envelope compared to the results of the simulation without surging motion.

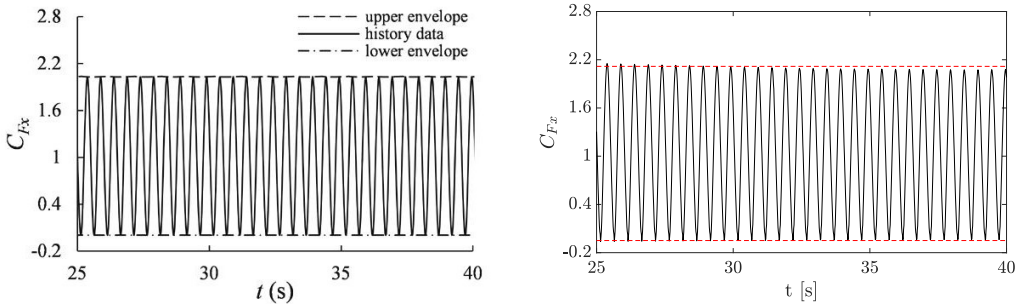

(a) Results of 2D CFD (b) Results of the U2DiVA code.

Figure 4.1: Time history curves of the rotor thrust coefficient for the stand-alone HEU turbine ($\lambda = 2.5$, $U_\infty = 1 m/s$) simulated via 2D CFD [41, 42] (a) and U2DiVA (b).

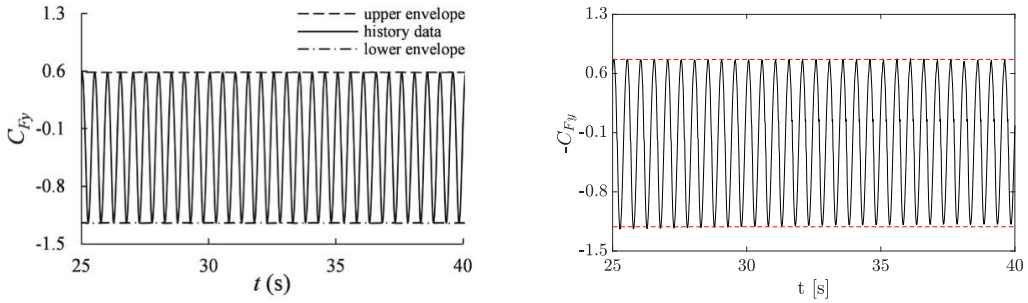

(a) Results of 2D CFD (b) Results of the U2DiVA code

Figure 4.2: Time history curves of the rotor lateral force coefficient for the stand-alone HEU turbine ($\lambda = 2.5$, $U_\infty = 1 m/s$) simulated via 2D CFD [41, 42] (a) and U2DiVA (b).

An overestimation of the maximum values by U2DiVA is noticeable on the upper envelopes of all simulation results, either in the only current case and under platform's surging motion. The overestimation is believed to be consequence of the potential-flow assumption at the base of the U2DiVA code, neglecting the viscous effects which are included instead in the 2D CFD computation.

A second verification of surge motion is performed against the results of the article by Sheng et al. (2016), who analysed the effect of surge motion on the Haineng 1 turbine [38]. However, the results presented by the authors are not possible to reproduce since the presented results are not consistent with the input values reported on the scientific paper (see the second row of Table 4.1 and Table 4.2). For example, the oscillation frequency of the force coefficients for the only current case should be $B \cdot \Omega = B \cdot \frac{\lambda U_{current}}{R} = 7$ rad/s with the given inputs. From the results of Sheng et al. reported in Figures 4.5(a), 4.6(a), 4.7(a) and 4.8(a), it can be observed that the load oscillation frequency due to the blades rotation is smaller than 7 rad/s. Nevertheless, U2DiVA simulations with the given inputs are run, and the results are presented and compared to the results of the scientific article in Figures 4.5, 4.6, 4.7 and 4.8. Again, two oscillation frequencies can be recognized: the low-frequency oscillation ω_e and the high-frequency oscillation $B \cdot \Omega$. The effect of surge motion on the envelopes of the force coefficients computed via U2DiVA is similar to the one observed in the results of the 2D CFD simulations, but the rotational frequency Ω and, as a consequence, the amplitude of load oscillations differ. In this case, the large overestimation of the results of the U2DiVA code compared to the CFD results, especially in the positive side (upper envelopes), mostly originates from different operating and / or inflow conditions.

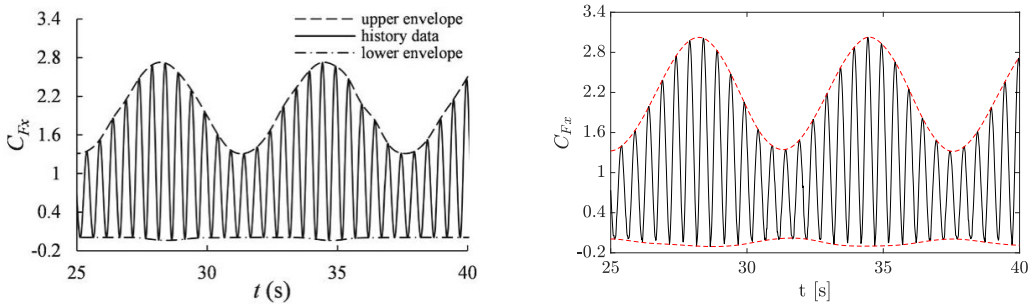

(a) Results of 2D CFD (b) Results of the U2DiVA code.

Figure 4.3: Time history curves of the rotor thrust coefficient for the HEU turbine under surging motion ($\lambda = 2.5$, $U_\infty = 1$m/s, $\xi_{surge} = 0.2$m, $\omega_e = 1$rad/s) simulated via 2D CFD [41, 42] (a) and U2DiVA (b).

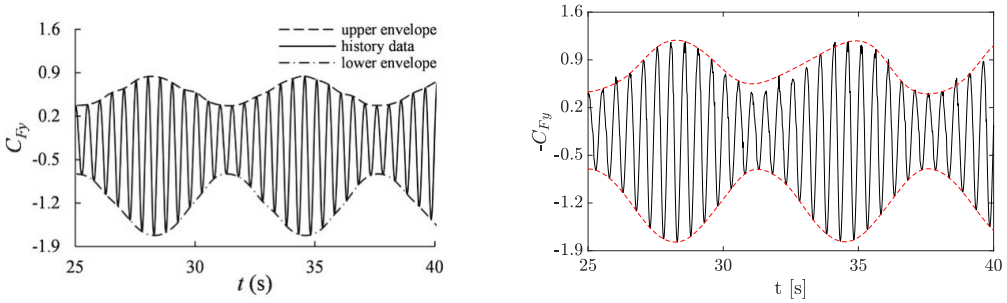

(a) Results of 2D CFD (b) Results of the U2DiVA code

Figure 4.4: Time history curves of the rotor lateral force coefficient for the HEU turbine under surging motion ($\lambda = 2.5$, $U_\infty = 1$m/s, $\xi_{surge} = 0.2$m, $\omega_e = 1$rad/s) simulated via 2D CFD [41, 42] (a) and U2DiVA (b).

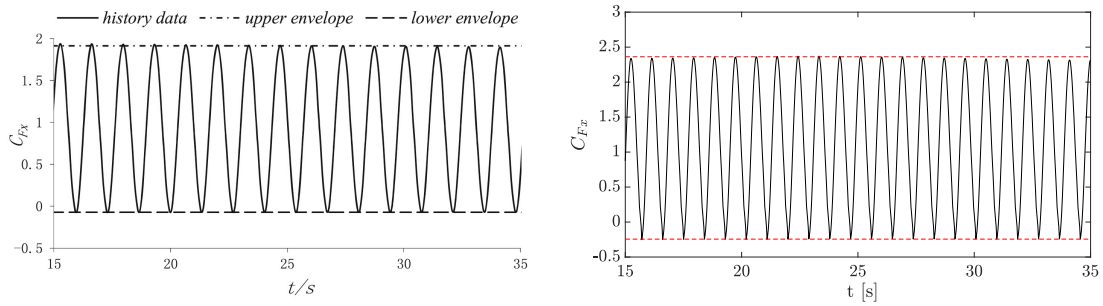

(a) Results of 2D CFD (b) Results of the U2DiVA code

Figure 4.5: Time history curves of the rotor thrust coefficient for the stand-alone Haineng 1 turbine ($\lambda = 2$, $U_\infty = 3.5m/s$) simulated via 2D CFD [38] (a) and U2DiVA (b).

4.3. Verification of swaying motion and surging&swaying coupled motions

The U2DiVA code is verified for swaying motion against the results of Xu et al. (2019), who researched the effects of platform translation motions in two-dimensions on the HEU turbine [42]. The geometry of the turbine and the inflow condition, operating parameters and sway conditions are listed in the first row of Table 4.1 and Table 4.2 respectively.

The effect of sway motion on the hydrodynamic loads of the HEU vertical-axis tidal turbine is similar to what was previously described in the case of surge. The loads in x- and y-directions oscillate with low-frequency ω_e and high-frequency 2Ω. The fluctuation frequency of the envelopes is coherent with swaying frequency ω_e, but the amplitude of oscillation due to swaying motion (Figures 4.9 and 4.10) is small compared to the effect of surging motion with the same amplitude and frequency (Figures 4.3 and 4.4). Moreover, the upper envelopes of the force coefficients are overestimated compared to the results of the 2D CFD simu-

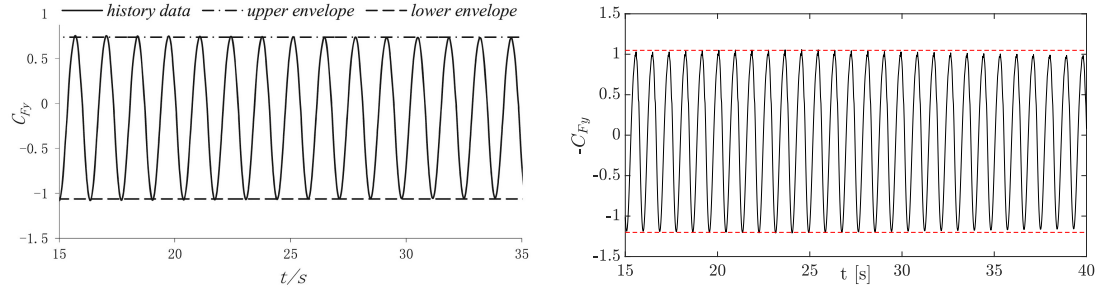

(a) Results of 2D CFD (b) Results of the U2DiVA code

Figure 4.6: Time history curves of the rotor lateral force coefficient for the stand-alone Haineng 1 turbine ($\lambda = 2$, $U_\infty = 3.5m/s$) simulated via 2D CFD [38] (a) and U2DiVA (b).

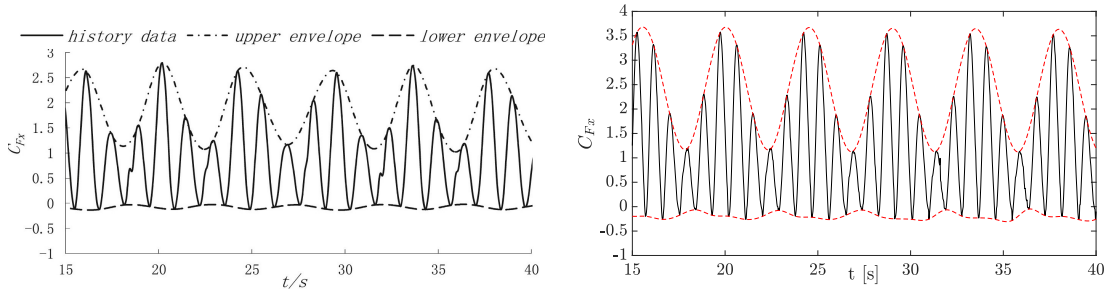

(a) Results of 2D CFD (b) Results of the U2DiVA code

Figure 4.7: Time history curves of the rotor thrust coefficient for the Haineng 1 turbine under surging motion ($\lambda = 2$, $U_\infty = 3.5$m/s, $\xi_{surge} = 0.6$m, $\omega_e = 1.4$rad/s) simulated via 2D CFD [38] (a) and U2DiVA (b).

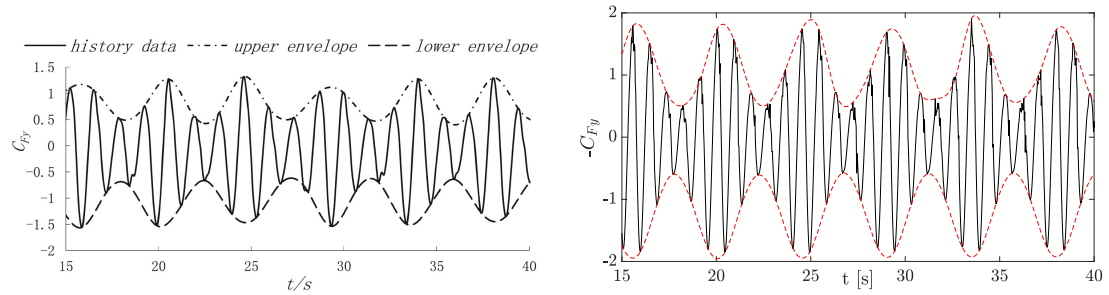

(a) Results of 2D CFD (b) Results of the U2DiVA code

Figure 4.8: Time history curves of the rotor lateral force coefficient for the Haineng 1 turbine under surging motion ($\lambda = 2$, $U_\infty = 3.5$m/s, $\xi_{surge} = 0.6$m, $\omega_e = 1.4$rad/s) simulated via 2D CFD [38] (a) and U2DiVA (b).

lations due to the assumptions at the base of the U2DiVA code. While surging motion induces symmetrical changes in the envelopes of the time evolution of the force coefficients, swaying motion instantaneously shifts vertically the lower and upper envelopes. Since sway occurs in cross-flow direction, its effect on the rotor thrust coefficient is limited. The effect of sway on the thrust coefficient (Figure 4.9) is mainly visible on the upper envelope, while the lower envelope is barely affected since its average value is close to zero. The lateral force coefficient depicted in Figure 4.10 is more noticeably affected by swaying motion which shifts both the envelopes upwards or downwards depending on the instantaneous direction of sway velocity. Moreover, since sway introduces an additional velocity component, the average loading is slightly larger than for the only current case.

The results of the 3 degrees of freedom simulations, including rotation, surge and sway, are presented in Figures 4.11 and 4.12. The variations induced by surging motions evidently prevail on the effect of swaying motion, especially in x-direction. Because of the little difference between Figures 4.3 and 4.11, the effect of

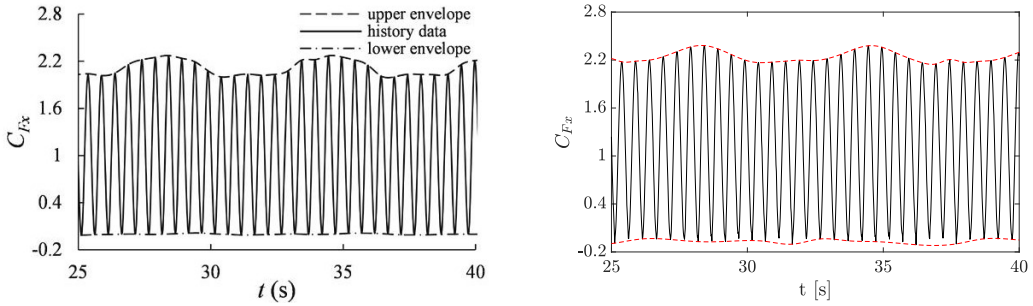

(a) Results of 2D CFD (b) Results of the U2DiVA code

Figure 4.9: Time history curves of the rotor thrust coefficient for the HEU turbine under swaying motion (λ = 2.5, U_∞ = 1m/s, ξ_{sway} = 0.2m, ω_e = 1rad/s) simulated via 2D CFD [42] (a) and U2DiVA (b).

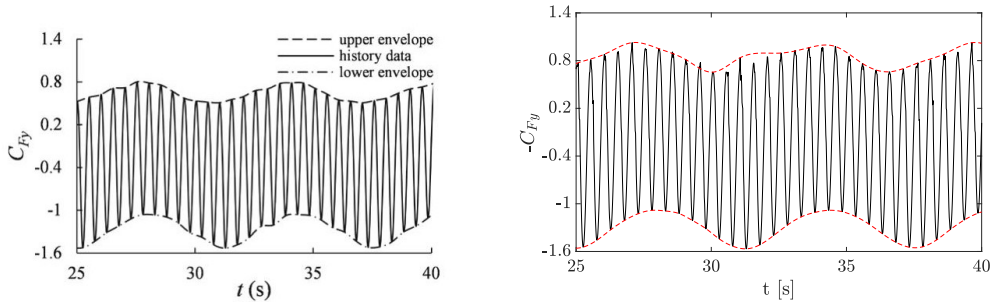

(a) Results of 2D CFD (b) Results of the U2DiVA code

Figure 4.10: Time history curves of the rotor lateral force coefficient for the HEU turbine under swaying motion (λ = 2.5, U_∞ = 1m/s, ξ_{sway} = 0.2m, ω_e = 1rad/s) simulated via 2D CFD [42] (a) and U2DiVA (b).

sway on the thrust coefficient can be considered negligible compared to the effect of surge with the same amplitude and frequency. On the other hand, the contribution of sway can be appreciated in the lateral force coefficient of Figure 4.12: compared to the oscillations in the lateral force coefficient induced by the only surge motion of Figure 4.4, the upper envelope undergoes larger oscillations and the lower envelope smaller. The introduction of sway also has an effect on the shape of the envelopes, reducing their symmetry in case of coupled surging&swaying motions compared to the only surge case. In spite of that, in the case of coupled motions, surge remains the main source of hydrodynamic load oscillations, assuming that surge and sway are described by the same amplitude and frequency.

4.4. Verification of yawing motion and surging&yawing coupled motions

Yawing motion is verified against the results presented by Wang et al.(2018) in [41]. Yaw is simulated as harmonic motion around the point P(-R,0) with the parameters of Table 4.2 and imposed to the rotation of the HEU turbine as explained in section 4.1.

Similarly to the other 2D platform's motions, yaw causes low-frequency oscillations (ω_e) of the hydrodynamic loads in both flow and cross-flow directions. Figures 4.13 and 4.14 display the oscillation of the envelopes of the hydrodynamic loads under yawing motion, which results from the periodical variation of the velocity perceived at the blades in x- and y-direction. This oscillation can be mostly appreciated in the lower envelope of the lateral force coefficient of Figure 4.14. Instead, the effect on the rotor thrust coefficient is more relevant on the upper envelope which shows on average marginally larger loads, with a negligible influence on the lower envelope, as displayed in Figure 4.13. The results of the U2DiVA code are slightly overestimated as in the cases of surge and sway motions.

In the 3 degrees of freedom simulation including rotation, surge and yaw, the time history curves of the hydrodynamic loads displayed in Figure 4.15 and Figure 4.16 are almost identical to the results of surge motion of, respectively, Figure 4.3 and Figure 4.4. The effect of yawing motion on the force coefficients is therefore weak and difficult to distinguish, and the oscillation of the envelopes is dominated by surge motion.

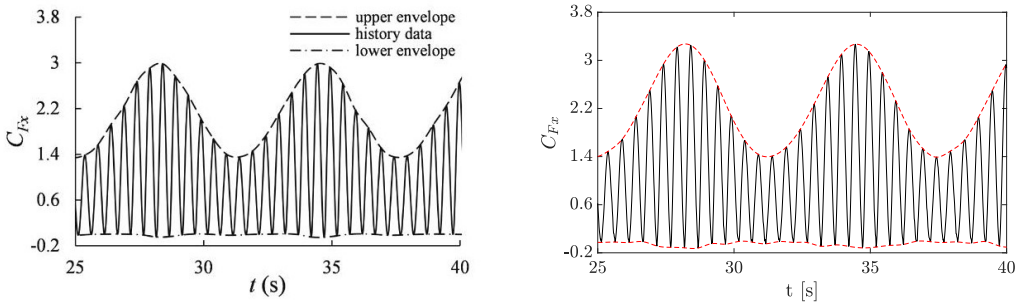

(a) Results of 2D CFD (b) Results of the U2DiVA code

Figure 4.11: Time history curves of the rotor thrust coefficient for the HEU turbine under surging&swaying coupled motions (λ = 2.5, U_∞ = 1m/s, $\xi_{surge} = \xi_{sway}$ = 0.2m, ω_e = 1rad/s) simulated via 2D CFD [42] (a) and U2DiVA (b).

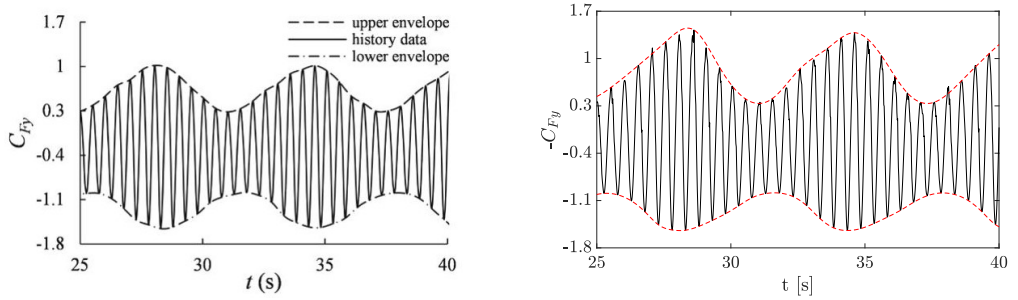

(a) Results of 2D CFD (b) Results of the U2DiVA code

Figure 4.12: Time history curves of the rotor lateral force coefficient for the HEU turbine under surging&swaying coupled motions (λ = 2.5, U_∞ = 1m/s, $\xi_{surge} = \xi_{sway}$ = 0.2m, ω_e = 1rad/s) simulated via 2D CFD [42] (a) and U2DiVA (b).

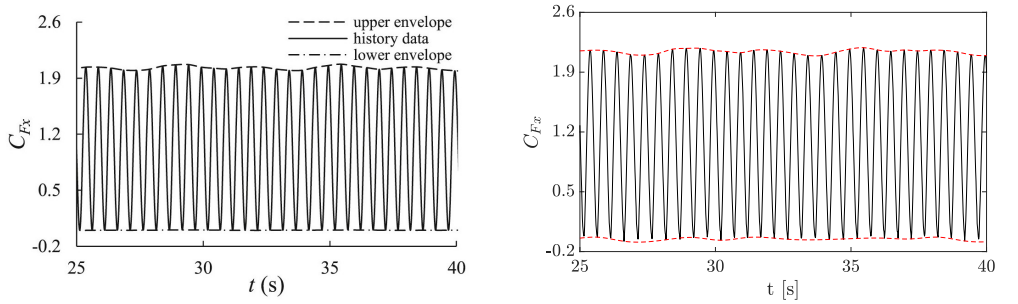

(a) Results of 2D CFD (b) Results of the U2DiVA code

Figure 4.13: Time history curves of the rotor thrust coefficient for the HEU turbine under yawing motion (λ = 2.5, U_∞ =1m/s, $\xi_{yaw} = \pi/18$, ω_e = 1rad/s) simulated via 2D CFD [41] (a) and U2DiVA (b).

4.5. Viscosity and compressibility correction

Compared to 2D CFD, U2DiVA is a simple and efficient model characterised by a relatively low computational cost. However, it assumes the flow around the blades to be inviscid, incompressible and irrotational, not accounting for friction, thermal conduction or diffusion. This leads to the overestimation of the hydrodynamic loads compared to the 2D CFD solutions as was observed in sections 4.2, 4.3 and 4.4, for either the stand-alone turbine and the turbine under imposed platform's motions. The modelling of viscous effects in the 2D CFD simulations results in reduced loads, since the gradient of the lift coefficient decreases and skin-friction and pressure drag are introduced [53]. In order to make the 2D vortex panel method more accurate, the effects of compressibility and viscosity could be included by corrections. These effects are directly related to the flow characteristics, described by the Reynolds number and the Mach number, which are respectively

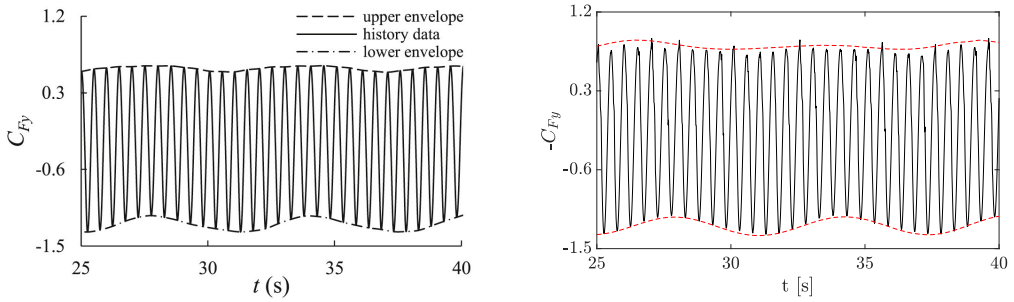

(a) Results of 2D CFD (b) Results of the U2DiVA code

Figure 4.14: Time history curves of the rotor lateral force coefficient for the HEU turbine under yawing motion (λ = 2.5, U_∞ = 1m/s, $\xi_{yaw} = \pi/18$, ω_e = 1rad/s) simulated via 2D CFD [41] (a) and U2DiVA (b).

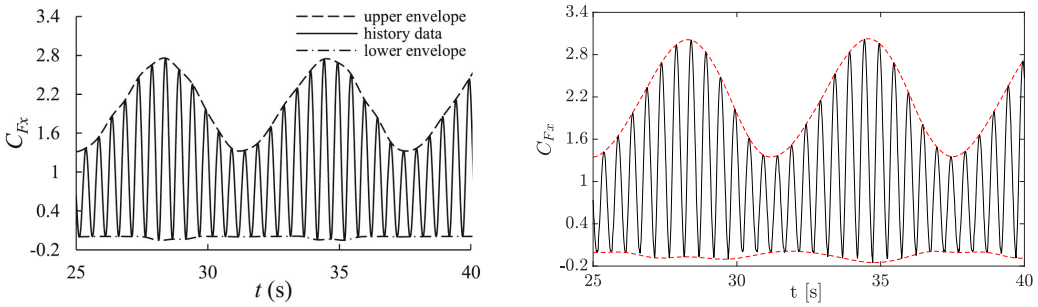

(a) Results of 2D CFD (b) Results of the U2DiVA code

Figure 4.15: Time history curves of the rotor thrust coefficient for the HEU turbine under surging&yawing coupled motions (λ = 2.5, U_∞ = 1m/s, ξ_{surge} = 0.2m, $\xi_{yaw} = \pi/18$, ω_e = 1rad/s) simulated via 2D CFD [41] (a) and U2DiVA (b).

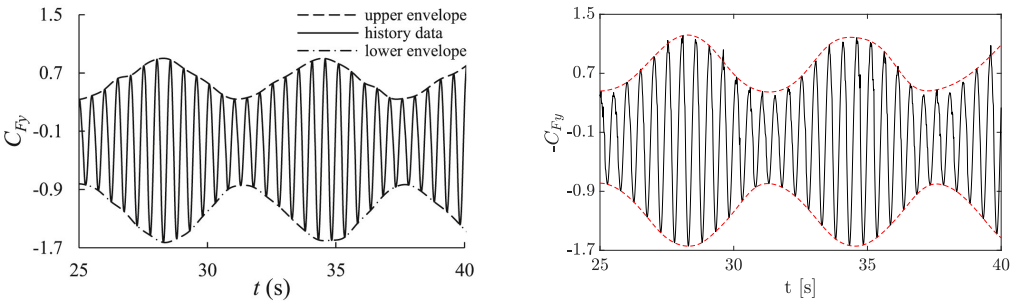

(a) Results of 2D CFD (b) Results of the U2DiVA code

Figure 4.16: Time history curves of the rotor lateral force coefficient for the HEU turbine under surging&yawing coupled motions (λ = 2.5, U_∞ = 1m/s, ξ_{surge} = 0.2m, $\xi_{yaw} = \pi/18$, ω_e = 1rad/s) simulated via 2D CFD [41] (a) and U2DiVA (b).

calculated as:

$$Reynolds = \frac{U_i \cdot c}{\nu} \tag{4.4}$$

$$Mach = \frac{U_i}{U_{water}} \tag{4.5}$$

where U_i is the local fluid velocity in [m/s], c is the airfoil chord in [m], ν is the kinematic viscosity of sea water of around $1.003 \cdot 10^{-6} m^2/s$ and C_S the speed of sound in water of around 1480m/s.

In this section, possible theoretical corrections to include compressibility and viscosity in the U2DiVA code are discussed, respectively, in 4.5.1 and in 4.5.2.

4.5.1. Compressibility correction

An approximate theoretical correction for compressibility consists in the Prandtl-Glauert rule [37] of equation 4.6, which computes the corrected pressure coefficient C_P from the pressure coefficient calculated via U2DiVA $C_{P,0}$ and the Mach number. It is valid for Mach numbers between 0 and 0.7.

$$C_P = \frac{C_{P,0}}{\sqrt{1 - Mach^2}} \tag{4.6}$$

However, the Mach numbers of the flows experienced by vertical-axis tidal turbines are very low (for example, in the simulations of this chapter Mach is in the order of 10^{-3}) since the speed of sound in water is large and the current flow is weak. Therefore, the assumption of incompressible flow (valid for $Mach < 0.3$) holds and viscous effects dominantly cause the overestimation of the results.

4.5.2. Viscosity correction

Theoretically, the potential-flow solution is valid for high Reynolds numbers and low incidence angles, for which the flow is mostly attached and the boundary layer is thin. For inviscid calculations, the lift varies linearly with the angle of attack and the drag is approximately zero. In particular, for Reynolds numbers in the order of magnitude of 10^6 the inviscid assumption holds [54]. As the angle of attack increases, the boundary layer thickens and the flow separates from the airfoil. Consequently, the flow cannot longer be approximated with the inviscid assumption, the lift drops and the drag increases because of friction. These flow phenomena are important to consider especially for vertical-axis turbines. As the angle of attack changes over one rotation, viscous effects can gain importance in some regions of the rotor, leading to flow separation and dynamic stall [21].

Since the Reynolds number in the simulations of this project is in the order of magnitude of 10^5, viscous effects are not negligible. Therefore, although the U2DiVA code already provides a good prediction of pressure and force distribution along the airfoil panels, viscosity corrections might be included to improve the accuracy of results.

Different corrections for viscous effects could be included in the U2DiVA code, such as altering the airfoil geometry by including the displacement thickness of the boundary layer or imposing a flux of momentum on the body surface [55]. Corrections are usually based on the division of the flow into two regions: an inner boundary layer region including the viscous flow adjacent to the body surface and an outer inviscid region. An example of 2D vortex panel method corrected for viscosity is the VMP2D [23], which includes a correction for the boundary layer based on Von Karman momentum equation to compute viscous forces after the simulation of the potential-flow.

4.6. Discussion

In this chapter, the U2DiVA code was verified against the 2D CFD simulations reported in the scientific literature for surge [38], sway [42] and yaw [41], simulated as either independent or coupled harmonic motions. In sections 4.2, 4.3 and 4.4, it was found that the 2D vortex panel method yields results of accuracy comparable to the 2D CFD simulations, at a reduced computational time. Therefore, it can be concluded that U2DiVA is a time-effective tool for the representation of the fluid-structure interaction between a vertical-axis tidal turbine and 2D platform's motions. Moreover, the physic description of vortex panel methods is easier to understand and interpret compared to CFD, since the potential flow theory is more fundamental and explicitly modelled. Insightful aspects of the flow phenomena can be understood by knowing the process the solution is computed with.

However, the results of U2DiVA are limited in accuracy because of the potential flow assumption. Although the hydrodynamic response of the VATT rotor to the platform's motions is correctly predicted, an overestimation of the loads is observed in the results of all the simulations presented in this chapter. The overestimation mainly interests the upper envelope of the loads. The largest overestimation observed in this chapter occurs for the lateral force coefficient, which upper envelope is overestimated by around 30% or more. Instead, the envelopes of the thrust coefficient are overestimated by less than 10%. The results of the U2DiVA code could be increased in accuracy by including viscosity and compressibility corrections. In section 4.5.1, it was found that because of the extremely low Mach numbers of tidal current flows, the assumption of incompressible flow holds for vertical-axis tidal turbines. The viscous effects inducing load reduction at the blade need to be included in the implementation of the 2D vortex panel method in order to obtain the same accuracy of CFD results, since tidal currents are characterised by low Reynolds numbers at which the

inviscid assumption does not hold. Being the loads overestimated, U2DiVA can be considered a relatively fast and conservative tool for safe floating turbines design.

Finally, the observations reported in this chapter are the starting point for the analysis that will be conducted in Chapter 5. From the results of the simulations for the verification of the U2DiVA code, it was found that the envelopes of the hydrodynamic loads fluctuate with frequency coherent with the frequency of platform's motion. The oscillations can be separated into high-frequency oscillations due to turbine rotation and low-frequency oscillations due to floating platform's motion. Furthermore, the effect of the imposed platform motion on the loading not only depends on its frequency and amplitude, but also on the direction in which the instantaneous flow field perceived at the blade is affected. In the two-dimensional plane, surging motion dominates over sway and yaw, assuming the same motion frequency, becoming the largest contribution to load oscillations in coupled dynamics simulations. Therefore, Chapter 5 studies the effects of the only surging motion on the evolution of the hydrodynamic coefficients and of the velocity triangles of two existing vertical-axis tidal turbines.

5

Analysis of the hydrodynamic response of vertical-axis tidal turbines under floating platform's surge

This chapter investigates the effect of the floating platform's surging motion on the hydrodynamic response of two existing vertical-axis tidal turbines, the Haineng 1 and the Kobold, via U2DiVA simulations. First, the set-up of the simulations is defined in section 5.1. Second, a case study involving surging motion is simulated with the Haineng 1 turbine in section 5.2, and its hydrodynamic response is studied in details by comparison with the stand-alone turbine experiencing uniform current. Following the same analysis, the hydrodynamic response of the Kobold turbine to identical surge conditions is investigated in section 5.3. Finally, the results are compared and discussed in section 5.4.

5.1. Simulation inputs and set-up

In this section, the set-up of the simulations for the analysis of the impact of surging motion on the hydrodynamics of two existing vertical-axis tidal turbines is presented. First, the range of operating conditions of the two turbines ($C_{power} - \lambda$ curves) is described in 5.1.1. Subsequently, the operational parameters can be defined, and the inputs to the reference case and to the case study including surging motion are prescribed based on the typical environmental conditions at a reference testing site and summarized, respectively, in 5.1.2 and 5.1.3. Finally, the set-up of the simulations is finalized through the findings of the sensitivity analysis of Chapter 3 and through the time step convergence study of the reference case conducted in 5.1.4.

5.1.1. The Haineng 1 and the Kobold vertical-axis tidal turbines

In this project, the analysis of the effect of surge on the hydrodynamics of vertical-axis tidal turbines is carried for two existing rotors, which were described in 3.3. The geometry of the two lift-driven straight-bladed VATTs is reported in Table 3.1.

In order to define the range of operating conditions of the turbines, the $C_{power} - \lambda$ curves are built by running simulations with U2DiVA at different tip speed ratios, keeping the remaining operating and inflow parameters constant. The current speed U_∞ is set to 1m/s. The mean power coefficient at each tip speed ratio is computed as the average of the upper envelope and lower envelope, which are extracted from the fitting of the maxima and minima of the time history curves respectively. The $C_{power} - \lambda$ curves of Figure 5.1 include both the envelopes and the average value of the instantaneous power coefficient. The latter, $\overline{C}_{power}$, indicates the ratio between the average of the instantaneous power per unit length produced by the VATT over one period cycle (in steady state conditions) and the available power per unit length in the current stream as described by equation 5.1. Notice that the instantaneous torque, and therefore the power coefficient, can become instantaneously negative at large tip speed ratios, for varying ranges of blade azimuth depending on the angles of attack experienced in the given conditions [56].

$$\overline{C}_{power} = \frac{\frac{1}{T_{rotation}} \int_t^{T_{rotation}+t} P(t)dt}{\frac{1}{2}\rho D U_\infty^3} \tag{5.1}$$

The Haineng 1's $C_{power} - \lambda$ curve of Figure 5.1(a) is obtained by varying the tip speed ratio in the range 0 to 3. Since the Haineng 1 turbine is extremely sensitive to the code inputs as discussed in 3.3, the input parameters must be tuned in order to obtain sufficiently reliable results. In particular, simulations at large tip speed ratios need to be run for a longer time in order to reach steadiness in the solution and with smaller time steps due to the increased rotational speed. The longer simulation time to reach steadiness derives from the increased vortex strength and stronger induction at large values of λ; a steady solution is reached once the wake is fully generated and developed, which depends on the geometry of the turbine, current velocity and tip speed ratio. The time inputs of the simulations at different tip speed ratios for the construction of the Haineng 1's $C_{power} - \lambda$ curve are presented in Table B.1 of the Appendix. The envelopes and the average of the instantaneous power coefficient are computed over the last 5 rotor revolutions simulated. Simulations are not run for tip speed ratios above 3, as the computational time would steadily increase because of the decreasing time step size and increasing number of rotations needed to obtain sufficiently reliable results. Therefore, the curve is assumed to approach zero at large tip speed ratios with similar trend.

The Kobold's $C_{power} - \lambda$ curve of Figure 5.1(b) is obtained by running simulations with the tip speed ratio in the range 0 to 6. Since the Kobold is less sensitive to the inputs of the U2DiVA code, a displacement of 5° per time step can be used for all the simulations. For small tip speed ratios, 20 rotations are simulated, while 35 rotations are run for tip speed ratios above 4 to allow the envelopes to reach steadiness. Also in this case, the envelopes and the average of the power coefficient are computed over the last 5 rotations of each simulation.

The average value and upper envelope of the power coefficients of the $C_{power} - \lambda$ curves constructed via U2DiVA simulations are overestimated due to the assumption of two-dimensional inviscid flow; for instance, this overestimation can be observed at optimal tip speed ratio, where the Betz limit is almost reached. In reality, the $C_{power} - \lambda$ curves would be downscaled, including the losses induced by 3D effects, viscous effects and arms/tower shadow effects. Moreover, the $C_{power} - \lambda$ curves provide information on the sensitivity of each turbine to variations in operating and/or inflow conditions. Since the average power coefficient of the Haineng 1 does not steeply change with varying λ, the power production can be considered more stable. Instead, the Kobold's response in power production to varying rotational speed and/or current speed is more unstable as can be seen from the increased steepness of the $C_{power} - \lambda$ curve. Consequently, possible control strategies of the two turbines will have different relevance, as will be investigated in section 5.2.

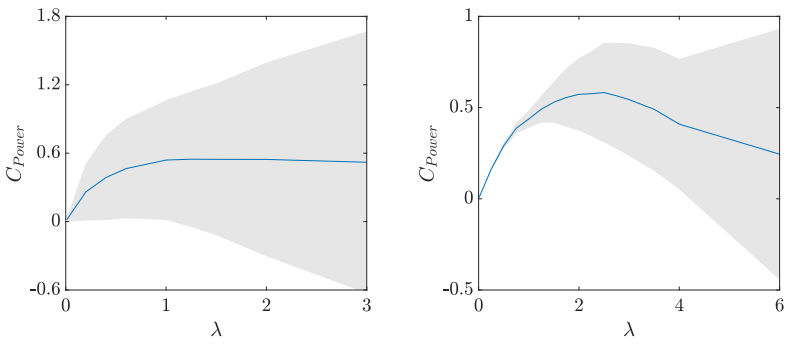

(a) Haineng 1 (b) Kobold

Figure 5.1: $C_{power} - \lambda$ curves with the average value and envelopes of the instantaneous power coefficient computed via U2DiVA of the Haineng 1 (a) and the Kobold (b) turbines for current speed U_∞ of 1m/s.

5.1.2. The only current reference case

In order to understand the effect of surging motion on the hydrodynamic coefficients, a reference case named "only current" is simulated with the inputs reported in Table 5.1. It consists of the stand-alone rotor experiencing rotation at optimal tip speed ratio under unbounded steady flow.

The inflow tidal current velocity is uniform, with no wave influence. Since both turbines were installed in the sea of Zhoushan islands (China) [19, 20], this site is used as a reference for typical environmental conditions of sites for tidal energy extraction to define the simulation inputs. From the scientific literature of the climate in Zhoushan islands, it is found that the tidal current speed typically ranges between 0m/s and 3m/s [57]. Hence, a value of 2m/s is chosen as representative of the tidal potential of the site.

The rotational speed is set to a constant value during the simulations, and it is defined from the optimal tip speed ratio λ_{opt} of each turbine and the inflow velocity U_∞ as:

$$\Omega = \frac{\lambda_{opt} U_\infty}{R} \tag{5.2}$$

Table 5.1: Inflow and operating conditions of the only current case simulated for the Haineng 1 and the Kobold turbines.

TURBINE	Only current case				
	λ_{opt}	U_∞[m/s]	A_{surge}[m/s]	ω_e[rad/s]	Φ_{surge}[°]
Haineng 1	1.5	2.0	0	0	0
Kobold	2.5	2.0	0	0	0

5.1.3. The intense surge case study

"Intense surge" refers to the surge conditions applied to all surge cases simulated in this chapter. The platform's motion is described as simple harmonic motion as in equations 3.35 and 3.36 and integrated in the U2DiVA code as described in 3.2. Its parameters are determined from the typical wave climate of the Zhoushan islands reference site. The inflow and operating conditions are reported in Table 5.2.

The ranges of wave height and wave period of Zhoushan islands can be extracted from the scatter table summarizing 10 years of wave climate of [58] and their average values can be found in [59]. The amplitude of surge A_{surge} is set to be half the inflow current speed, which resulting surge displacement falls within the range of annual average wave height provided in the literature of the site conditions (0.7-1.6m). The platform's surging frequency ω_e equals the wave frequency and it is computed from the average wave period at the reference site, set to the annual average value of 5s. The values of the "intense surge" parameters are arbitrarily chosen for a clearer visualization of the effect of surge on the simulation quantities as it is expected to severely impact on the envelopes of the coefficients.

Table 5.2: Inflow and operating conditions of the intense surge case study simulated for the Haineng 1 and the Kobold turbines.

TURBINE	Intense surge case				
	λ_{opt}	U_∞[m/s]	A_{surge}[m/s]	ω_e[rad/s]	Φ_{surge}[°]
Haineng 1	1.5	2.0	1.0	$\frac{2\pi}{5}$	0
Kobold	2.5	2.0	1.0	$\frac{2\pi}{5}$	0

5.1.4. Time step convergence study

Once the inflow conditions and the operating point of the turbines are defined, a convergence study is carried in order to finalize the inputs to the U2DiVA simulations. Using the lessons learnt in the sensitivity analysis of 3.3, a panelling consisting of 190 panels is adopted for each airfoil, since it was concluded that the computational time is not strongly affected by the density of the grid. The panelling is closed at the trailing edge in order to satisfy the Kutta condition. About the simulation time inputs, the time step size was prescribed in the range 1° to 5° as compromise between accuracy and computational cost. The convergence study presented in this section has the purpose of identifying the number of rotor revolutions after which the solution can be considered steady and selecting a time step size within the prescribed range.

First, the number of rotations after which steadiness is reached needs to be defined. The results become steady once the wake is fully developed, which depends on the geometry of the turbine and on the operating and inflow conditions inputted in the simulation. In this project, it is defined by running simulations of the two turbines under the only current reference case for a large number of rotations with 15° displacement per time step. Since the envelopes of the power coefficient become straight after 60 rotations (see Figures B.1 and B.2 in the Appendix), the results of the reference case and intense surge case will be observed in the time interval between the 60^{th} and 80^{th} rotation.

Second, simulations at decreasing time step sizes are run in order to observe the convergence in terms of MSE of the hydrodynamic load coefficients on one airfoil after 60 rotations, as shown in Figures 5.2 and 5.3. The Haineng 1 turbine is characterised by steeper convergence compared to the Kobold, which was found to be less sensitive to the simulation inputs in 3.3. Eventually, a displacement of 3° per time step is chosen as a trade-off between accuracy and computational time for both turbines.

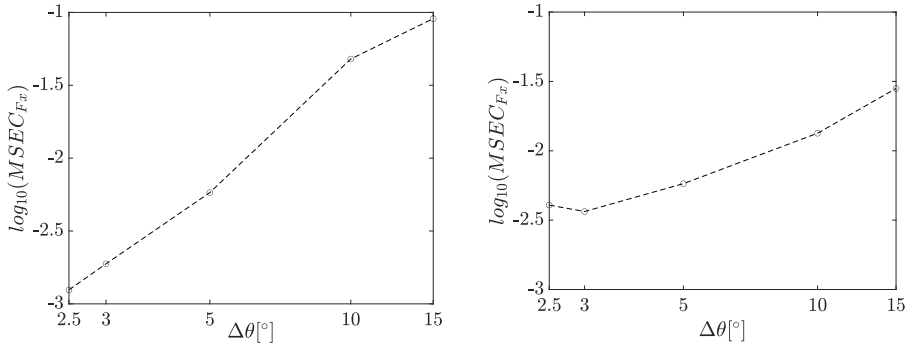

(a) Haineng 1 (b) Kobold

Figure 5.2: Convergence of the MSE of the thrust coefficient for decreasing time step size with respect to a displacement of 1°per time step at one blade of: (a) the Haineng 1 turbine ($U_\infty = 2$m/s,$\lambda = 1.5$) and (b) the Kobold turbine ($U_\infty = 2$m/s,$\lambda = 2.5$).

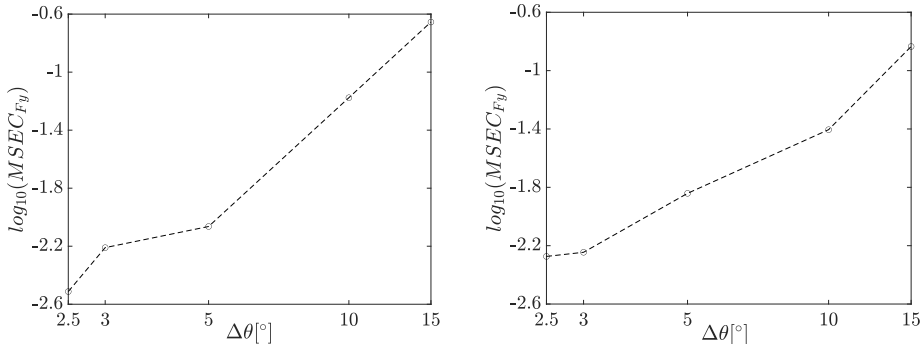

(a) Haineng 1 (b) Kobold

Figure 5.3: Convergence of the MSE of the lateral force coefficient for decreasing time step size with respect to a displacement of 1°per time step at one blade of: (a) the Haineng 1 turbine ($U_\infty = 2$m/s,$\lambda = 1.5$) and (b) the Kobold turbine ($U_\infty = 2$m/s,$\lambda = 2.5$).

5.2. Case study: Haineng 1 turbine under intense surge

The scientific literature about vertical-axis tidal turbines under platform's surge motion mostly studies the effect of different operating parameters and surge conditions on the hydrodynamic coefficients, but fails at providing a detailed description of the load fluctuations due to surge and insights on their origin. In this section, the hydrodynamic response of the Haineng 1 rotor under intense surging motion is investigated by comparison with the reference only current case. The investigation focuses on the time evolution of the rotor hydrodynamic coefficients and of the flow perceived at one blade. The study of one blade is sufficient to understand the effect of surge on the rotor, as all the blades experience the same flow field with a certain time shift depending on the phase difference between airfoils and between each airfoil and the surge harmonic motion.

The analysis is structured as follows. First, the effect of the platform's intense surge on the hydrodynamic load and power coefficients is described and quantified in 5.2.1, starting from the considerations of Chapter 4. Second, the power spectral density of the relative velocity at one blade is analysed to define the fundamental frequencies of oscillation of the simulation quantities in 5.2.2. Third, the study of the time evolution of the velocity triangles at quarter chord of one blade is conducted in 5.2.3. Eventually, some examples of the effect of tuning the rotor operating parameters on the hydrodynamic response to given surge conditions are provided in 5.2.4.

5.2.1. Effect of surge on the hydrodynamic coefficients

The available scientific literature reports that the platform's motions introduce unsteadiness in the flow perceived at the rotor blades resulting in multiple frequencies of oscillation of the loads, as discussed in Chapter 4. This can be observed in the comparison of the time history curves of the rotor thrust, lateral force and power coefficients of the only current reference case and intense surge case study displayed, respectively, in

Figures 5.4, 5.5 and 5.6.

Since the flow field perceived at the blade of a vertical-axis tidal turbine varies along the revolution, the simulation quantities oscillate periodically in time between an upper envelope and a lower envelope, i.e. the curves connecting respectively the maximum and minimum values perceived at the blades over each rotation. In the case of stand-alone Haineng 1 turbine under constant tidal current inflow, the total thrust and lateral force coefficients and the power coefficient oscillate periodically with frequency $B\Omega$, where B is the number of blades. Because of the steady inflow conditions and constant operational parameters, the envelopes of the time history curves of the hydrodynamic coefficients, as well as the envelopes of any quantity computed in this simulation, are straight lines. When imposing intense surge, the oscillations of the load and power coefficients are related to either the rotational frequency $B\Omega$ and the surge frequency ω_e, and the amplitude of oscillation depends on the operating conditions and the surge conditions. Differently from the results of the simulations presented in Chapter 4, high-frequency and low-frequency oscillations cannot be distinguished because of the frequency of surge being close to the frequency of rotation. This results in severe and frequent oscillations of the hydrodynamic coefficients, since the inflow conditions dynamically change within one rotation period. An additional recognizable effect of surge is the introduction of spikiness and irregularities in the time history curves compared to the only current case.

The instantaneous amplitude and direction of surge has a direct impact on the time evolution of load coefficients in both horizontal and vertical direction. When the surge velocity adds to the tidal current speed, both loads increase in magnitude; for surge velocity opposite to the tidal current, the loads decrease towards zero; finally, when the surge velocity is instantaneously zero, the loads nearly overlap with the results from the only current case. Therefore, the instantaneous velocity of surge dominantly influences the actual transient value of the tip speed ratio, resulting in load and power oscillations. Consequently, the envelopes of the loads and power coefficients drastically deviate from the only current reference case, especially in the positive direction.

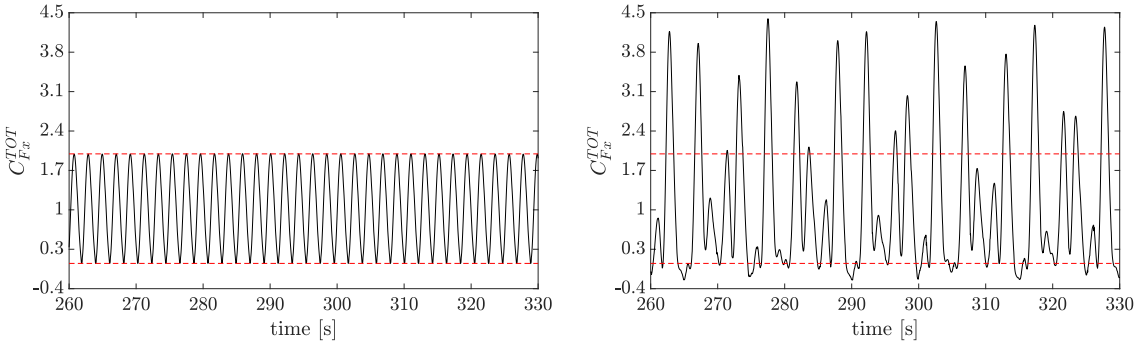

(a) Only current

(b) Intense surge

Figure 5.4: Comparison of the time history of the Haineng 1 rotor thrust coefficient for: (a) the only current case (U_∞ = 2m/s,λ = 1.5) and (b) the intense surge case (U_∞ = 2m/s,λ = 1.5,A_{surge} = 1m/s,$\omega_e = \frac{2\pi}{5}$ rad/s).

In order to determine whether intense surge could be beneficial to the Haineng 1 turbine in terms of loading and performance, the average and extreme values of the instantaneous thrust, lateral force and power coefficients of the only current case and the intense surge case are compared in Figure 5.7 and quantified in Table 5.3. These values are computed over a limited interval of time, consisting of an entire number of rotations and surge cycles. As previously observed, the amplitude of oscillation of the coefficients is significantly widened when the platform is on motion. The widening of the force coefficients envelopes has a negative impact on the cyclic loading of the rotor, leading to increased maximum load and marked fatigue issues. Since the surging motion is harmonic, with surge velocity periodically oscillating from 1m/s to -1m/s, the average thrust coefficient and lateral force coefficient are only marginally affected, with an increase of 5% and 3%, respectively, due to non-linear effect of surge. Instead, the average power coefficient increases from 0.57 to 0.86, meaning that additional power can be extracted from the platform's motion[1].

However, the analysis of the load and power amplitude is limited by the assumptions of the U2DiVA code.

[1] Notice that in the only current case the power coefficient is close to the Betz limit because of the assumption of 2D inviscid flow. Under surge motion, the power coefficient calculated with respect to the free-stream velocity is larger than the Betz limit due to the unsteady inflow current affecting the instantaneous tip speed ratio.

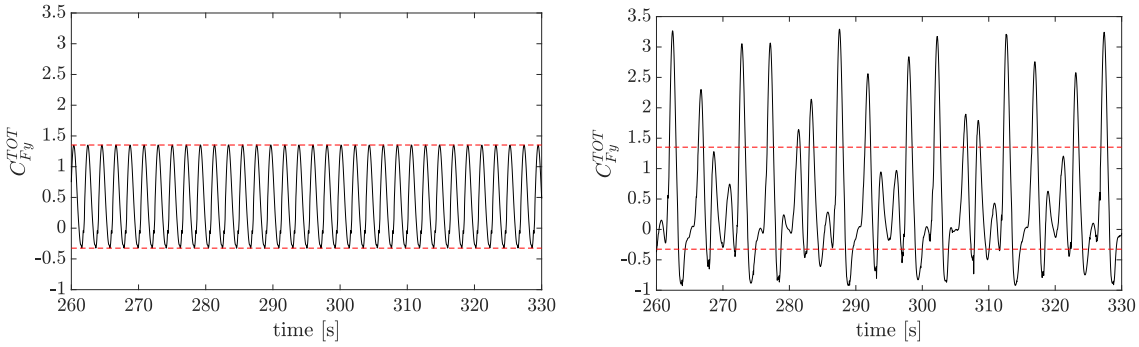

(a) Only current (b) Intense surge

Figure 5.5: Comparison of the time history of the Haineng 1 rotor lateral force coefficient for: (a) the only current case (U_∞ = 2m/s,λ = 1.5) and (b) the intense surge case (U_∞ = 2m/s,λ = 1.5,A_{surge} = 1m/s,$\omega_e = \frac{2\pi}{5}$rad/s).

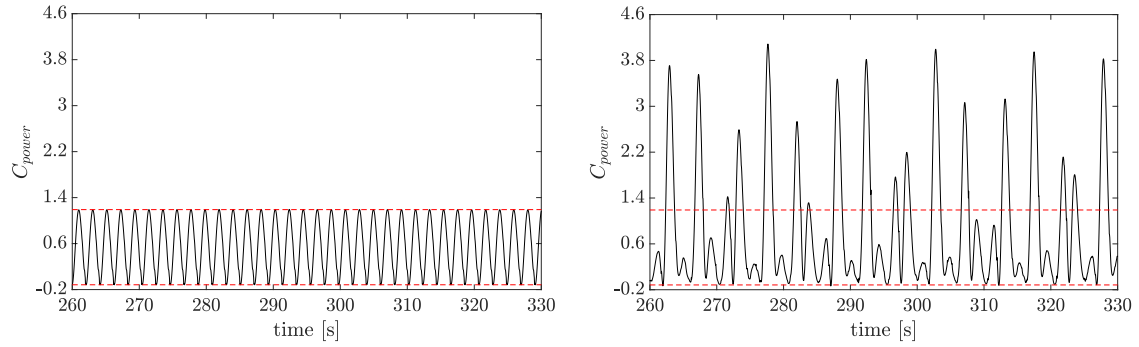

(a) Only current (b) Intense surge

Figure 5.6: Comparison of the time history of the Haineng 1 rotor power coefficient for: (a) the only current case (U_∞ = 2m/s,λ = 1.5) and (b) the intense surge case (U_∞ = 2m/s,λ = 1.5,A_{surge} = 1m/s,$\omega_e = \frac{2\pi}{5}$rad/s).

Because of the large angles of attack experienced at the blades in both the only current case and the intense surge case (see Figure 5.15), the values obtained from the U2DiVA simulations are to be considered overestimated. Moreover, as surge velocity widens the range of angles of attack, the overestimation is stronger in the results of the intense surge case study, particularly for the upper envelopes and the average values of the hydrodynamic coefficients.

Table 5.3: Comparison of the minimum (min), maximum (max) and average (ave) values of the hydrodynamic coefficients of the Haineng 1 turbine in the only current reference case (U_∞ = 2m/s,λ = 1.5) and in the intense surge case study (U_∞ = 2m/s,λ = 1.5,A_{surge} = 1m/s,$\omega_e = \frac{2\pi}{5}$rad/s). The relative percent change due to surge is indicated.

	C_{Fx}^{TOT}			C_{Fy}^{TOT}			C_{power}^{TOT}		
	min	max	ave	min	max	ave	min	max	ave
Only current	0.05	2.00	1.06	-0.33	1.36	0.46	-0.12	1.20	0.57
Intense surge	-0.25 (-621%)	4.40 (120%)	1.11 (5%)	-0.93 (183%)	3.29 (143%)	0.47 (3%)	-0.13 (15%)	4.09 (242%)	0.86 (53%)

5.2.2. Identification of the fundamental frequencies of oscillation

In order to identify the main frequencies of oscillation in the results of the only current case and the intense surge case, the power spectral density (PSD) of the relative velocity at quarter chord of airfoil 1 is obtained through the fast Fourier transform (FFT). The spectral content of the relative velocity is analysed as it includes the frequencies of all the components of the flow, both in x- and y-direction, representing the oscillations in the time evolution of both the velocity triangles and the hydrodynamic coefficients.

In the only current case, the fundamental frequency of rotation Ω and its multiples can be identified in

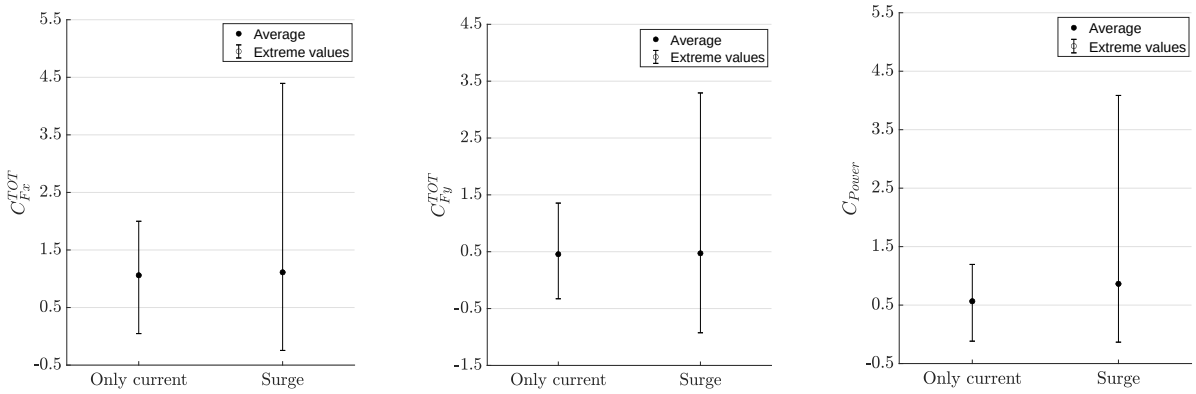

Figure 5.7: Comparison of the average and extreme values of the thrust, lateral force and power coefficients of the Haineng 1 turbine for the only current reference case ($U_\infty = 2$m/s,$\lambda = 1.5$) and intense surging motion ($U_\infty = 2$m/s,$\lambda = 1.5, A_{surge} = 1$m/s,$\omega_e = \frac{2\pi}{5}$rad/s).

Figure 5.8(a). Additional frequencies with limited variation can be observed in between of the multiples of Ω, resulting either from the periodic vortex shedding at the blade or from frequency spectrum leakage. The periodic vortex shedding at the blade is directly related to the velocity induced by the airfoils' panels and wake elements on the quarter chord point of the airfoil in analysis. This can be confirmed by comparing the PSD of the relative velocity to the PSD of the relative velocity without induction (see Figure B.3 in the Appendix); the latter only includes the large peaks at Ω and its multiples and few small peaks due to spectrum leakage. The power density of the peaks related to the induced velocity is small compared to the peaks at multiples of Ω because of the limited amplitude of these oscillations compared to the other components of the perceived velocity at the blade.

In the case of the Haineng 1 under intense surge motion, multiple fundamental frequencies and intense power density variations at high-frequencies are introduced in the PSD graph of the relative velocity at one blade as shown in Figure 5.8(b). Besides the peak at rotational frequency Ω, the first recognizable peak occurs at $0.0398Hz$, corresponding to the frequency at which the relative velocity repeats almost identically at the blade, and the second peak at the surge frequency ω_e of $0.2Hz$, as can be seen in Figure 5.9. The frequency of the first peak derives from both Ω and ω_e and can be easily computed manually, with the following considerations. In the only current case, the turbine simply rotates under uniform incoming tidal current and the time variation of the flow field depends exclusively on the airfoil position on the rotor circumference, so the flow field at each blade repeats every 360°, with frequency Ω. Instead, in the intense surge case the flow field repetition period equally depends on the airfoil position on the rotor circumference and the rotor position due to surge. The period of repetition is longer than the rotation period, in this case around $25.1s$ which corresponds to 6 turbine rotations and 5 surge cycles. This value is found manually by knowing that in 5 seconds of surge $\frac{T_{surge}}{T_{rotation}} \simeq 1.2$ surge cycles per rotation occur and that an entire number of surge cycles that multiplied by 1.2 gives an entire number of rotations must be defined. [2]

Compared to the only current case, the spectral power density graph of the surge case presents more frequent oscillations with larger power density variations due to the multiples of the three fundamental frequencies and to the more complex blade-vortex interactions. In fact, the time evolution of the wake and the airfoil's interaction with the wake and with other airfoils is strongly affected by surge, introducing new frequencies and increasing the strength of the relative velocity oscillations. An extensive explanation of the time evolution of the induced velocity generating these large high-frequency oscillations is elaborated in section 5.2.3.

5.2.3. Time evolution of the velocity triangles

Since U2DiVA is an unsteady code solving the pressure distribution from the flow field over the body at each time step, a detailed analysis of the time evolution of the velocity triangles provides insights about the influence of surge on the flow variation at the blade, and consequently on the oscillations of rotor loads and power.

Figure 5.10 represents the oscillations introduced by the platform's motion in the relative velocity at quar-

[2]Since the period of rotation is a periodic number (4.1888s), the flow field does not exactly repeat after a full number of rotations and surge cycles. The minimum difference between the original and new position is reached, but there is no exact coincidence.

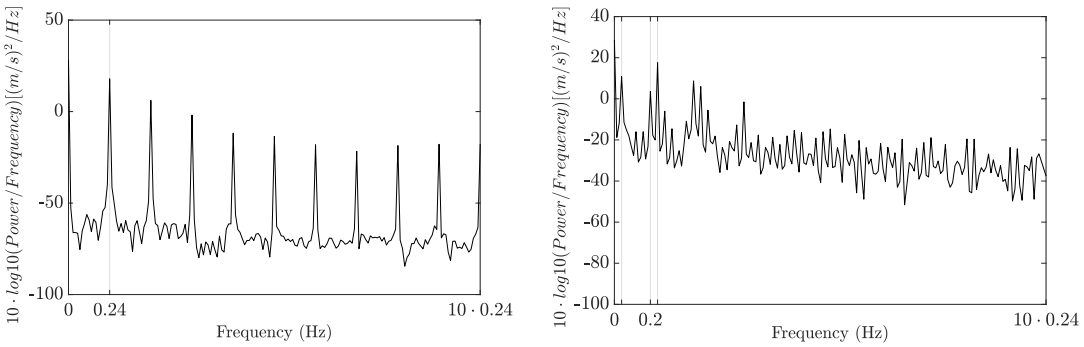

(a) Only current (b) Intense surge

Figure 5.8: Comparison of the spectral power density of the relative velocity at quarter chord of one blade of the Haineng 1 turbine for: (a) the only current case (U_∞ = 2m/s,λ = 1.5) and (b) the intense surge case (U_∞ = 2m/s,λ = 1.5,A_{surge} = 1m/s,$\omega_e = \frac{2\pi}{5}$rad/s).

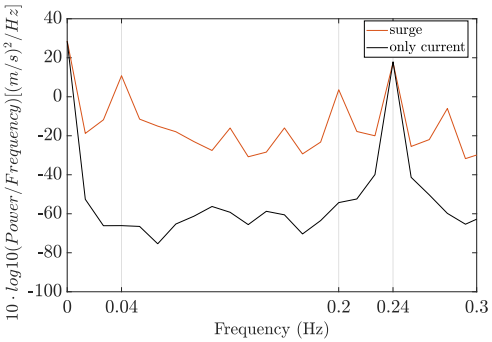

Figure 5.9: Visualization of the fundamental frequencies of the spectral power density of the relative velocity at quarter chord of one blade of the Haineng 1 turbine for the only current case (U_∞ = 2m/s,λ = 1.5) and the intense surge case (U_∞ = 2m/s,λ = 1.5,A_{surge} = 1m/s,$\omega_e = \frac{2\pi}{5}$rad/s).

ter chord of one blade by comparison with the periodic and smooth behaviour of the only current case because of the modified evolution of the velocity triangles at the blades. The maxima and minima of the relative velocity in the intense surge case oscillate around the straight envelopes of the only current case (red dotted lines) depending on the instantaneous magnitude and direction of the surge velocity. Therefore, the inflow velocity component U_{surge} exerts the most dominant effect on the oscillating envelopes of the relative velocity, by modifying its time evolution in both magnitude (Figure 5.10) and direction (Figure 5.15), as well as on the envelopes of the hydrodynamic coefficients observed in section 5.2.1. The high-frequency oscillations described in the frequency analysis of section 5.2.2 are visible from the irregular profile of the relative velocity of one blade. They derive from the effect of the surging motion on the time history of the induced velocity, affected either in magnitude and direction, and results in a more irregular response of the hydrodynamic coefficients.

The relative velocity at quarter chord of one blade is decomposed into the horizontal and vertical directions following equation 3.14 in order to isolate the effect of surge in terms of the surge inflow velocity U_{surge} and the surge displacement X_{surge}. Figure 5.11 compares the horizontal and vertical relative velocity components including and excluding the induced velocity. When the induction is not included in the computation, the relative velocity is a smooth harmonic signal (black curves), given as the sum of constant and sinusoidal terms ($U_{disp,x} + U_\infty$ in x-direction and $U_{disp,y}$ in y-direction). The envelopes of the signal in x-direction oscillate with the fundamental period of 25.1s and amplitude of A_{surge}, while the envelopes in y-direction are straight since surge velocity only acts in x-direction. Once the induction term is included, the evolution of the relative velocity presents high-frequency peaks deriving from the unsteady and complex interaction of the blade with the singularity elements of the computational domain. In particular, the time history of the horizontal relative velocity is shifted downwards by the induced velocity, as it is always negative in this direction ($U_{induced,x} < 0$), while in the cross-flow direction the induced velocity oscillates between positive and negative values introducing oscillations in both directions.

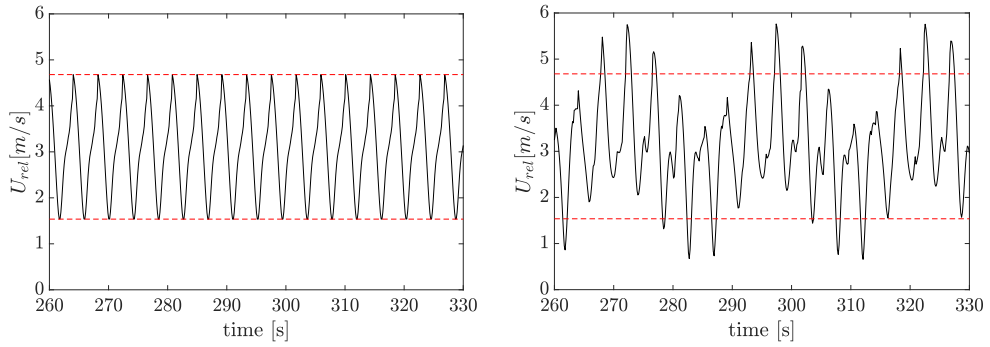

(a) Only current (b) Intense surge

Figure 5.10: Comparison of the time history of the relative velocity at quarter chord of one blade of the Haineng 1 turbine for: (a) the only current case (U_∞ = 2m/s,λ = 1.5) and (b) the intense surge case (U_∞ = 2m/s,λ = 1.5,A_{surge} = 1m/s,$\omega_e = \frac{2\pi}{5}$ rad/s).

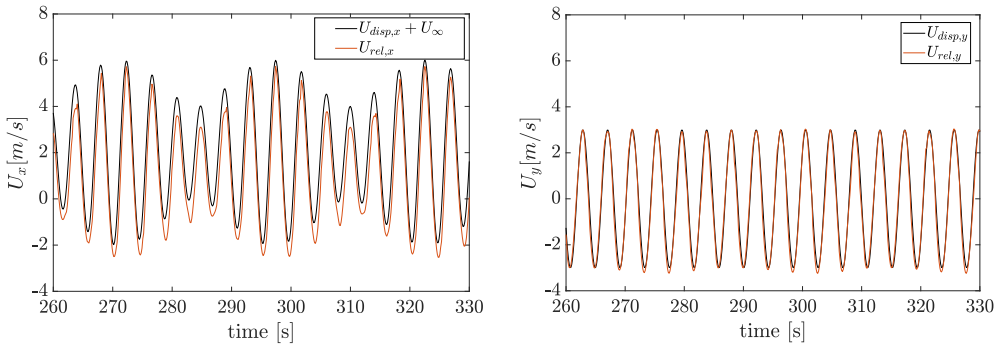

(a) Horizontal relative velocity (b) Vertical relative velocity

Figure 5.11: Comparison of the relative velocity at one blade of the Haineng 1 turbine in the intense surge case (U_∞ = 2m/s,λ = 1.5,A_{surge} = 1m/s,$\omega_e = \frac{2\pi}{5}$ rad/s) in x-direction (a) and y-direction (b), with the induction (orange curve) and without the induction (black curve).

In the U2DiVA code, the induction results from the sum of two terms, as described by equation 3.12: the velocity induced by the wake elements U_{wake} and the velocity induced by the doublets/sources distribution over the airfoils $U_{otherairfoils}$ on the point in analysis. Both induced velocity terms are directly proportional to the strength of the respective singularity elements and inversely proportional to the distance between the singularity element and the point where the induction is computed. The platform's surging motion affects the strength of the panels and wake vortex points in time, due to the unsteady flow field, and it dynamically translates the rotor position with respect to the wake. As a result of the modified wake-airfoil and wake-wake interactions (free-wake model), a different wake evolution profile can be seen in the far-wake and in the near-wake, respectively illustrated in Figure 5.13 and in Figure 5.12. In the only current case, the wake evolution is steady, and the interaction with the wake elements is stronger for airfoils in downwind position since the tidal current constantly drags away the wake elements from the rotor in the positive x-direction. Under surging motion, spindle-shaped wake zones are formed downwind every surge period, originating intricate wake profiles in the far-wake region [60]. The evolution of the near-wake is strongly influenced by the instantaneous surge velocity and displacement and it dominantly determines the magnitude and profile of the wake induced velocity. Figure 5.12 shows how the number of wake elements surrounding each airfoil and the distance between singularity elements changes depending on the instantaneous value of the surge displacement. For positive surge displacement as in Figure 5.12(b), the rotor moves towards the wake, reducing the distance with the wake elements thus resulting in stronger airfoil-wake interactions. In the surge equilibrium position of Figure 5.12(c), the distribution of the vortex points in the near-wake resembles more the one of the only current case of Figure 5.12(a). Finally, when the surge displacement is negative, the airfoils move away from the wake, causing a reduction in the magnitude of the wake induced velocity because of the increased distance wake-rotor.

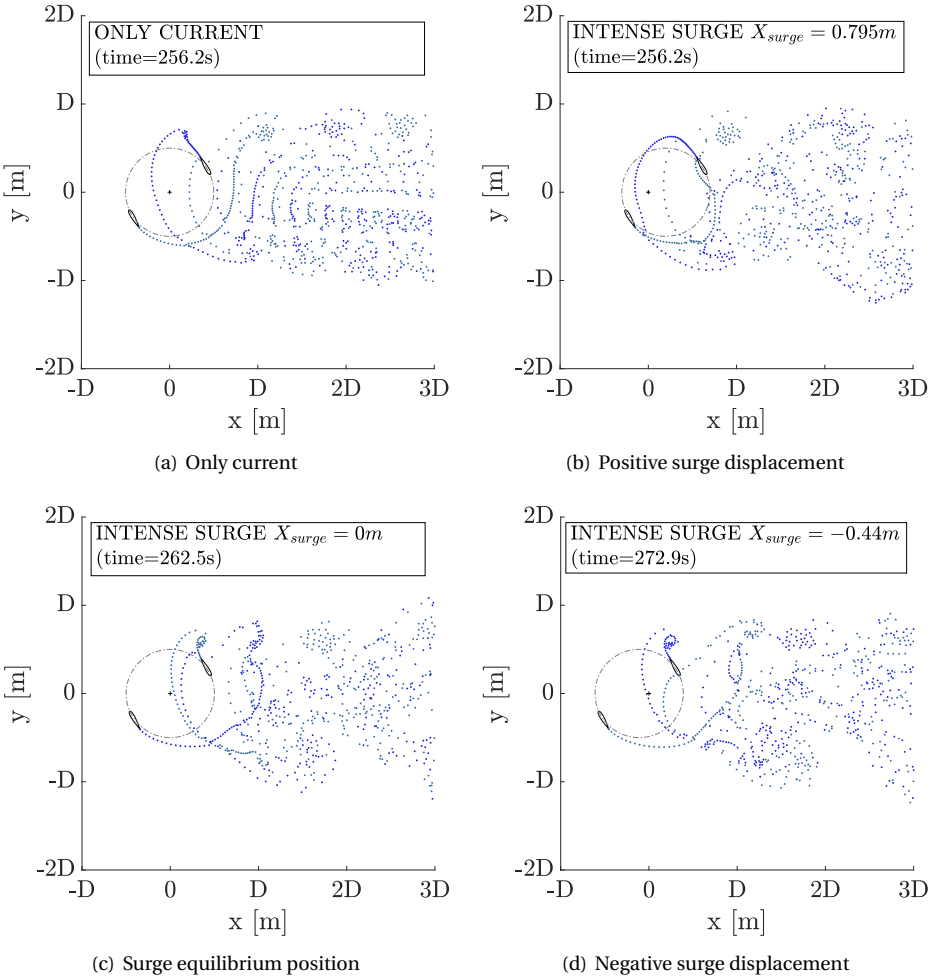

(a) Only current

(b) Positive surge displacement

(c) Surge equilibrium position

(d) Negative surge displacement

Figure 5.12: Evolution of the near-wake for the only current reference case (a) and for the intense surge case study in different time instants, corresponding to positive surge displacement (b), equilibrium position (c) and negative surge displacement (d).

The modified wake profile of Figure 5.13(b) derives from three effects introduced by the surging motion on the development of the wake in time. First, the strength of the doublets/sources distribution on the airfoils and, consequently, of the wake vortices shed at the trailing edge are affected by the unsteadiness of surge. In the first rotations of the U2DiVA simulation, the surge velocity mostly modifies the instantaneous velocity triangles at the control points; once the wake is fully developed, the surge displacement also impacts the velocity triangles evolution. Second, the rotor displacement in time due to surge motion results in the vortex shedding at the trailing edge occurring in different positions in time, outside of the original rotor circumference. Third, the distance between the wake vortex points and the point where the induction is computed changes in time with the instantaneous value of X_{surge}.

Each of the induced velocity components is affected differently by surge, depending on the singularity elements interested and the direction. The velocity induced by the wake in x-direction is the only component of the induced velocity directly dependent on the instantaneous rotor position in time due to the surge displacement X_{surge}. In the only current case, this component is weak when the airfoil is upwind, being this the furthest from the wake elements, and strong in downwind position, because of the reduced distance airfoil-wake. The surge displacement imposed to the rotor induces oscillations in the envelopes of this velocity component in time since the distance between the airfoils and the wake elements is continuously changing. Positive surge displacement leads to stronger blade-vortex interactions and a shift of the values downwards (to more intense negative values), while negative surge displacements cause a reduction in the magnitude of the induced velocity. The wake velocity in y-direction and the velocity induced by the airfoils are smaller in magnitude compared to $U_{wake,x}$. The oscillations of these three induced velocity components mostly originate from the variation of strength of the singularity elements. They do not directly depend on

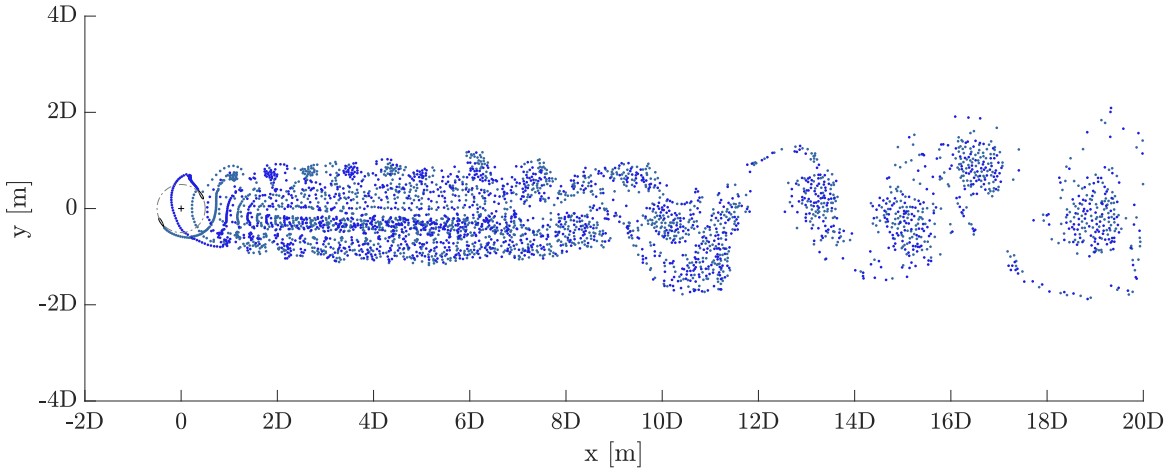

(a) Only current

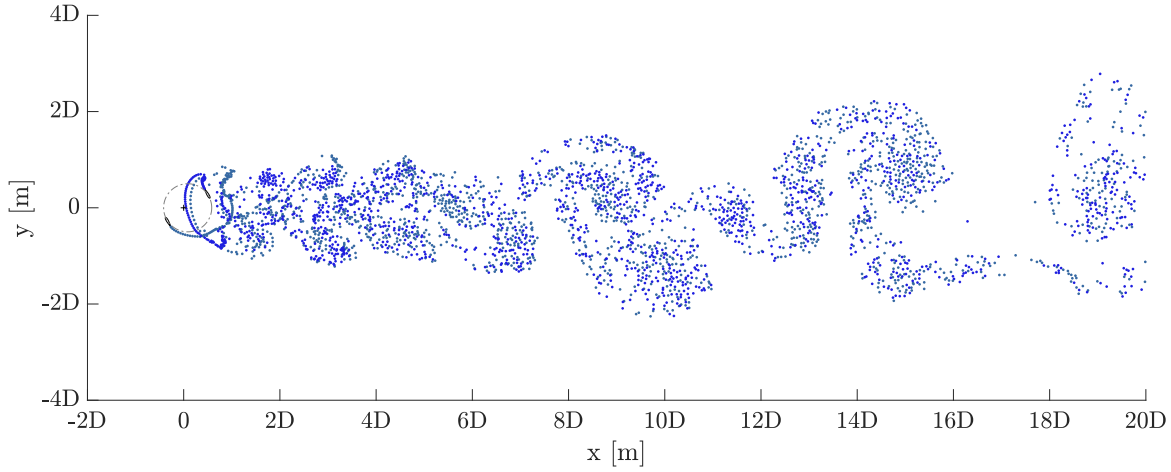

(b) Intense surge

Figure 5.13: Evolution of the far-wake up to 20 rotor diameters downwind the Haineng 1 rotor in the only current reference case (a) and in the intense surge case study (b) at simulation time of 230.6s (61^{st} rotation). The wake elements shed by different airfoils are coloured differently for clearer visualization.

the rotor displacement in time, as they are calculated from the fixed distances either of the wake elements in y-direction or between the airfoils. All these components oscillate between positive and negative values and their envelopes undergo periodic oscillations with period 25.1s, as illustrated in the Appendix (Figures B.4, B.5, B.6, B.7).

Since the time evolution of the velocity components is characterised by amplitude oscillations and irregular shape when the rotor experiences intense surge, the same will occur for the angle between the relative velocity and the airfoil chord, i.e. the angle of attack α. The amplitude of oscillation of the angle of attack has direct implications on the reliability of the results of the simulations. The assumption of potential flow at the base of the U2DiVA code is only valid for small angles of attack. However, the blades in both cases simulated experience a large range of angles of attack over the rotation, as illustrated in Figure 5.15, which implies non-negligible viscous effects. As a result, the overestimation of the force coefficients, increasing for larger angles of attack, is to be expected. Corrections accounting for viscous effects or the coupling of the code with viscous models, as discussed in 4.5, become particularly relevant in the intense surge case, which range of angles of attack is almost double the range of the reference only current case. At such angles of attack, flow separation and dynamic stall are also more likely to occur, of which U2DiVA limits the investigation.

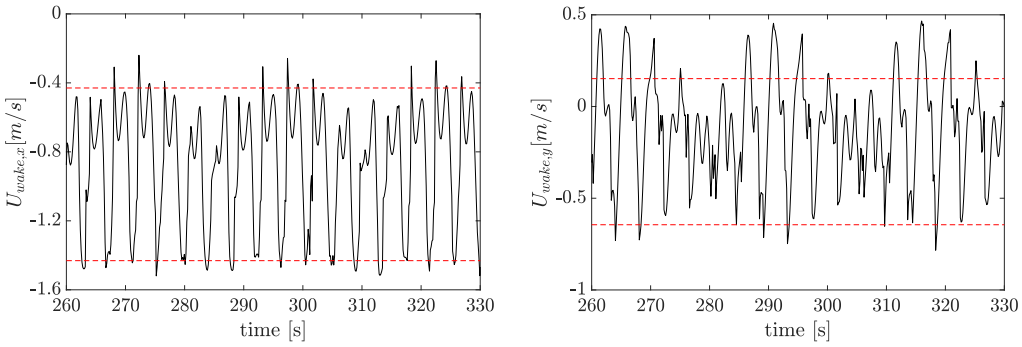

(a) Horizontal wake induced velocity (b) Vertical wake induced velocity

Figure 5.14: History curves of the wake induced velocity at quarter chord of one blade of the Haineng 1 turbine in the intense surge case (U_∞ = 2m/s,λ = 1.5,A_{surge} = 1m/s,$\omega_e = \frac{2\pi}{5}$ rad/s) in x-direction (a) and y-direction (b). The red dashed lines are the upper and lower envelopes of the only current reference case.

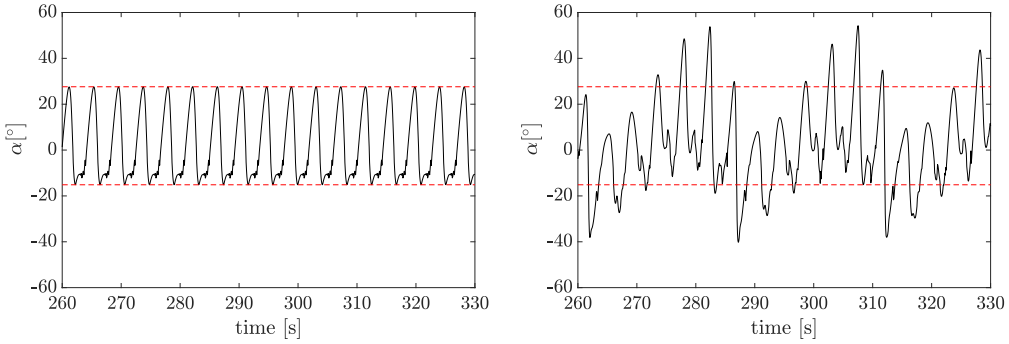

(a) Only current (b) Intense surge

Figure 5.15: Comparison of the time history of the angle of attack of one blade of the Haineng 1 turbine for: (a) the only current case (U_∞ = 2m/s,λ = 1.5) and (b) the intense surge case (U_∞ = 2m/s,λ = 1.5,A_{surge} = 1m/s,$\omega_e = \frac{2\pi}{5}$ rad/s).

5.2.4. Possible tuning of the rotor parameters for controlling the hydrodynamic response to surge

The operational parameters of the Haineng 1 tidal turbine could be optimally tuned through control strategies in order to modify its hydrodynamic response to surging motion, with the aim of either reducing the amplitude of load oscillations or exploiting surge for enhanced power extraction. No control strategy is presented in this project. Instead, the tuning the rotor operational parameters is analysed through two examples, which implement respectively phase tuning for optimal power extraction and rotational speed tuning for the reduction of load oscillations. The inputs of these simulations are reported in Tables B.2 and B.3 of the Appendix.

First, the tuning of the phasing between surge cycle and initial airfoil position is investigated in the following example. In order to define the phase difference, the tip speed ratio is altered to a sub-optimal value so that the ratio between surge period and rotation period is a finite number, since the original indefinite ratio $\frac{T_{surge}}{T_{rotation}}$ would lead to continuously changing phase at every rotation. Hence, the rotation period is reduced to 4 seconds resulting in a tip speed ratio of $\lambda_{new} = \frac{2\pi}{4} \simeq 1.57$. This implies a marginal loss in power coefficient of the stand-alone turbine, decreasing from 0.56 to 0.55, but also allows a better exploitation of the intense surging conditions, with power coefficient increased from 0.86 to 0.91. The objective of phase tuning would be maximising the effect of positive surge velocity, which increases force and power coefficients, while minimising the effect of negative surge velocity, which reduces them. With the given rotational speed, each surge cycle lasts one full rotation and one fourth, meaning that when defining a certain phase ϕ_{surge} the next rotations will experience a phasing of ϕ_{surge}, $\phi_{surge}+90^\circ$, $\phi_{surge}+180^\circ$ or $\phi_{surge}+270^\circ$. The hydrodynamic coefficients obtained for surge phases of $0^\circ, 30^\circ, 45^\circ$ and 60° are compared in Figure 5.16 and quantified in Table 5.4. The details of the simulations inputs can be found in Table B.2 of the Appendix. The effect of phas-

ing on the average of the coefficients is limited, with relative percent change of less than 4% with respect to a phasing of 0°. The extreme values are more affected, with relative percent change of the maxima and minima of less than 23% with respect to a phasing of 0°, and depends on the phase difference between the maximum surge velocity and airfoil positions corresponding to the extreme values of the force coefficients. For example, the largest upper envelope of the thrust force is reached for the surge phase of 45° at which the maximum positive surge is reached for the airfoil positions of maximum thrust (90° and 270°).

From the phasing example, it can be concluded that the hydrodynamics of the rotor is not particularly sensitive to the phase between blades and surge, and therefore to the initial blades position. This was also found by Sheng et al. (2016), who studied the effect of varying the initial blade azimuth under surge motion and found that the hydrodynamic coefficients are not very sensitive to the phase angle [38]. Moreover, since the mean values and the envelopes of the hydrodynamic coefficients are only marginally affected by changes in phase, the platform's yawing motion is expected to have a weak influence on the hydrodynamics of the vertical-axis tidal turbine when compared to surging motion. This is in line with what was found by Wang et al. in [41].

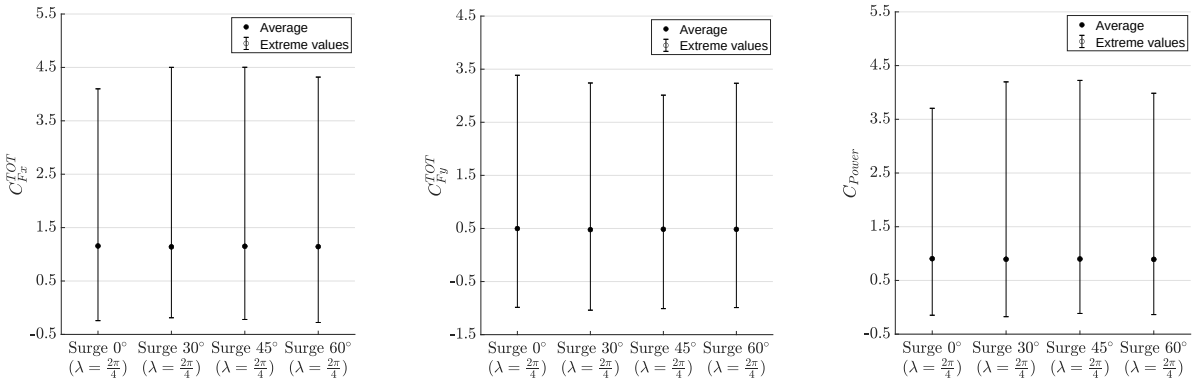

Figure 5.16: Comparison of the average and extreme values of the thrust, lateral force and power coefficients of the Haineng 1 turbine at sub-optimal operation (U_∞ = 2m/s,λ_{new} = 1.57) under intense surging conditions (A_{surge} = 1m/s,$\omega_e = \frac{2\pi}{5}$ rad/s) for different phasing between surge displacement and airfoil positions.

Table 5.4: Comparison of the minimum (min), maximum (max) and average (ave) values of the thrust, lateral force and power coefficients of the Haineng 1 turbine at sub-optimal operation (U_∞ = 2m/s,λ_{new} = 1.57) under intense surging conditions (A_{surge} = 1m/s,$\omega_e = \frac{2\pi}{5}$ rad/s) for different phasing between surge displacement and airfoil positions. The relative percent change with respect to the intense surge case with phase of 0°is indicated.

	C_{Fx}^{TOT}			C_{Fy}^{TOT}			C_{power}^{TOT}		
	min	max	ave	min	max	ave	min	max	ave
Surge 0°	-0.24	4.10	1.16	-0.99	3.39	0.50	-0.15	3.70	0.91
Surge 30°	-0.19 (-23%)	4.50 (10%)	1.14 (-1%)	-1.04 (5%)	3.24 (-4%)	0.48 (-4%)	-0.17 (18%)	4.20 (13%)	0.89 (-1%)
Surge 45°	-0.22 (-9%)	4.50 (10%)	1.15 (-1%)	-1.01 (2%)	3.01 (-11%)	0.49 (-3%)	-0.11 (-23%)	4.22 (14%)	0.90 (-1%)
Surge 60°	-0.28 (14%)	4.32 (5%)	1.14 (-1%)	-0.99 (0%)	3.24 (-4%)	0.48 (-3%)	-0.14 (-8%)	3.98 (8%)	0.89 (-1%)

The second example consists in tuning the rotational speed Ω for the reduction of load oscillations to minimize fatigue issues. In this case, the rotation period is set to $T_{rotation} = B \cdot T_{surge}$ so that each blade experiences one full surge cycle in half rotation. The envelopes of the force and power coefficients become straight again, since the blades undergo the same flow field evolution in time shifted by 180° as in the only current case (see Figure B.13 in the Appendix). Notice that the phase difference is tuned so that the maximum positive surge velocity always occurs at 90° and 270° and the extreme negative surge velocity at 0° and 180° for both airfoils, in order to exploit surge at best. However, such tuning leads to a tip speed ratio of $\lambda = \frac{2\pi}{10} \simeq 0.62$, far from the optimal value λ_{opt}. The effects of this example of rotational speed tuning are displayed in Figure 5.17 and quantified in Table 5.5. As expected, the amplitude of oscillation of the tuned intense surge case is reduced compared to the intense surge case at optimal tip speed ratio. The increase in average power

coefficient from the reference only current case is almost halved, from 53% to 28%, and the average thrust coefficient is slightly reduced. In conclusion, this example of rotational speed tuning allows to reduce the amplitude of load oscillations and to obtain a constant, although reduced, average power output per rotation.

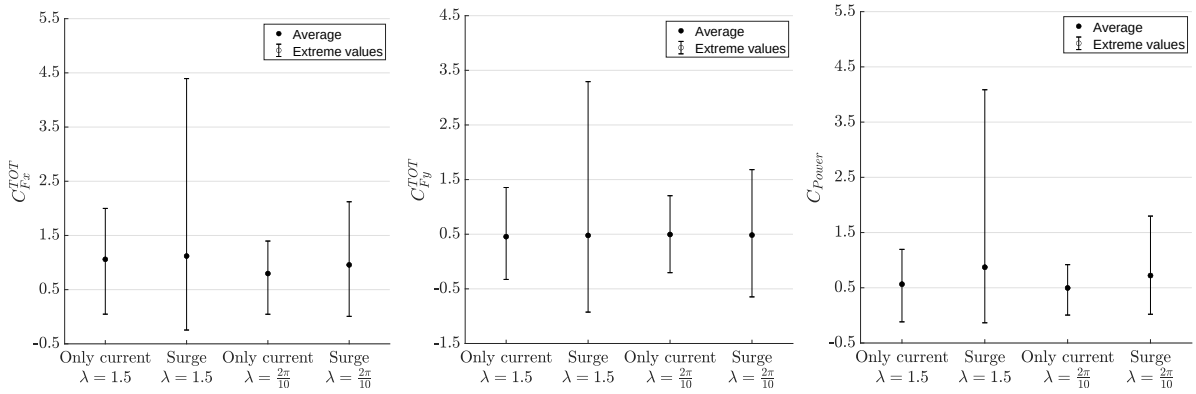

Figure 5.17: Comparison of the average and extreme values of the thrust, lateral force and power coefficients of the Haineng 1 turbine for the cases of only current inflow (U_∞ = 2m/s) and intense surge conditions (A_{surge} = 1m/s,$\omega_e = \frac{2\pi}{5}$ rad/s) at different tip speed ratios.

Table 5.5: Comparison of the minimum (min), maximum (max) and average (ave) values of the thrust, lateral force and power coefficients of the Haineng 1 turbine for the cases of only current inflow (U_∞ = 2m/s) and intense surge conditions (A_{surge} = 1m/s,$\omega_e = \frac{2\pi}{5}$ rad/s) at different tip speed ratios. The relative percent change with respect to the only current case with λ of 1.5 is indicated.

	C_{Fx}^{TOT}			C_{Fy}^{TOT}			C_{power}^{TOT}		
	min	max	ave	min	max	ave	min	max	ave
Only current λ = 1.5	0.05	2.00	1.06	-0.33	1.36	0.46	-0.12	1.20	0.57
Intense surge λ = 1.5	-0.25 (-621%)	4.40 (120%)	1.11 (5%)	-0.93 (183%)	3.29 (143%)	0.47 (3%)	-0.13 (15%)	4.09 (242%)	0.86 (53%)
Only current λ = 0.62	0.05 (-4%)	1.40 (-30%)	0.80 (-25%)	-0.20 (-38%)	1.20 (-11%)	0.50 (9%)	0.01 (-105%)	0.92 (-23%)	0.50 (-12%)
Intense surge λ = 0.62	0.01 (-85%)	2.12 (6%)	0.96 (-10%)	-0.65 (97%)	1.68 (24%)	0.48 (6%)	0.02 (-118%)	1.80 (50%)	0.72 (28%)

5.3. Case study: Kobold turbine under intense surge

In this section, the hydrodynamic response of the Kobold vertical-axis tidal turbine to the intense surge case study is simulated. The analysis follows the same procedure as the Haineng 1 in section 5.2. The Kobold turbine is fundamentally different from the Haineng 1 in terms of geometry, e.g. in the number of blades and solidity, and operating conditions (λ_{opt}). The interaction with the intense surge conditions is strongly dependent on these parameters. Nevertheless, the analysis will reveal that the response of the Kobold turbine to intense surging motion shares similarities with the findings of the Haineng 1's case study.

5.3.1. Effect of surge on the hydrodynamic coefficients

The time history curves of the thrust force, lateral force and power coefficients in the reference case and in the case study are illustrated, respectively, in Figures 5.18, 5.19 and 5.20. From the comparison of the curves in the two cases simulated, the impact of platform's surging motion can be recognized in the modified frequency and amplitude of oscillation.

In the only current reference case, the rotor loads oscillate with frequency of $3 \cdot \Omega$ between straight envelopes (red dotted lines), given steady inflow conditions and constant operational parameters. Introducing surge motion affects the shape of the time evolution of the coefficients, increasing the amplitude of oscillation and the spikiness. The oscillations of the thrust coefficient are evidently dominated by the effect of surge velocity on the relative velocity in x-direction, as can be seen in Figure 5.18(b): the rotor experiences an increase in thrust force when the surge velocity is positive, an analogous decrease when the surge velocity is negative and it almost overlaps the thrust curve of the only current reference case when the surge velocity is

instantaneously null. Instead, the lateral force coefficient is dominated by the effect of rotational frequency, as can be seen in Figure 5.19.

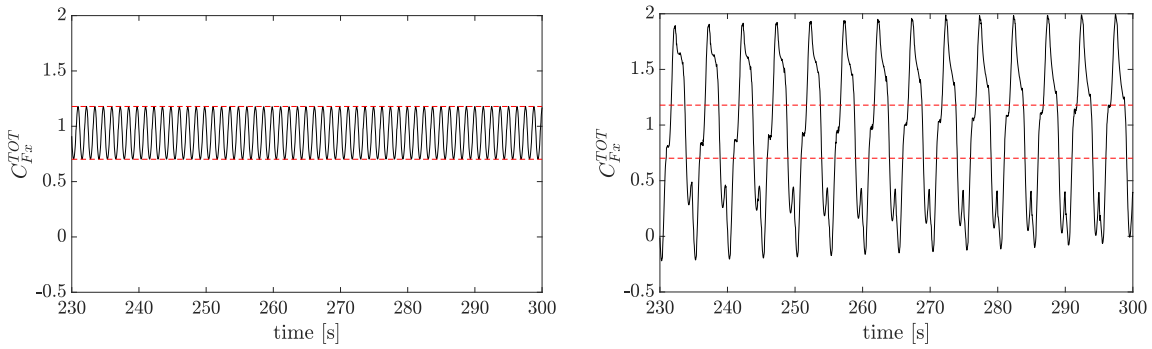

(a) Only current (b) Intense surge

Figure 5.18: Comparison of the time history of the Kobold rotor thrust coefficient for: (a) the only current case ($U_\infty = 2$m/s,$\lambda = 2.5$) and (b) the intense surge case ($U_\infty = 2$m/s,$\lambda = 2.5$,$A_{surge} = 1$m/s,$\omega_e = \frac{2\pi}{5}$rad/s).

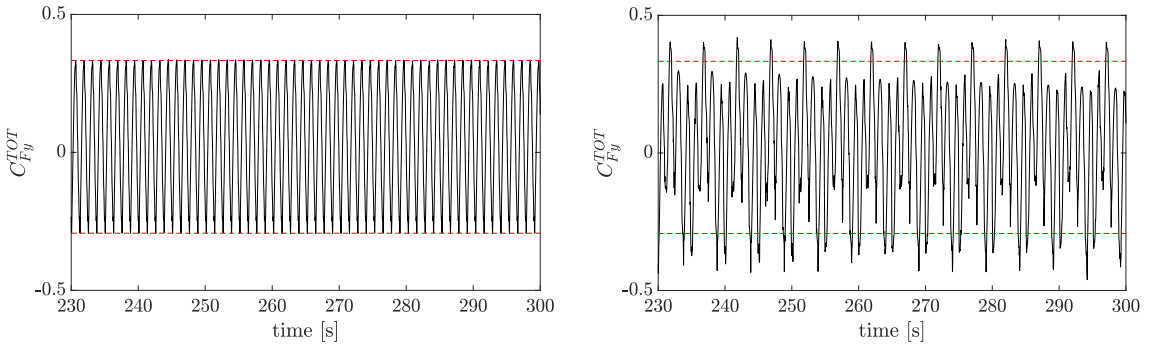

(a) Only current (b) Intense surge

Figure 5.19: Comparison of the time history of the Kobold rotor lateral force coefficient for: (a) the only current case ($U_\infty = 2$m/s,$\lambda = 2.5$) and (b) the intense surge case ($U_\infty = 2$m/s,$\lambda = 2.5$,$A_{surge} = 1$m/s,$\omega_e = \frac{2\pi}{5}$rad/s).

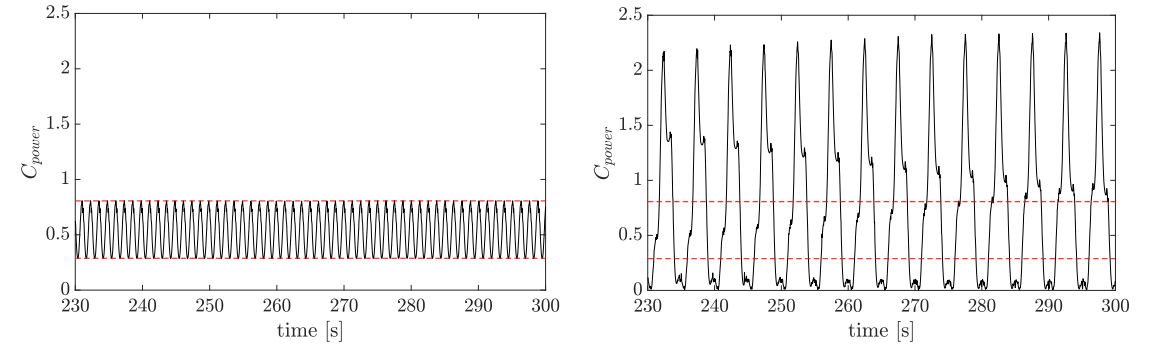

(a) Only current (b) Intense surge

Figure 5.20: Comparison of the time history of the Kobold rotor power coefficient for: (a) the only current case ($U_\infty = 2$m/s,$\lambda = 2.5$) and (b) the intense surge case ($U_\infty = 2$m/s,$\lambda = 2.5$,$A_{surge} = 1$m/s,$\omega_e = \frac{2\pi}{5}$rad/s).

The effect of intense surge on the average and extreme values of the hydrodynamic coefficients is illustrated in Figure 5.21 and quantified in Table 5.6. As in the case of Haineng 1, the amplitude of oscillation is widened by the intense surge conditions and the mean power coefficient is increased due to additional energy extraction from platform's motion; the average loading is only marginally affected. The increase in the

extremes of load oscillation leads to more critical fatigue issues. On the other hand, the increase in power coefficient is beneficial and surge can be potentially exploited for enhanced power production.

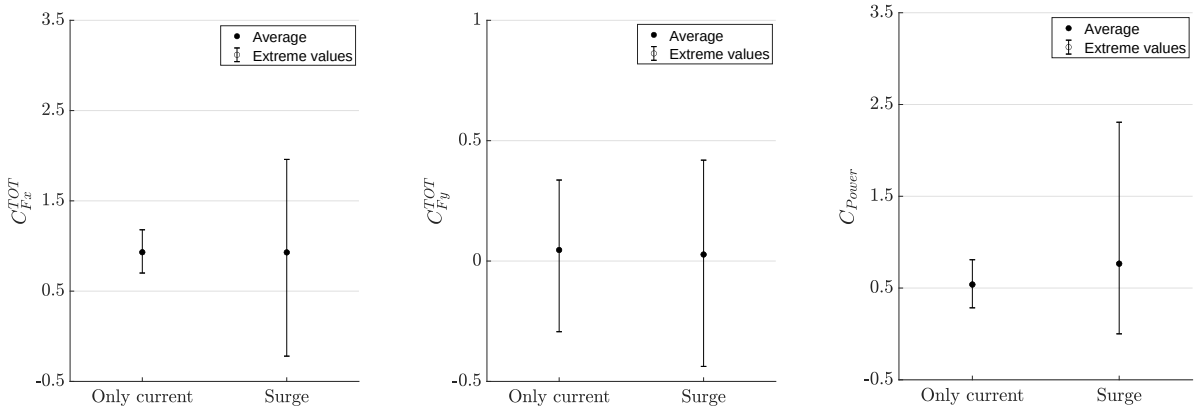

Figure 5.21: Comparison of the average and extreme values of the thrust, lateral force and power coefficients of the Kobold turbine for the only current reference case (U_∞ = 2m/s,λ = 2.5) and intense surging motion (U_∞ = 2m/s,λ = 2.5,A_{surge} = 1m/s,$\omega_e = \frac{2\pi}{5}$rad/s).

Table 5.6: Comparison of the minimum (min), maximum (max) and average (ave) values of the hydrodynamic coefficients of the Kobold turbine in the only current reference case (U_∞ = 2m/s,λ = 2.5) and in the intense surge case study (U_∞ = 2m/s,λ = 2.5,A_{surge} = 1m/s,$\omega_e = \frac{2\pi}{5}$rad/s). The relative percent change due to surge is indicated.

	C_{Fx}^{TOT}			C_{Fy}^{TOT}			C_{power}^{TOT}		
	min	max	ave	min	max	ave	min	max	ave
Only current	0.70	1.18	0.93	-0.29	0.34	0.05	0.28	0.81	0.54
Intense surge	-0.22 (-131%)	1.96 (66%)	0.93 (0%)	-0.44 (49%)	0.42 (25%)	0.03 (-41%)	0.00 (-100%)	2.31 (185%)	0.77 (42%)

5.3.2. Identification of the fundamental frequencies of oscillation

The effect of surge on the frequency of oscillation of the simulation quantities can be summarized by the power spectral density graphs of the relative velocity at quarter chord of one blade in Figure 5.22. While in the only current case the only fundamental frequency is the frequency of rotation Ω, under intense surge two additional frequencies can be identified: the surge frequency ω_e of $0.2Hz$ and the frequency at which the relative velocity repeats almost identically at the blade of $0.06Hz$. Similarly to the intense surge case simulated for the Haineng 1 turbine, the latter frequency can be computed manually considering that the velocity field repeats at the blade after an entire number of rotations and of surge cycles.

High-frequency oscillations appear in between the multiples of the fundamental frequencies in both cases, and these small peaks are related either to periodic blade vortex shedding or to frequency spectrum leakage. Under intense surging motion, the high-frequency oscillations have a larger spectral power density content because of the modified wake evolution and interactions of the airfoil with the other airfoils and wake elements, consequently impacting on the time history of the induced component of the relative velocity.

5.3.3. Time evolution of the velocity triangles

The widening and oscillation of the envelopes and the introduction of an irregular shape due to surge can be also observed in the time evolution of the relative velocity at quarter chord of one blade of Figure 5.24. As discussed in section 5.2.3, the instantaneous surge velocity has a dominant effect on determining the amplitude of oscillation of the envelopes of the magnitude and orientation of the relative velocity, as can be seen in Figure 5.25. The irregular shape of the magnitude of the relative velocity (see Figure 5.24) and of the angle of attack (see Figure 5.26) originates from the induced velocity, which mostly impacts the x-direction introducing small peaks in the velocity profile.

The intense surge conditions affect the wake evolution profile with the same process previously described for the Haineng 1 turbine in 5.2.3. The modified wake profile of the Kobold under intense surge compared to the only current case is similar to the Haineng 1's, and it can be seen in Figure B.12 of the Appendix. Similarly

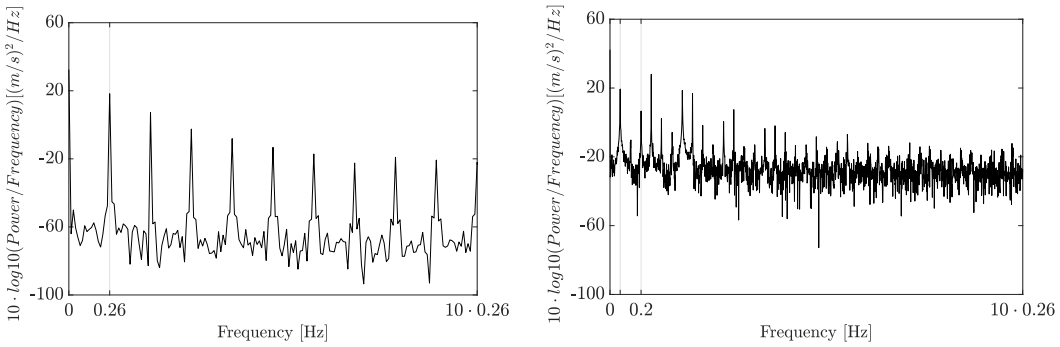

(a) Only current (b) Intense surge

Figure 5.22: Comparison of the spectral power density of the relative velocity at quarter chord of one blade of the Kobold turbine for: (a) the only current case ($U_\infty = 2$m/s,$\lambda = 2.5$) and (b) the intense surge case ($U_\infty = 2$m/s,$\lambda = 2.5, A_{surge} = 1$m/s,$\omega_e = \frac{2\pi}{5}$rad/s).

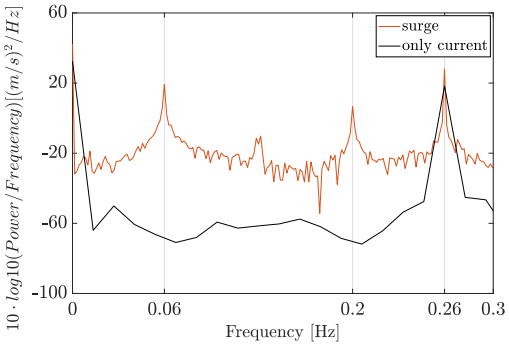

Figure 5.23: Visualization of the fundamental frequencies of the spectral power density of the relative velocity at quarter chord of one blade of the Kobold turbine for the only current reference case ($U_\infty = 2$m/s,$\lambda = 2.5$) and the intense surge case study ($U_\infty = 2$m/s,$\lambda = 2.5, A_{surge} = 1$m/s,$\omega_e = \frac{2\pi}{5}$rad/s).

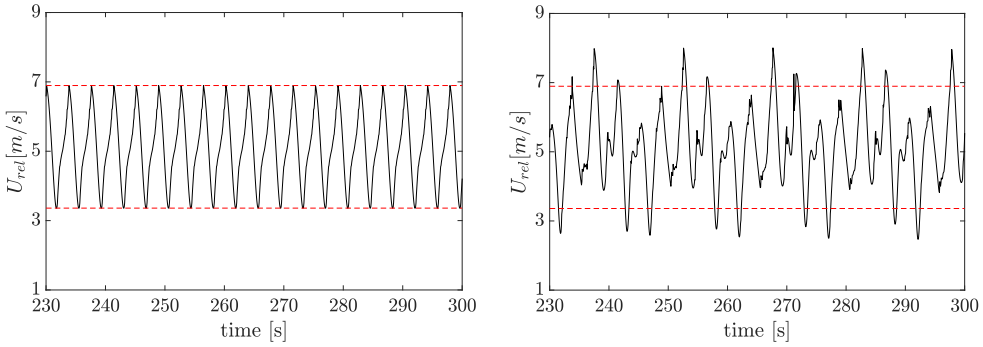

(a) Only current (b) Intense surge

Figure 5.24: Comparison of the time history of the relative velocity at one blade of the Kobold turbine for: (a) the only current case ($U_\infty = 2$m/s,$\lambda = 2.5$) and (b) the intense surge case ($U_\infty = 2$m/s,$\lambda = 2.5, A_{surge} = 1$m/s,$\omega_e = \frac{2\pi}{5}$rad/s).

to the Haineng 1's wake evolution, spindle-shaped wake zones are created downwind at every surge period, and the increased blade-vortex interaction in the near wake results in the irregular shape of the induced velocity evolution in time and in the small peaks at high frequencies identified in the PSD graph of Figure 5.22(b). The modified time evolution of the induced velocity components can be observed in Figures B.8, B.9, B.10 and B.11 in the Appendix, for which the same consideration of the Haineng 1's apply. However, the different number of blades has implications on the time evolution of the induced velocity. The third blade introduces one additional wake element shed at the trailing edge per time step and 190 additional panels, which contribute to the computation of the induced velocity at a given point, introducing more oscillations.

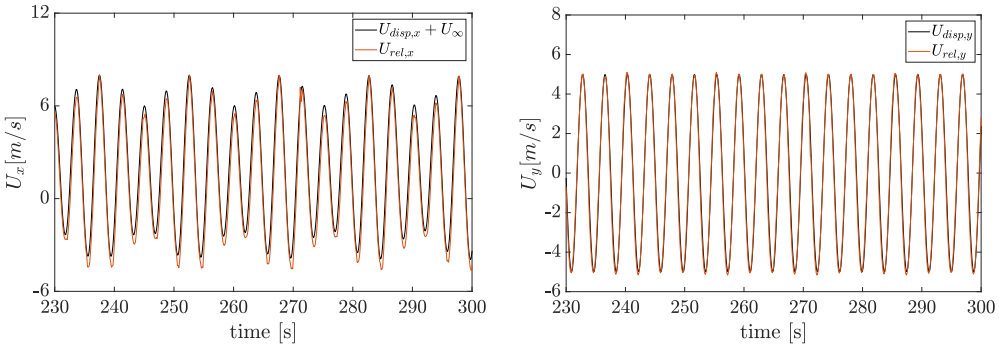

(a) Horizontal relative velocity (b) Vertical relative velocity

Figure 5.25: Comparison of the relative velocity at one blade of the Kobold turbine in the intense surge case ($U_\infty = 2$m/s,$\lambda = 2.5$,$A_{surge} = 1$m/s,$\omega_e = \frac{2\pi}{5}$rad/s) in x-direction (a) and y-direction (b), with the induction (orange curve) and without the induction (black curve).

The additional wake elements can be noticed when comparing Figure B.12 to Figure 5.13. Moreover, the three blades are distanced 120° (instead of 180° of the Haineng 1), which affects the distance between control points and the shedding position of the vortices. The effect of the introduction of the third blade is evident from the more irregular profile due to more frequent blade-vortex interactions, which is directly dependent on the increase in number of the singularity elements used in the computation.

The time history of the angle of attack of one blade reveals a relatively small range compared to the Haineng 1 turbine, mostly depending on the higher operational tip speed ratio of the Kobold. Because of the reduced amplitude of oscillation of the angle of attack, the overestimation due to viscous effects is reduced and corrections are not as significant as in the simulations of the Haineng 1 turbine.

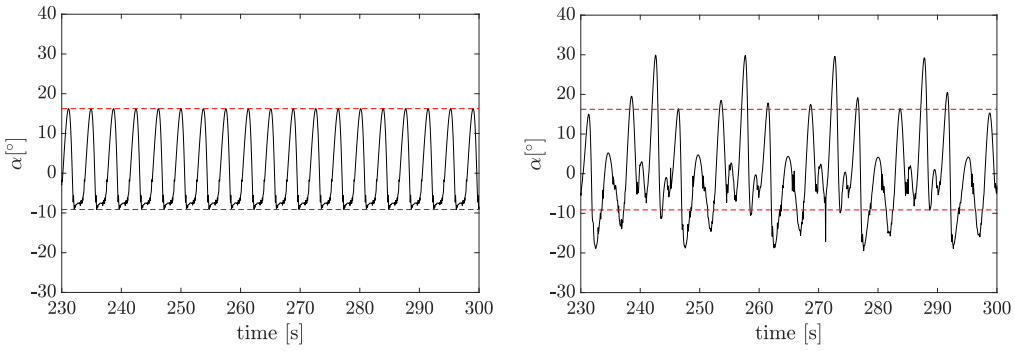

(a) Only current (b) Intense surge

Figure 5.26: Comparison of the time history of the angle of attack of one blade of the Kobold turbine for: (a) the only current case ($U_\infty = 2$m/s,$\lambda = 2.5$) and (b) the intense surge case ($U_\infty = 2$m/s,$\lambda = 2.5$,$A_{surge} = 1$m/s,$\omega_e = \frac{2\pi}{5}$rad/s).

5.3.4. Possible tuning of the rotor parameters for controlling the hydrodynamic response to surge

In this section, two examples of possible tuning of the operational parameters of the Kobold turbine are presented, based on the examples conducted for the Haineng 1 turbine. The phase tuning for power extraction optimization is investigated in the first example. The second example demonstrates how the tuning of the rotational speed allows to obtain straight envelopes of the hydrodynamic coefficients under surging motion. The inputs to the simulations for the two tuning examples are reported in Tables B.4 and B.5 of the Appendix.

In order to study the effect of phasing between the surge velocity and the blades position, the rotational speed is changed into a sub-optimal value so that the ratio between the surge period and rotation period is a finite number and the phase can be easily defined for each blade over the rotations. The modified tip speed ratio corresponding to the new rotational speed is $\lambda_{new} = \frac{2\pi}{4/3T_{surge}} \frac{R}{U_\infty} = 2.51$, where the rotation period is $4/3T_{surge}$ so that one surge cycle lasts exactly one and one third rotations. This implies that at every surge

cycle, each blade will experience exactly the same flow field experienced by the blade before it in the previous surge period, thus with the same phase with respect to surge velocity. In this example, the surge phase Φ_{surge} is set to $-180°$ in order to have maximum positive surge velocity at the initial blade position of airfoil 1, and the initial azimuth of one blade is varied for comparison to $0°, 30°, 45°, 60°$ and $90°$. The effect of different phasing on the average and extreme values of the hydrodynamic coefficients is reported in Figure 5.27 and in Table 5.7. The force and power coefficients are evidently not very sensitive to the phasing between surge motion and blades, which confirms the findings of the phasing example of the Haineng 1 turbine of section 5.2.4. Moreover, the sensitivity of the simulation results to the initial blade azimuth is reduced compared to the Haineng 1 turbine because of the introduction of the third blade.

The rotational frequency is tuned in the second example in order to obtain straight envelopes. By setting the rotation period to $B \cdot T_{surge} = 15s$, the surge velocity is perceived by each blade in the same way over the rotation. The hydrodynamic coefficients and their straight envelopes are presented in Figure B.14 of the Appendix. However, this results in a tip speed ratio of around 0.62 which severely impacts on the power extraction as can be seen in Figure 5.28 and in Table 5.8. Since the $C_{power} - \lambda$ curve of the Kobold is steeper than the Haineng 1's (see Figure 5.1), this tuning is not beneficial in terms of performance, which average value decreases by 28% with respect to the only current reference case at optimal tip speed ratio. This tuning might be convenient to reduce the amplitude of the hydrodynamic coefficients and to obtain stable average values, or in other cases with different surge conditions, for example when the surge period is small.

Because of the inviscid assumption of the U2DiVA code, an overestimation of the hydrodynamic coefficients must be considered, although small compared to the case study of the Haineng 1 turbine.

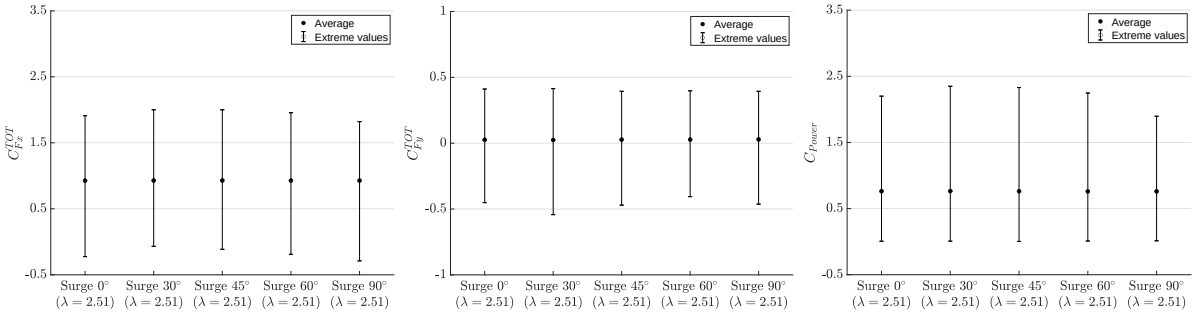

Figure 5.27: Comparison of the average and extreme values of the thrust, lateral force and power coefficients of the Kobold turbine at sub-optimal operation (U_∞ = 2m/s,λ_{new} = 2.51) under intense surge conditions (A_{surge} = 1m/s,$\omega_e = \frac{2\pi}{5}$rad/s) at different phasing between surge displacement and airfoil positions.

Table 5.7: Comparison of the minimum (min), maximum (max) and average (ave) values of the thrust, lateral force and power coefficients of the Kobold turbine at sub-optimal operation (U_∞ = 2m/s,λ_{new} = 2.51) under intense surging conditions (A_{surge} = 1m/s,$\omega_e = \frac{2\pi}{5}$rad/s) for different phasing between surge displacement and airfoil positions. The relative percent change with respect to the intense surge case with phase of 0°is indicated.

	C_{Fx}^{TOT}			C_{Fy}^{TOT}			C_{power}^{TOT}		
	min	max	ave	min	max	ave	min	max	ave
Surge 0°	-0.22	1.91	0.93	-0.45	0.41	0.03	0.01	2.20	0.76
Surge 30°	-0.07 (-70%)	2.00 (5%)	0.93 (0%)	-0.54 (20%)	0.41 (1%)	0.02 (-6%)	0.01 (11%)	2.35 (7%)	0.76 (0%)
Surge 45°	-0.11 (-50%)	2.00 (5%)	0.93 (0%)	-0.47 (4%)	0.39 (-4%)	0.03 (4%)	0.00 (-47%)	2.33 (6%)	0.76 (0%)
Surge 60°	-0.19 (-16%)	1.96 (2%)	0.93 (0%)	-0.41 (-10%)	0.40 (-3%)	0.03 (5%)	0.01 (53%)	2.25 (2%)	0.76 (0%)
Surge 90°	-0.29 (29%)	1.82 (-5%)	0.93 (0%)	-0.46 (3%)	0.39 (-4%)	0.03 (11%)	0.01 (97%)	1.90 (-14%)	0.76 (0%)

5.4. Discussion

This chapter studied the hydrodynamic response of two existing lift-driven vertical-axis tidal turbines to intense surge conditions. In section 5.1, the set-up of the simulations used for the analysis was presented. First,

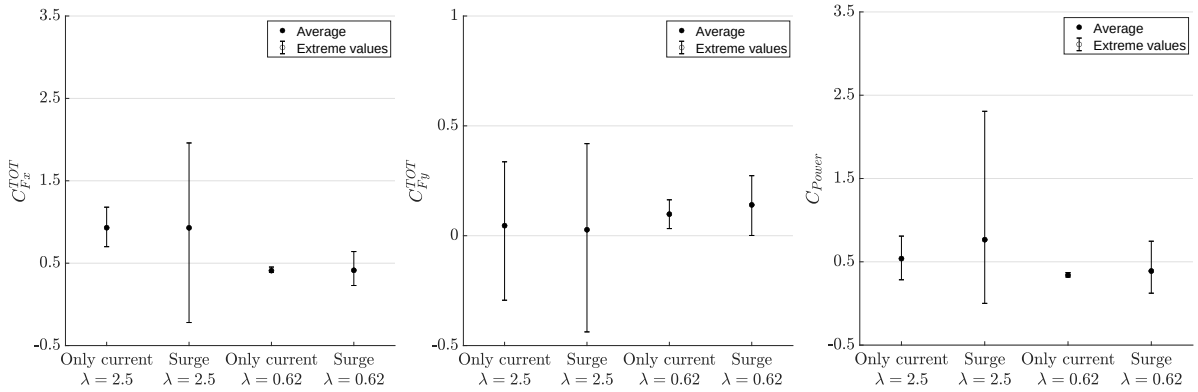

Figure 5.28: Comparison of the average and extreme values of the thrust, lateral force and power coefficients of the Kobold turbine for the cases of only current inflow (U_∞ = 2m/s) and intense surge conditions (A_{surge} = 1m/s,$\omega_e = \frac{2\pi}{5}$ rad/s) at different tip speed ratios.

Table 5.8: Comparison of the minimum (min), maximum (max) and average (ave) values of the thrust, lateral force and power coefficients of the Kobold turbine for the cases of only current inflow (U_∞ = 2m/s) and intense surge conditions (A_{surge} = 1m/s,$\omega_e = \frac{2\pi}{5}$ rad/s) at different tip speed ratios. The relative percent change with respect to the only current case with λ of 2.5 is indicated.

	C_{Fx}^{TOT}			C_{Fy}^{TOT}			C_{power}^{TOT}		
	min	max	ave	min	max	ave	min	max	ave
Only current $\lambda = 2.5$	0.70	1.18	0.93	-0.29	0.34	0.05	0.28	0.81	0.54
Intense surge $\lambda = 2.5$	-0.22 (-131%)	1.96 (66%)	0.93 (0%)	-0.44 (49%)	0.42 (25%)	0.03 (-41%)	0.00 (-100%)	2.31 (185%)	0.77 (42%)
Only current $\lambda = 0.62$	0.39 (-44%)	0.45 (-62%)	0.41 (-56%)	0.03 (-111%)	0.16 (-51%)	0.10 (114%)	0.32 (11%)	0.37 (-54%)	0.34 (-37%)
Intense surge $\lambda = 0.62$	0.23 (-67%)	0.64 (-46%)	0.41 (-56%)	0.00 (-100%)	0.27 (-19%)	0.14 (206%)	0.12 (-57%)	0.75 (-8%)	0.39 (-28%)

the range of operation of the Haineng 1 and the Kobold turbines was defined by constructing the $C_{power} - \lambda$ curves via U2DiVA reported in Figure 5.1. Second, the simulation cases of only current and intense surge were described, respectively, in sections 5.1.2 and 5.1.3. The simulation inputs are reported respectively in Table 5.1 and Table 5.2. Finally, the sensitivity of the code was analysed. About the spatial resolution, a panelling of 190 panels per airfoil with closed trailing edge was selected. About the simulation time inputs, it was found that the steadiness in results is reached after 60 rotations and that a time step size of 3° compromises between computational cost and accuracy of the results. In section 5.2, the hydrodynamic response of the Haineng 1 turbine to the two simulation cases described in 5.1.2 and 5.1.3 was analysed at different levels. The same analysis was followed in 5.3.

The oscillation of the simulation quantities introduced by the platform's motion was studied in details for the Haineng 1 and the Kobold turbines, by first quantifying the impact on the envelopes amplitude and average hydrodynamic coefficients of the two turbines respectively in sections 5.2.1 and 5.3.1, and then analysing the frequency spectrum of the relative velocity at the blade respectively in sections 5.2.2 and 5.3.2. The intense surge conditions were found to increase both the amplitude of oscillation and the frequency content of the simulation quantities. The envelopes of the hydrodynamic coefficients are widened by surge, with repercussions on the fatigue life of the blades, and the average values are marginally affected as can be seen for the Haineng 1 in Figure 5.7 and for the Kobold in Figure 5.21. For both turbines, the energy of the platform's surging motion contributes to the power coefficient, increasing it to values above the power at optimal tip speed ratio. The analysis of the power spectral density graphs revealed that when surge is imposed to the vertical-axis tidal turbines, the number of fundamental frequencies of the simulation results increases from one to three, including the rotational frequency Ω, the surge frequency ω_e and the frequency of flow repetition at one blade deriving from the combination of the first two fundamental frequencies. Furthermore, the surge cases show an increase in magnitude of the high-frequency oscillations, related to stronger and more frequent blade-vortex interactions.

The origin of the oscillations in the time history curves of the hydrodynamic coefficients was traced back to the unsteadiness introduced by the surge velocity and displacement in the evolution of the velocity tri-

angles, treated in sections 5.2.3 and 5.3.3. The surge velocity was found to be the term which dominantly affects the envelopes of the simulation quantities, widening the range of oscillation especially in x-direction. The high-frequency peaks found in the frequency analysis, as well as the spikes of the hydrodynamic coefficients, derive from the modified time evolution of the induced velocity at the blade. The unsteadiness of surge generates a modified time evolution of the strength and position of the singularity elements, either on the airfoils' panels and in the wake. The effect of surge on the wake trajectory and therefore on the induction is evident from the far-wake profile (see Figure 5.13 and Figure B.12) and from the interaction of the rotor with the near-wake (see Figure 5.12). The far-wake is characterised by spindle-shaped wake zones, while in the near wake the number of wake elements sufficiently close to the rotor to have a significant contribution to the induction continuously changes in time depending on the relative position of the rotor with respect to the wake. The introduction of a third blade with the Kobold turbine introduces more wake elements, resulting in more irregularities in the time history of the induced velocity.

The time evolution of the angle of attack also reveals the limitations of the U2DiVA code when simulating the platform's motions. Since surge increases the amplitude of oscillation of the angle of attack, the overestimation of the hydrodynamic coefficient due to the potential flow assumption is stronger in the intense surge case compared to the only current case for both turbines. However, the range of angles of attack of the Haineng 1 turbine is almost double the range experienced by the Kobold's blades, meaning that viscous effects are dependent on the geometry, the rotor operating parameters and the inflow conditions.

Finally, two examples of tuning of the rotor operating parameters of the Haineng 1 and the Kobold are implemented and discussed respectively in 5.2.4 and 5.3.4, with the aim of controlling the hydrodynamic response of the vertical-axis turbines to the surge conditions. A first example tuning the phase difference between the rotor and surge revealed that the simulation results are not particularly sensitive to the initial blade azimuth, as can be seen in Figure 5.16 and in Figure 5.27. Consequently, yawing motion is expected to weakly impact on the hydrodynamic response of vertical-axis tidal turbines. This is in agreement with the results of Wang et al. in [41], reported in Chapter 4. The second example involves the tuning of the rotational speed aimed at obtaining straight envelopes of the force coefficients with a reduced amplitude of oscillation. It was found to be beneficial for the Haineng 1 turbine in 5.2.4, as it mitigates fatigue issues with a marginal reduction of the power extraction (see Figure 5.17). Instead, this tuning leads to halve the power production of the Kobold turbine under intense surging motion as can be seen in Figure 5.28, being the $C_{power} - \lambda$ curve of the Kobold turbine steep around the optimal point of operation.

6

Conclusions

The study of the fluid-structure interactions of vertical-axis tidal turbines under the floating carrier's motions is a challenging research topic. The current scientific literature commonly investigates the topic using computational fluid dynamics, which is the most computationally expensive method available for the modelling of vertical-axis turbines. In this project, the 2D free-wake vortex panel method was presented as an alternative to 2D CFD, characterised by similar accuracy and reduced computational time. First, the U2DiVA code used in this project, based on the theory as described in [37], was outlined in Chapter 3. Its reliability in representing the hydrodynamic response of vertical-axis tidal turbines to harmonic platform's motions was analysed in Chapter 4 by reproducing some of the simulation cases reported in the scientific literature, and the advantages and limitations of the U2DiVA code compared to 2D CFD were discussed. Having verified the code against 2D CFD, two existing tidal turbines were simulated in a reference case without platform's motion and a case study including surge in Chapter 5. The hydrodynamic response of the rotors to the two cases were compared. In particular, the analysis was focused on the impact of surge on the amplitude and frequency of oscillation of the hydrodynamic coefficients and on the time evolution of the inflow perceived at the blades.

The research questions formulated in Chapter 1 are answered in section 6.1 through the findings of the research conducted in this project. Section 6.2 discusses the possible improvements and future work regarding the topic.

6.1. Conclusions

In this project, the Unsteady Two-Dimensional Vorticity Aerodynamics model (U2DiVA) [47] was applied as a computationally effective alternative to study the details of the fluid-structure interactions of vertical-axis tidal turbines under harmonic floating platform's motions. Through the code verification against the results of the scientific literature, the U2DiVA code revealed to be a relatively fast and reliable tool for the simulations of the effect of 2D platform's motions on the hydrodynamic coefficients of vertical-axis tidal turbines. The U2DiVA code is characterised by a computational time of the order of magnitude of minutes to a few hours, extremely short when compared to the computationally expensive CFD simulations. Moreover, the setting-up of U2DiVA simulations is relatively simple and mostly depends on the definition of the time step size and panelling density. The process of meshing of the computational domain in 2D CFD, allowing the mesh to move with the turbine rotation and platform's motions, is more time-consuming and the simulation results are extremely sensitive to multiple simulation inputs (e.g. meshing, differentiation scheme and turbulence model). When defining the set-up of U2DiVA code simulations, a trade-off of the panelling and time stepping inputs must be chosen through a convergence study in order to guarantee good accuracy and a reasonable computational time. Increasing the density of panelling has a largely positive influence on the accuracy and causes marginally higher computational cost, as more panels result in a larger solution matrix. The airfoil panelling must be closed at the trailing edge for applying the Kutta condition correctly, and the grid at the airfoil edges should be denser for capturing the flow phenomena in the critical points. Instead, decreasing the time step size directly affects the computational time of the simulation, while increasing the accuracy. However, extremely small time steps do not guarantee more accurate results as numerical instability might occur. Finally, the combination of number of panels and time step size should be selected carefully as numerical instability rise when the non-dimensional distance of the trailing edge vortex is smaller than the

size of the panels at the trailing edge. The accuracy of the code is limited by the intrinsic assumption of 2D potential flow, i.e. three-dimensional and viscous losses are not accounted for. In vertical-axis tidal turbines, the assumption of incompressible flow holds while viscous effects are not negligible and increase as the angle of attack increases. The magnitude of the overestimation related to the inviscid assumption is strongly dependent on the operating parameters and on the surge conditions. These parameters influence the range of variation of the angle of attack perceived at the blade, which is directly correlated to the magnitude of viscous effects experienced at the blade. For instance, in the simulations of Chapter 5, the range of angles of attack experienced by the blades of the Kobold turbine is half the range experienced by the Haineng 1, mostly due to the different operational tip speed ratio. Consequently, the viscous effects are almost negligible in the cases simulated for the Kobold turbine, while corrections are needed for the Haineng 1. Possible viscosity corrections should account for flow conditions at very low Reynolds numbers and small Mach number. The assumptions at the base of the U2DiVA code also limit the investigation of the dynamic stall phenomenon and flow separation.

The simulations of the intense surge case of the Haineng 1 and the Kobold turbines indicate that the platform's surging motion affects the amplitude and frequency of oscillation of the simulation quantities. Surge induces oscillations of the hydrodynamic coefficients in a wider range, influencing both the maxima and minima. This has implications on the fatigue life of the turbine, which undergoes stronger and more irregular loads in horizontal and vertical direction. On the other hand, surge is beneficial to power extraction as the power coefficient is found to be increased on average compared to the only current reference case.

The oscillations of the coefficients are also affected in terms of frequency content. First, two additional fundamental frequencies are introduced: the frequency of surge and the frequency at which the flow repeats (almost) exactly at the blade, which results from the combination of the frequency of rotation and the surge frequency. The large peaks of the power spectral density graphs occurring at the fundamental frequencies derive from the rotational speed, current velocity and surge velocity components. Second, the high-frequency peaks in between of the multiples of the fundamental frequencies increase in number and in magnitude, meaning that the induced velocity is more irregular and has larger amplitude of oscillation. The time history of the induced velocity is affected by the change in singularity elements strength and position in time, both on the airfoils' panels and in the wake. Spindle-shaped regions are generated at every surge period in the far-wake, while the near-wake is characterised by unsteady interactions of the blades in either downwind or upwind position with the wake vortex points. The introduction of a third blade introduces more wake elements therefore a more irregular behaviour of the time history of the induced velocity. The examples of tuning of rotor operating parameters conducted in this project suggest that control strategies could be developed either for the exploitation of surge for enhanced power extraction or for the reduction of cyclic loading. The rotation period can be tuned in order to modify its relationship with the surge period, and it strongly impacts the hydrodynamic response to surge. The tuning of rotational speed is convenient in a specific range of tip speed ratios defined by the characteristic $C_{power} - \lambda$ curve of the turbine. Differently from the rotational speed, the initial blade azimuth of the turbine is not a determining parameter of the hydrodynamic response to the surging motion; this result suggests that yawing motion should weakly impact the hydrodynamics of the rotor compared to surge.

In conclusion, the effect of floating platform's motions on the fluid-structure interaction of vertical-axis tidal turbines can be studied with a 2D free-wake vortex panel method. The results are conservative and computed at a relatively low computational cost. The analysis of two existing tidal turbines under surging motion reveals that surge introduces unsteadiness in the flow perceived at the blade, affecting the hydrodynamic loads and the wake characteristics. Understanding the variation of the rotor loads under surging motion is beneficial for evaluating the structural strength and fatigue life when designing the blades and for the design of the floating platform and mooring lines. Additionally, the analysis of the fluctuations introduced by surge on the hydrodynamic coefficients and the study of the sensitivity to rotor operating conditions could be relevant for the design of possible control strategies allowing surge energy exploitation or cyclic load reduction.

6.2. Recommendations

In this section, the recommendations for the use of the U2DiVA code and for future applications and developments of the solver are presented.

The U2DiVA code is recommended for a relatively fast and conservative representation of the fluid-structure interactions of a vertical-axis tidal turbine under floater's motions. In tidal applications, the potential flow assumption at the base of the code doesn't hold because of the low Reynolds numbers typical of tidal currents.

The quality of the results could be further improved by including corrections in the code. The compressibility correction is generally not needed for tidal applications, because of the extremely low Mach numbers typical of tidal flows. Including viscous effects allows for a more precise estimation of the loads, especially the peak loading, and can potentially yield an accuracy close to the results of CFD simulations. The prediction of the hydrodynamic response of the turbine is accurate when the panelling and time step size are correctly selected, avoiding numerical instabilities while having a sufficiently smooth resolution to capture the flow. The panelling needs to be sufficiently fine, with closed trailing edge and high density of panels around the edges; the time step size should be small enough for smooth results but not extremely small in order to avoid numerical instabilities.

The same method can be used in future work for studying the details of the hydrodynamics of vertical-axis tidal turbines under other 2D motions, either coupled and uncoupled. The findings of the case study applying surging motion on two existing vertical-axis tidal turbines can be useful for the study of swaying motion. Furthermore, the free-wake vortex panel method could be implemented in three-dimensions in order to deal with other platform's motions (heave, pitch and roll) and include 3D effects. Extending the calculations to the third dimension would allow the modelling of arm effects and tower shadow effects.

Since the free-wake method implemented in the U2DiVA code dominates the computational time, replacing it with a fixed-wake method could further reduce the computational cost of this approach. In the fixed-wake method, either the location or the velocity of the wake vortex points is prescribed in time; therefore, the effects of the modified wake trajectory on the induced velocity are not modelled. Nevertheless, reducing the computational time could be fundamental for the future coupling of the code with a tool modelling the floating carrier's dynamics. For a more realistic representation of the sea conditions, the wave inducing the platform's motions could be modelled in the inflow conditions (*wind script file*) and they could be described as irregular, instead of the simply harmonic waves used in this study.

Through the results of the U2DiVA code simulating the effects of platform's motions on the hydrodynamic response of vertical-axis tidal turbines, control strategies could be developed which tune the rotor operating parameters in order to increase or stabilize the loading and performance.

Bibliography

[1] S.S. Khalid, Z. Liang, and N. Shah. "Harnessing tidal energy using vertical axis tidal turbine". In: *Research Journal of Applied Sciences, Engineering and Technology* 5.1 (2012), pp. 239–252.

[2] *Ocean Energy: The next big thing in energy*. 2020. URL: https://www.oceanenergy-europe.eu/ocean-energy/.

[3] EC/European Commission. *Report from the Commission to the European Parliament and the Council. On progress of clean energy competitiveness*. 2020.

[4] EC/European Commission. *Communication from the Commission to the European Parliament, the Council, the European Economic and Social Committee and the Committee of the Regions. An EU Strategy to harness the potential of offshore renewable energy for a climate neutral future*. 2020.

[5] F.O. Rourke, F. Boyle, and A. Reynolds. "Tidal energy update 2009". In: *Applied energy* 87.2 (2010), pp. 398–409.

[6] M.S. Chowdhury et al. "Current trends and prospects of tidal energy technology". In: *Environment, Development and Sustainability* (2020), pp. 1–16.

[7] Ocean Energy Europe. *2030 Ocean Energy Vision: Industry analysis of future deployments, costs and supply chains*. 2020.

[8] *Orbital Marine Power: Leaders in tidal energy technology*. 2020. URL: https://orbitalmarine.com/.

[9] Minesto. *France / Tidal Stream Industry Energiser Project (TIGER)*. 2019. URL: https://minesto.com/projects/france-tiger.

[10] EC/European Commission. *Study on Lessons for Ocean Energy Development*. 2017.

[11] C. Hu et al. "Coupled Motion Prediction of a Floating Tidal Current Power Station with Vertical Axis Twin-rotor Turbine". In: *Journal of Coastal Research* 103.SI (2020), pp. 784–788.

[12] M. Borg, M. Collu, and F.P. Brennan. "Offshore floating vertical axis wind turbines: advantages, disadvantages, and dynamics modelling state of the art". In: *The International Conference on Marine & Offshore Renewable Energy (MORE 2012)*. RINA HQ London. 2012, pp. 26–27.

[13] E.I. Baring-Gould et al. "A Review of the Environmental Impacts for Marine and Hydrokinetic Projects to Inform Regulatory Permitting: Summary Findings from the 2015 Workshop on Marine and Hydrokinetic Technologies, Washington, DC". In: (2016).

[14] X.W. Zhang et al. "Research on the unsteady hydrodynamic characteristics of vertical axis tidal turbine". In: *China ocean engineering* 28.1 (2014), pp. 95–103.

[15] F. Trivellato and M. R. Castelli. "Appraisal of Strouhal number in wind turbine engineering". In: *Renewable and Sustainable Energy Reviews* 49 (2015), pp. 795–804.

[16] F. Scheurich, T. Fletcher, and R. Brown. "The influence of blade curvature and helical blade twist on the performance of a vertical-axis wind turbine". In: *48th AIAA aerospace sciences meeting including the new horizons forum and aerospace exposition*. 2010, p. 1579.

[17] R. Whittlesey. "Vertical axis wind turbines: Farm and turbine design". In: *Wind Energy Engineering*. Elsevier, 2017, pp. 185–202.

[18] M.N. Kaya and Y. Celik. "Vertical Axis Wind Turbines for Turkey: Overview to Application Opportunities". In: 2018.

[19] C. Ma, M. Wang, and D. Zhang. "Representative technology development of marine renewable energy in China". In: *IOP Conference Series: Earth and Environmental Science* 227.2 (2019), p. 022013. URL: https://doi.org/10.1088/1755-1315/227/2/022013.

[20] G. Calcagno and A. Moroso. "The Kobold marine turbine: from the testing model to the full scale prototype". In: *Tidal Energy Summit, Londra* (2007).

[21] D.A.M. De Tavernier. "Aerodynamic advances in vertical-axis wind turbines". In: *research.tudelft.nl* (2021).

[22] A.A. Mohammed et al. "Vertical axis wind turbine aerodynamics: summary and review of momentum models". In: *Journal of Energy Resources Technology* 141.5 (2019).

[23] L.B. Wang, L. Zhang, and N.D. Zeng. "A potential flow 2-D vortex panel model: Applications to vertical axis straight blade tidal turbine". In: *Energy Conversion and Management* 48.2 (2007), pp. 454–461.

[24] I. Paraschivoiu. "Double-multiple streamtube model for Darrieus wind turbines". In: NASA. Lewis Research Center Wind Turbine Dyn. 1981.

[25] H. Beri, Y. Yao, et al. "Double multiple streamtube model and numerical analysis of vertical axis wind turbine". In: *Energy and Power Engineering* 3.03 (2011), p. 262.

[26] M. Collu et al. "FloVAWT: progress on the development of a coupled model of dynamics for floating offshore vertical axis wind turbines". In: *ASME 2013 32nd International Conference on Ocean, Offshore and Arctic Engineering*. American Society of Mechanical Engineers Digital Collection. 2013.

[27] F. Kanyako and I. Janajreh. "Vertical Axis Wind Turbine performance prediction for low wind speed environment". In: *2014 IEEE Innovations in Technology Conference*. IEEE. 2014, pp. 1–10.

[28] D.P. Coiro et al. "Dynamic behavior of novel vertical axis tidal current turbine: Numerical and experimental investigations". In: *The Fifteenth International Offshore and Polar Engineering Conference*. International Society of Offshore and Polar Engineers. 2005.

[29] C.J. Simão Ferreira et al. "Comparison of aerodynamic models for vertical axis wind turbines". In: *Journal of Physics: Conference Series*. Vol. 524. 1. IOP Publishing. 2014, p. 012125.

[30] H.A. Madsen. *Actuator cylinder. A flow model for vertical axis wind turbines*. 1982.

[31] Z. Cheng et al. "Aerodynamic modeling of floating vertical axis wind turbines using the actuator cylinder flow method". In: *Energy procedia* 94 (2016), pp. 531–543.

[32] Z. Cheng et al. "A fully coupled method for numerical modeling and dynamic analysis of floating vertical axis wind turbines". In: *Renewable Energy* 107 (2017), pp. 604–619.

[33] J. Murray and M. Barone. "The development of CACTUS, a wind and marine turbine performance simulation code". In: *49th AIAA Aerospace Sciences Meeting including the New Horizons Forum and Aerospace Exposition*. 2011, p. 147.

[34] H. Akimoto, K. Iijima, and Y. Hara. "Prediction of the flow around a floating axis marine current turbine". In: *2016 Techno-Ocean (Techno-Ocean)*. IEEE. 2016, pp. 272–275.

[35] Y. Li and Sander M. Çalışal. "A discrete vortex method for simulating a stand-alone tidal-current turbine: Modeling and validation". In: *Journal of offshore mechanics and arctic engineering* 132.3 (2010).

[36] B.Y. Li, N. Karri, and Q. Wang. "Three-dimensional numerical analysis on blade response of a vertical-axis tidal current turbine under operational conditions". In: *Journal of Renewable and Sustainable Energy* 6.4 (2014), p. 043123.

[37] J. Katz and A. Plotkin. *Low-speed aerodynamics*. Vol. 13. Cambridge university press, 2001.

[38] Q. Sheng et al. "Study of the hydrodynamic derivatives of vertical-axis tidal current turbines in surge motion". In: *Renewable energy* 96 (2016), pp. 366–376.

[39] S. Hickel. *CFD for Aerospace Engineers: Introduction to Computational Fluid Dynamics*. Delft University of Technology. 2020.

[40] K. Wang et al. "The effects of yawing motion with different frequencies on the hydrodynamic performance of floating vertical-axis tidal current turbines". In: *Applied ocean research* 59 (2016), pp. 224–235.

[41] S.Q. Wang et al. "Hydrodynamic analysis of vertical-axis tidal current turbine with surging and yawing coupled motions". In: *Ocean Engineering* 155 (2018), pp. 42–54.

[42] G. Xu, H. Li, and S. Wang. "Numerical Study on the Vertical-Axis Tidal Current Turbine with Coupled Motions (Part I)". In: *Journal of Coastal Research* 97.SI (2019), pp. 273–288.

[43] Y. Guo et al. "Aerodynamics and motion performance of the H-type floating vertical axis wind turbine". In: *Applied Sciences* 8.2 (2018), p. 262.

[44] S. Weller, L. Johanning, and P. Davies. “Best practice report–mooring of floating marine renewable energy devices”. In: *MERIFIC* (2013).

[45] W. Zhang et al. “Forced motion CFD simulation and load refinement evaluation of floating vertical-axis tidal current turbines”. In: *Polish Maritime Research* 27.3 (2020), pp. 40–49.

[46] J.M.J. Journée and W.W. Massie. *Offshore hydromechanics*. 2001.

[47] C.J. Simão Ferreira. *The near wake of the VAWT: 2D and 3D views of the VAWT aerodynamics*. 2009.

[48] M.H. Eriksson, A. Moroso, and A. Fiorentino. “The vertical axis Kobold turbine in the Strait of Messina - a case study of a full scale marine current prototype”. In: *Ponte Di Archimede SpA, Italy* (2005).

[49] NACA 4 digit airfoil generator (NACA 0018 AIRFOIL). URL: http://airfoiltools.com/airfoil/naca4digit.

[50] G. Dimitriadis. *Aerodynamics, Lecture 4: Panel methods*. University Lecture.

[51] Y. Shan. *2D Actuator Disk and Vertical Axis Rotor Model in the Wave- Current Unsteady Flow*. 2013.

[52] J. Katz. “Convergence and Accuracy of Potential-Flow Methods”. In: *Journal of Aircraft* 56.6 (2019), pp. 2371–2375.

[53] D. Ciliberti et al. “Aircraft directional stability and vertical tail design: A review of semi-empirical methods”. In: *Progress in Aerospace Sciences* 95 (2017), pp. 140–172.

[54] C. Bak. “Aerodynamic design of wind turbine rotors”. In: *Wind Energy Systems*. Elsevier, 2011, pp. 161–207.

[55] A. F. Molland and S. R. Turnock. “6 - Theoretical and numerical methods”. In: *Marine Rudders and Control Surfaces*. Oxford: Butterworth-Heinemann, 2007, pp. 233–311. DOI: https://doi.org/10.1016/B978-075066944-3/50009-3.

[56] Z. Zhao et al. “Variable pitch approach for performance improving of straight-bladed VAWT at rated tip speed ratio”. In: *Applied Sciences* 8.6 (2018), p. 957.

[57] P. Gao et al. “Potential assessment of tidal stream energy around Hulu Island, China”. In: *Procedia Engineering* 116 (2015), pp. 871–879.

[58] B. Jiang et al. “Assessment of wave energy resource of the Bohai Sea, Yellow Sea and East China Sea based on 10-year numerical hindcast data”. In: *OCEANS 2016-Shanghai*. IEEE. 2016, pp. 1–9.

[59] Y. Wan et al. “Wave energy resource assessment off the coast of China around the Zhoushan Islands”. In: *Energies* 10.9 (2017), p. 1320.

[60] H. Lei et al. “Investigation of wake characteristics for the offshore floating vertical axis wind turbines in pitch and surge motions of platforms”. In: *Energy* 166 (2019), pp. 471–489.

A

The U2DiVA code

A.1. Regular waves theory

Regular waves are a simplification of sea waves, and are represented as a simple sinusoidal signal with a given amplitude and period. The x-component of the wave velocity of a water particle can be written in complex notation as:

$$U_{wave} = A_{wave} \cdot e^{-i(\omega_{wave} t - k \cdot x)} \tag{A.1}$$

where A_{wave} is the wave amplitude, ω_{wave} is the circular wave frequency in $[rad/s]$, t is the time in $[s]$, k is the wave number in $[rad/m]$ and x is the position of the water particle. Assuming the water surface slope to be very small so that harmonic displacements, velocities and accelerations are linearly related to the wave surface elevation [46], the wave amplitude is:

$$A_{wave} = \frac{H}{2} \omega_{wave} \frac{cosh(k \cdot (h+z))}{sinh(kh)} e^{i \cdot \phi_{wave}} \tag{A.2}$$

where H is the wave height in $[m]$, h is the water depth in $[m]$ and z is the vertical distance of the water particle in $[m]$ (positive upwards).

By knowing the wave period T_{wave} and assuming deep waters, we can find the previous parameters from the following equations, with the second equation being the dispersion equation in deep water.

$$\omega_{wave} = \frac{2\pi}{T_{wave}} \tag{A.3}$$

$$K = \frac{\omega_{wave}^2}{g} \tag{A.4}$$

A.2. Additional secondary outputs

The lift and drag are the forces perpendicular and aligned with the relative velocity vector. The lift force F_L and drag force F_D per unit span are therefore computed from the horizontal and vertical forces and from the inflow angle ψ, given as $\psi = \alpha + \theta_p = \alpha$ assuming a pitch angle θ_p of 0°:

$$F_L = F_y cos\psi - F_x sin\psi$$
$$F_D = F_x cos\psi + F_y sin\psi$$

From these forces, the lift and drag coefficients of the blade section are:

$$C_{F_L} = \frac{F_L}{0.5 \rho U_{rel}^2 D}$$
$$C_{F_D} = \frac{F_D}{0.5 \rho U_{rel}^2 D}$$

where U_{rel} is the relative velocity at the blade section in [m/s].

The normal force coefficient C_{Fn} and tangential force coefficient C_{Ft} are defined as:

$$C_{Fn} = C_{F_L} cos\phi + C_{F_D} sin\phi$$
$$C_{Ft} = C_{F_L} sin\phi - C_{F_D} cos\phi$$

The non-dimensional normal force F_n and tangential force F_t can be derived as:

$$F_n = C_{Fn} \left(\frac{U_{rel}}{U_\infty} \right)^2$$
$$F_t = C_{Ft} \left(\frac{U_{rel}}{U_\infty} \right)^2$$

A.3. Sensitivity of the U2DiVA code

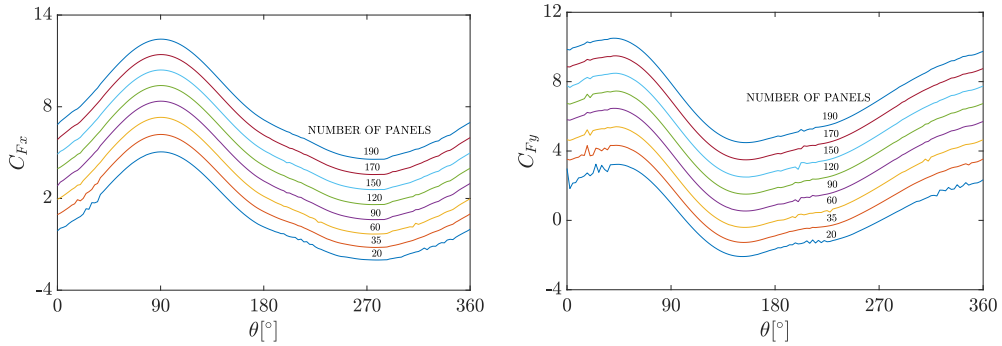

(a) Thrust force coefficient (b) Lateral force coefficient

Figure A.1: Curves of the normalized force coefficients of the Haineng 1 (U_∞=3.5m/s,λ=3.0) over one rotation with increasing N_{panels}. The curves are shifted upwards for increasing N_{panels} for clearer visualization.

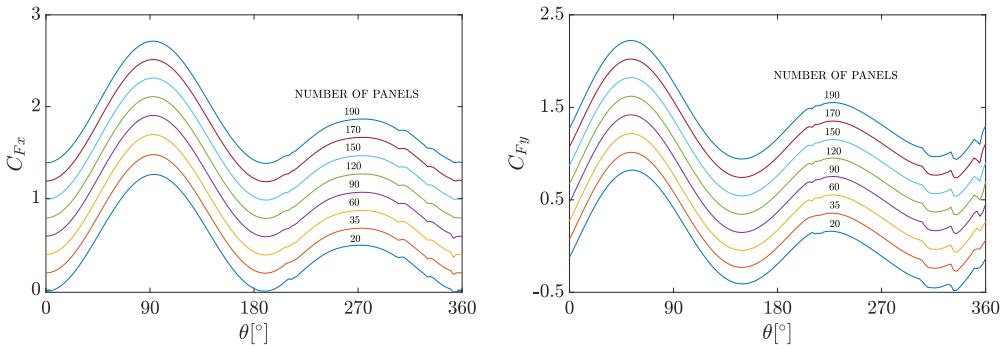

(a) Thrust force coefficient (b) Lateral force coefficient

Figure A.2: Curves of the normalized force coefficients of the Kobold (U_∞=2.0m/s,λ=2.8) over one rotation with increasing N_{panels}. The curves are shifted upwards for increasing N_{panels} for clearer visualization.

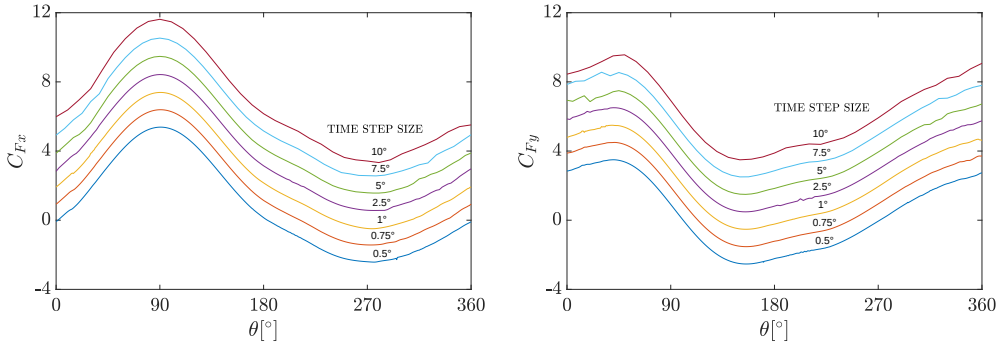

(a) Thrust force coefficient (b) Lateral force coefficient

Figure A.3: Curves of the normalized force coefficients of the Haineng 1 (U_∞=3.5m/s,λ=3.0) over one rotation with decreasing time step size. The curves are shifted upwards for increasing $\Delta\theta$ for clearer visualization.

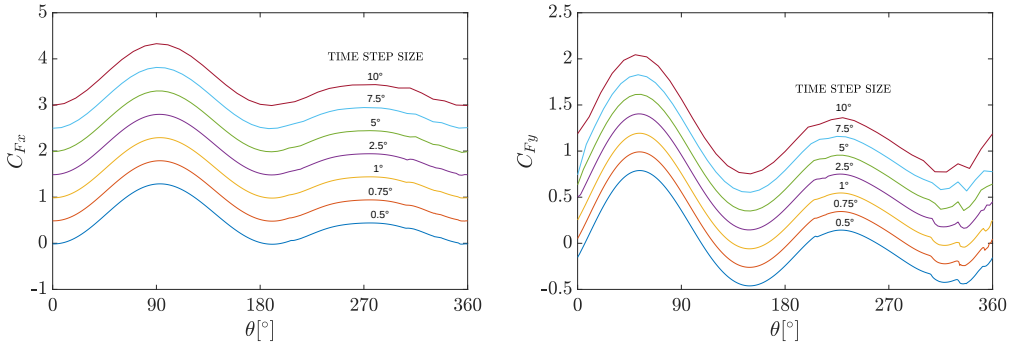

(a) Thrust force coefficient (b) Lateral force coefficient

Figure A.4: Curves of the normalized force coefficients of the Kobold (U_∞=2.0m/s,λ=2.8) over one rotation with decreasing time step size. The curves are shifted upwards for increasing $\Delta\theta$ for clearer visualization.

B

Set-up and additional results of the Haineng 1 and the Kobold turbines

B.1. Set-up of the Haineng 1's and Kobold simulations

Table B.1: Time inputs for the construction of the $C_{power} - \lambda$ curve of the Haineng 1 at different tip speed ratios via U2DiVA code.

λ	0.2-1	1-2	2-3	3
$\Delta\theta$	15°	5°	3°	3°
Number of rotations	20	20	20	50

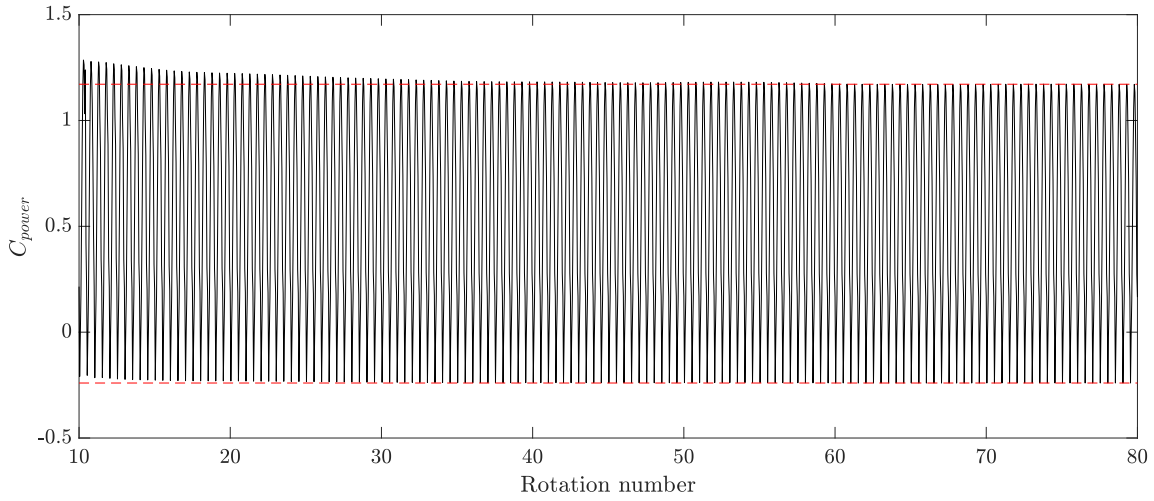

Figure B.1: Time history of the power coefficient of the Haineng 1 turbine (U_∞ = 2m/s,λ = 1.5). The steadiness of envelopes can be observed from the 60^{th} rotation.

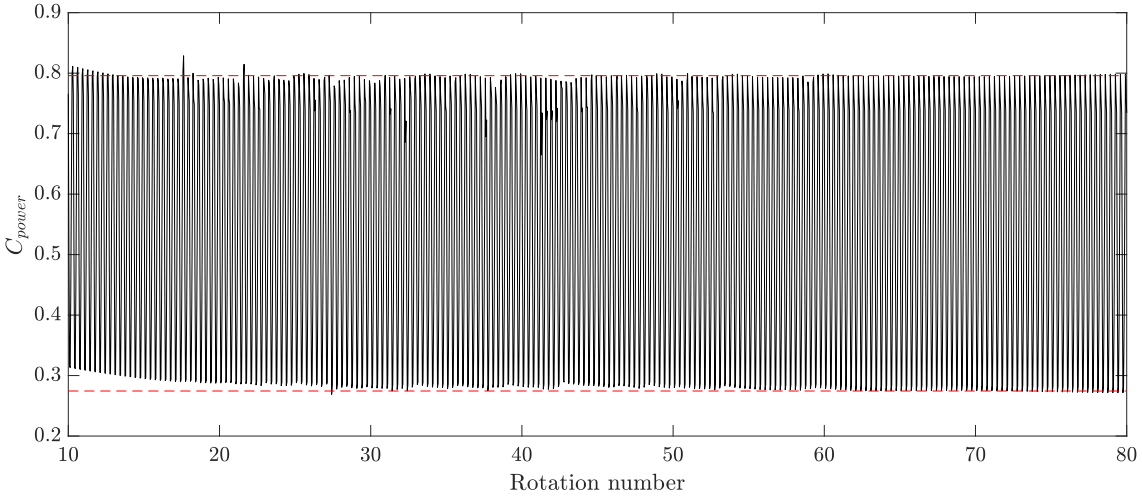

Figure B.2: Time history of the power coefficient of the Kobold turbine ($U_\infty = 2$m/s,$\lambda = 2.5$). The steadiness of envelopes can be observed from the 60^{th} rotation.

B.2. Additional results of the Haineng 1 turbine and Kobold turbine case studies

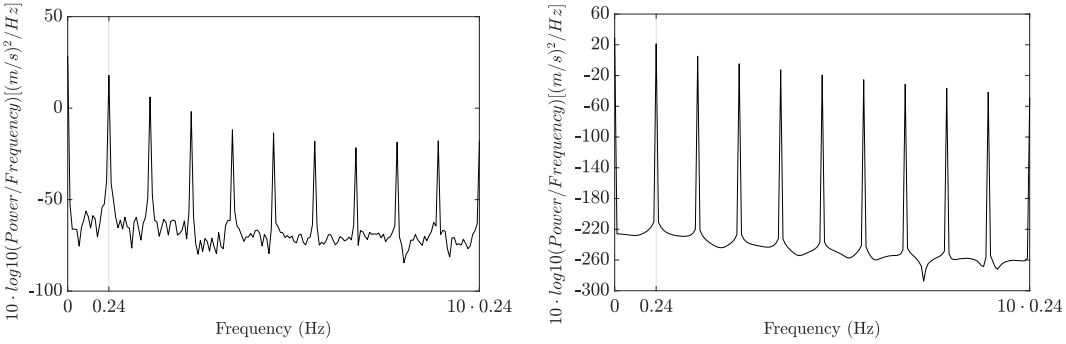

(a) PSD of U_{rel} (b) PSD of $U_{rel} - U_{induced}$

Figure B.3: Comparison of the spectral power density of the relative velocity (a) and of the relative velocity without induction (b) at quarter chord of one blade of the Haineng 1 turbine for the only current reference case ($U_\infty = 2$m/s,$\lambda = 1.5$).

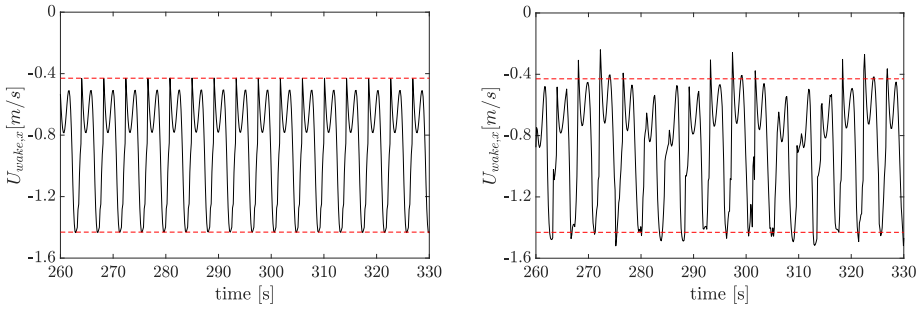

(a) Only current (b) Intense surge

Figure B.4: Comparison of the horizontal wake induced velocity at quarter chord of one airfoil of the Haineng 1 turbine for: (a) the only current case ($U_\infty = 2$m/s,$\lambda = 1.5$) and (b) the intense surge case ($U_\infty = 2$m/s,$\lambda = 1.5, A_{surge} = 1$m/s,$\omega_0 = \frac{2\pi}{5}$rad/s).

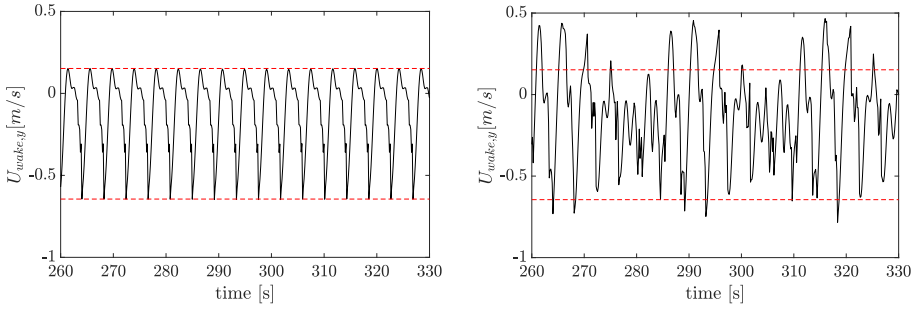

(a) Only current (b) Intense surge

Figure B.5: Comparison of the vertical wake induced velocity at quarter chord of one airfoil of the Haineng 1 turbine for: (a) the only current case (U_∞ = 2m/s,λ = 1.5) and (b) the intense surge case (U_∞ = 2m/s,λ = 1.5,A_{surge} = 1m/s,$\omega_0 = \frac{2\pi}{5}$ rad/s).

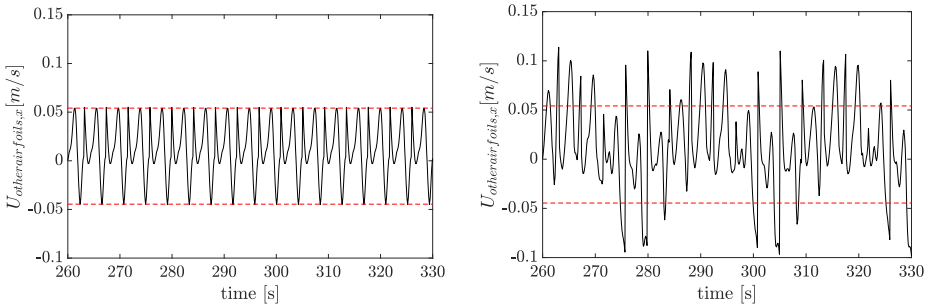

(a) Only current (b) Intense surge

Figure B.6: Comparison of the horizontal velocity induced by the airfoils' doublets/sources distribution at quarter chord of one airfoil of the Haineng 1 turbine for: (a) the only current case (U_∞ = 2m/s,λ = 1.5) and (b) the intense surge case (U_∞ = 2m/s,λ = 1.5,A_{surge} = 1m/s,$\omega_0 = \frac{2\pi}{5}$ rad/s).

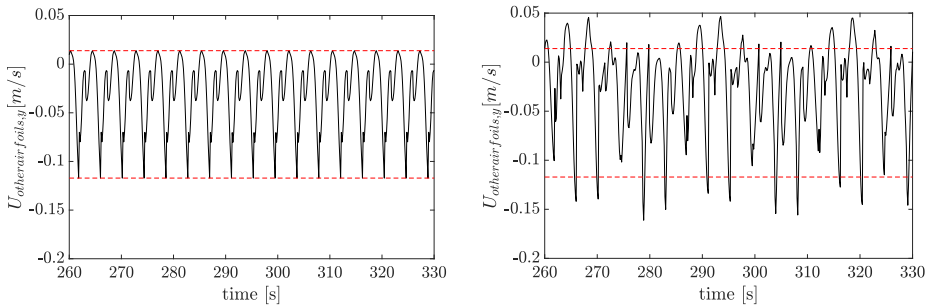

(a) Only current (b) Intense surge

Figure B.7: Comparison of the vertical velocity induced by the airfoils' doublets/sources distribution at quarter chord of one airfoil of the Haineng 1 turbine for: (a) the only current case (U_∞ = 2m/s,λ = 1.5) and (b) the intense surge case (U_∞ = 2m/s,λ = 1.5,A_{surge} = 1m/s,$\omega_0 = \frac{2\pi}{5}$ rad/s).

Table B.2: Operating conditions, inflow conditions and simulation time inputs of the intense surge cases simulated for the phase tuning example of the Haineng 1 turbine.

CASE	Operating conditions		Inflow conditions				Simulation time inputs	
	λ	Φ_0[°]	U_∞[m/s]	A_{surge}[m/s]	ω_0[rad/s]	Φ_{surge}[°]	$\Delta\theta$[°]	Rotations
1	$\frac{2\pi}{4}$	**0**	2	1	$\frac{2\pi}{5}$	**0**	3	60-80
2	$\frac{2\pi}{4}$	**0**	2	1	$\frac{2\pi}{5}$	**30**	3	60-80
3	$\frac{2\pi}{4}$	**0**	2	1	$\frac{2\pi}{5}$	**45**	3	60-80
4	$\frac{2\pi}{4}$	**0**	2	1	$\frac{2\pi}{5}$	**60**	3	60-80

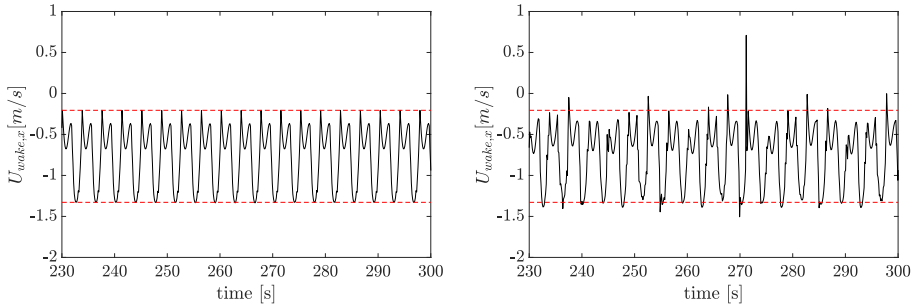

(a) Only current (b) Intense surge

Figure B.8: Comparison of the horizontal wake induced velocity at quarter chord of one airfoil of the Kobold turbine for: (a) the only current case ($U_\infty = 2$m/s,$\lambda = 2.5$) and (b) the intense surge case ($U_\infty = 2$m/s,$\lambda = 2.5$,$A_{surge} = 1$m/s,$\omega_0 = \frac{2\pi}{5}$rad/s).

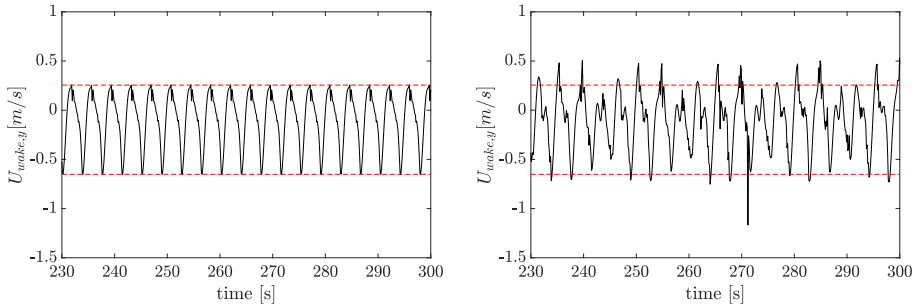

(a) Only current (b) Intense surge

Figure B.9: Comparison of the vertical wake induced velocity at quarter chord of one airfoil of the Kobold turbine for: (a) the only current case ($U_\infty = 2$m/s,$\lambda = 2.5$) and (b) the intense surge case ($U_\infty = 2$m/s,$\lambda = 2.5$,$A_{surge} = 1$m/s,$\omega_0 = \frac{2\pi}{5}$rad/s).

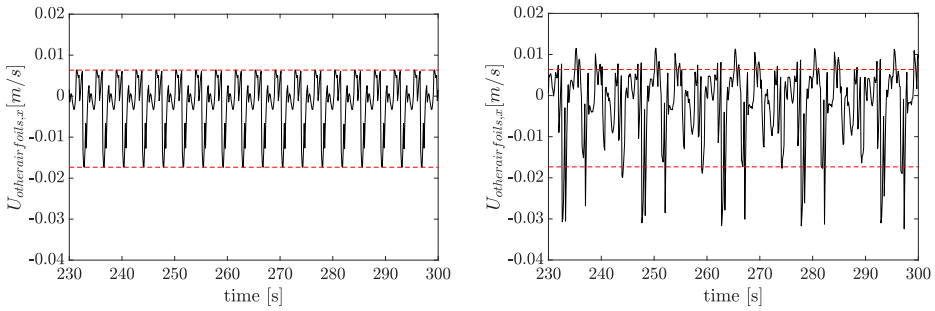

(a) Only current (b) Intense surge

Figure B.10: Comparison of the horizontal velocity induced by the airfoils' doublets/sources distribution at quarter chord of one airfoil of the Kobold turbine for: (a) the only current case ($U_\infty = 2$m/s,$\lambda = 2.5$) and (b) the intense surge case ($U_\infty = 2$m/s,$\lambda = 2.5$,$A_{surge} = 1$m/s,$\omega_0 = \frac{2\pi}{5}$rad/s).

Table B.3: Operating conditions, inflow conditions and simulation time inputs of the only current case (1) and the intense surge case (2) simulated for the rotational speed tuning example of the Haineng 1 turbine.

CASE	Operating conditions		Inflow conditions				Simulation time inputs	
	λ	Φ_0[°]	U_∞[m/s]	A_{surge}[m/s]	ω_0[rad/s]	Φ_{surge}[°]	$\Delta\theta$[°]	Rotations
1	$\frac{2\pi}{10}$	0	2	0	0	0	3	60-80
2	$\frac{2\pi}{10}$	0	2	1	$\frac{2\pi}{5}$	0	3	60-80

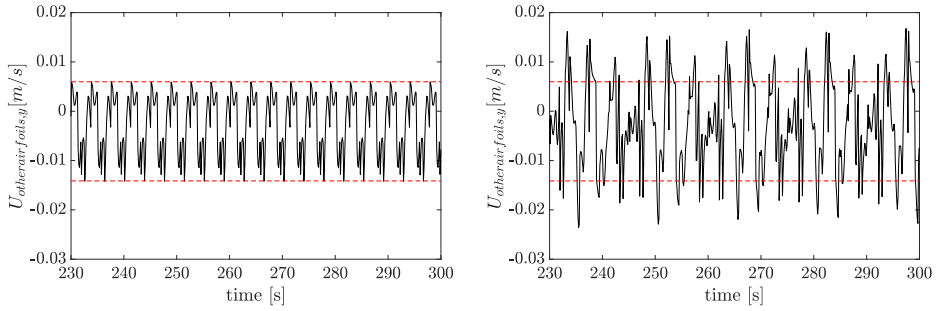

(a) Only current (b) Intense surge

Figure B.11: Comparison of the vertical velocity induced by the airfoils' doublets/sources distribution at quarter chord of one airfoil of the Kobold turbine for: (a) the only current case (U_∞ = 2m/s,λ = 2.5) and (b) the intense surge case (U_∞ = 2m/s,λ = 2.5,A_{surge} = 1m/s,$\omega_0 = \frac{2\pi}{5}$rad/s).

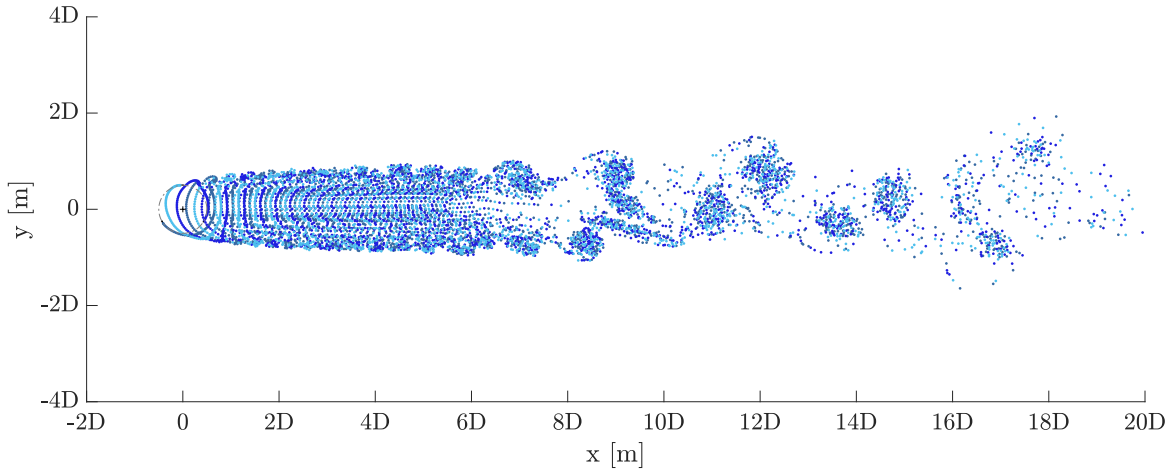

(a) Only current

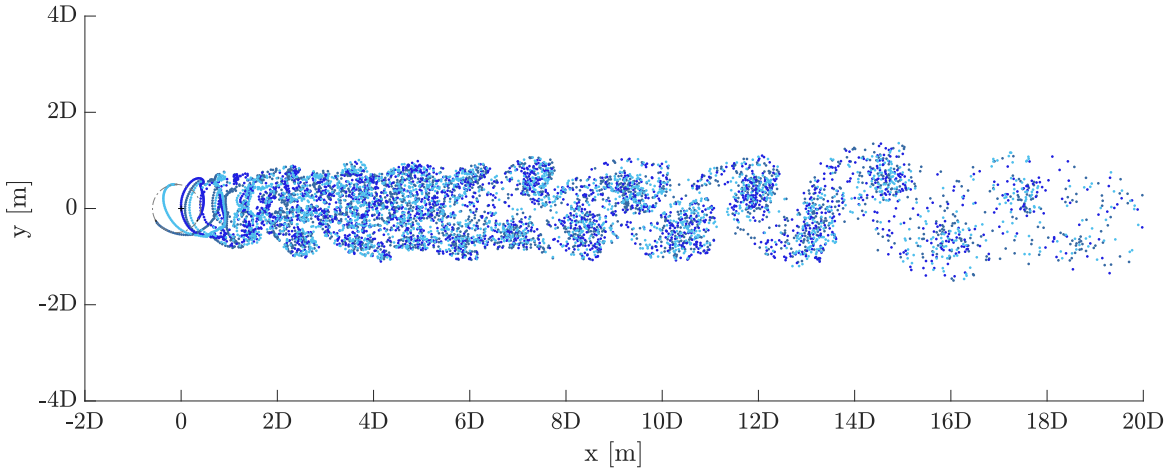

(b) Intense surge

Figure B.12: Evolution of the far-wake up to 20 rotor diameters downwind the Kobold rotor in the only current reference case (a) and in the intense surge case study (b) at simulation time of 238.1s (63^{rd} rotation). The wake elements shed by different airfoils are coloured differently for clearer visualization.

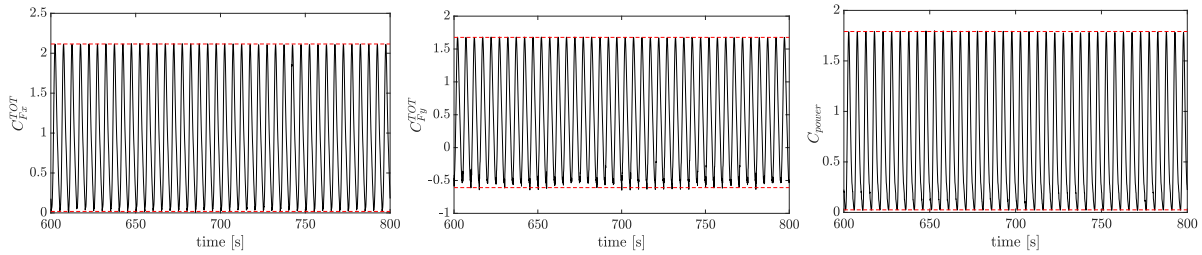

Figure B.13: Time history curves of the rotor thrust, lateral force and power coefficients of the Haineng 1 turbine at $\lambda = \frac{2\pi}{10}$. The envelopes of the hydrodynamic coefficients (red dotted lines) are straight.

Table B.4: Operating conditions, inflow conditions and simulation time inputs of the intense surge cases simulated for the phase tuning example of the Kobold turbine.

CASE	Operating conditions		Inflow conditions				Simulation time inputs	
	λ	Φ_0[°]	U_∞[m/s]	A_{surge}[m/s]	ω_0[rad/s]	Φ_{surge}[°]	$\Delta\theta$[°]	Rotations
1	2.51	**0**	2	1	$\frac{2\pi}{5}$	**-180**	3	60-80
2	2.51	**30**	2	1	$\frac{2\pi}{5}$	**-180**	3	60-80
3	2.51	**45**	2	1	$\frac{2\pi}{5}$	**-180**	3	60-80
4	2.51	**60**	2	1	$\frac{2\pi}{5}$	**-180**	3	60-80
5	2.51	**90**	2	1	$\frac{2\pi}{5}$	**-180**	3	60-80

Table B.5: Operating conditions, inflow conditions and simulation time inputs of the only current case (1) and the intense surge case (2) simulated for the rotational speed tuning example of the Kobold turbine.

CASE	Operating conditions		Inflow conditions				Simulation time inputs	
	λ	Φ_0[°]	U_∞[m/s]	A_{surge}[m/s]	ω_0[rad/s]	Φ_{surge}[°]	$\Delta\theta$[°]	Rotations
1	$\frac{2\pi}{15}\frac{3}{2}$	0	2	0	0	0	3	60-80
2	$\frac{2\pi}{15}\frac{3}{2}$	0	2	1	$\frac{2\pi}{5}$	0	3	60-80

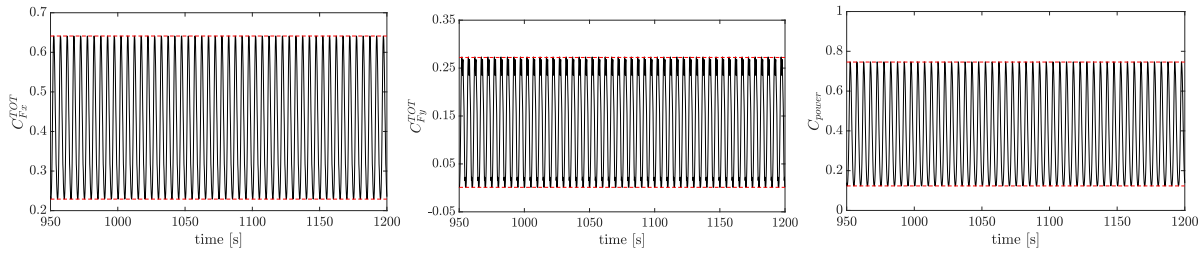

Figure B.14: Time history curves of the rotor thrust, lateral force and power coefficients of the Kobold turbine at $\lambda = \frac{2\pi}{15}\frac{R}{U_\infty}$. The envelopes of the hydrodynamic coefficients (red dotted lines) are straight.